Mechatronic Design and Evaluation of a Two-Degree-of-Freedom Powered Ankle-Foot Prosthesis with Myoneural Interfacing Capabilities

by

Tsung-Han Hsieh

B.Sc., National Taiwan University (2013)
M.Sc., Carnegie Mellon University (2015)
M.Sc., Massachusetts Institute of Technology (2019)

Submitted to the Program in Media Arts and Sciences,
School of Architecture and Planning
in partial fulfillment of the requirements for the degree of
Doctor of Philosophy in Media Arts and Sciences
at the
MASSACHUSETTS INSTITUTE OF TECHNOLOGY
September 2024

Author . . . .
Program in Media Arts and Sciences,
August 15, 2024

Certified by . . . .
Hugh Herr
Professor of Media Arts and Sciences
Thesis Supervisor

Accepted by . . . .
Joseph Paradiso
Academic Head, Program in Media Arts and Sciences

Mechatronic Design and Evaluation of a Two-Degree-of-Freedom Powered Ankle-Foot Prosthesis with Myoneural Interfacing Capabilities

by

Tsung-Han Hsieh

Submitted to the Program in Media Arts and Sciences,,
School of Architecture and Planning
on August 15, 2024, in partial fulfillment of the
requirements for the degree of
Doctor of Philosophy in Media Arts and Sciences

Abstract

Recent advancements in neural interfaces and sensing technologies have opened new possibilities for enhanced prosthesis control. The agonist-antagonist myoneural interface (AMI) connects residual muscle pairs to emulate natural dynamics, while electronic osseointegrated prostheses for the rehabilitation of amputees (eOPRA) allow direct measurement of neural signals through implants. Additionally, magnetomicrometry enables precise, real-time measurement of muscle length. These innovations motivate the development of more sophisticated prosthetic designs, including two degrees of freedom (2DoF) ankle systems.

This Ph.D. thesis advanced bionic limb technology through three primary aims. First, a comprehensive characterization study of human-scale actuators was conducted, including brushless motors of different sizes. Using a custom-built dynamometer, the performance of these actuators was evaluated across their full operating range. Building upon this foundation, an innovative bionic ankle-foot prosthesis with enhanced capabilities was designed and fabricated. This advanced prosthetic system achieved biological fidelity in terms of range of motion, torque output, and angular velocity, thus enabling more natural and adaptable gait patterns. To validate the efficacy of the system, a subject with AMI constructs was fitted with the prosthesis and underwent a series of locomotion tasks, including level-ground ambulation and obstacle traversal.

This work pushed the boundaries of bionic limb function and advanced the restoration of natural locomotion after lower limb amputation, providing valuable insights into the potential of combining advanced prosthetic design with neural interfacing techniques.

Thesis Supervisor: Hugh Herr
Title: Professor of Media Arts and Sciences

Mechatronic Design and Evaluation of a Two-Degree-of-Freedom Powered Ankle-Foot Prosthesis with Myoneural Interfacing Capabilities

by

Tsung-Han Hsieh

The following people served as readers for this thesis:

Thesis Reader . . . .

Edward Boyden
Y. Eva Tan Professor in Neurotechnology
Professor of Brain and Cognitive Sciences, Media Arts and Sciences,
and Biological Engineering
Massachusetts Institute of Technology

Thesis Reader . . . .

Hartmut Geyer
Associate Professor of Robotics
Carnegie Mellon University

Acknowledgments

I would like to express my sincere gratitude to my advisor, Professor Hugh Herr, for his invaluable resources and unwavering support throughout my journey. I am also deeply thankful to my committee members, Professors Ed Boyden and Hartmut Geyer, for their guidance and encouragement in my academic pursuits.

A special thanks goes to Matt Carney for his expert tutelage in mechanical design, and to my lab mates Hyungeun Song, Seong Ho Yeon, Chris Shallal, Junqing Qiao, Daniel Levine, and Tony Shu for their collaboration and camaraderie during this period. I extend my appreciation to our lab administrator, Lindsey Reynolds, for ensuring smooth operations, and to Rick Casler for honing my strategic thinking skills akin to those of a CTO. My heartfelt thanks go to my family and A-O.K. Industrial Corp. for their constant support. I am also indebted to Trend Micro and Foxconn for their generous scholarships. Finally, I would like to acknowledge our sponsors: K. Lisa Yang, DARPA, NIH, and the MIT Media Lab, whose financial support made this research possible.

MIT 一念七年，真的是非常愉快，也有太多人要感謝。我想在這裡好好感謝我最親愛、最支持我的家人，因為有你們，我的研究生涯才能這麼愉快。也特別感謝我的太太，在博士最後的期間辛苦照顧小孩，讓我可以好好把最後這一段學術之路走完。博士學位從來不是我個人的成就，是因為有你們，我才能無後顧之憂地前進。

Contents

List of Figures

List of Tables

Chapter 1

Introduction

1.1 Motivation

Over the past decade, significant progress has been made in bionic prostheses development. These advanced robotic devices, controlled by microcontrollers, aim to restore biological functions beyond the capabilities of conventional prostheses. Despite their increased weight, powered ankle-foot prostheses have been proven to improve the walking economy of individuals with transtibial amputation [1, 2, 3].

Currently available commercial powered ankle-foot prostheses, such as Ottobock Empower [4] and Össur Proprio [5] (see Figure 1-1), are limited to single degree-of-freedom (1-DoF) motions in the sagittal plane (i.e., plantarflexion and dorsiflexion). However, research indicates that ankle movements in the frontal plane (i.e., eversion and inversion) play a crucial role in maintaining balance during walking. Studies on able-bodied individuals have shown that the ankle actively controls frontal plane motions to adjust the center of pressure and maintain stability while walking [6, 7].

Recent advancements in peripheral neural interfaces have shown promise in preserving proprioception after lower-limb amputation, enabling more robust and repeatable motor control. Two notable examples are the agonist-antagonist myoneural interface (AMI) and electronic osseointegrated prostheses for the rehabilitation of amputees (eOPRA), both groundbreaking amputation paradigms. AMI connects residual agonist-antagonist muscle pairs, emulating natural muscle dynamics and leveraging native muscle-tendon sensory organs to generate proprioceptive afferent signals [8, 9]. eOPRA, on the other hand, involves direct skeletal attachment of the prosthesis through osseointegration, combined with implanted neuromuscular electrodes for enhanced control and sensory feedback [10]. These advanced interfaces allow for improved volitional and reflexive motor control, resulting in faster walking speeds, more natural joint kinematics and kinetics, improved inter-limb symmetry, and better adaptation to various terrains and perturbations in individuals using bionic ankles [11].

(a) (b)

Figure 1-1: Commercially available powered ankle-foot prostheses can only perform 1-DoF motions on the sagittal plane: (a) Ottobock Empower [4] and (b) Össur Proprio [5].

These developments highlight the need for a powered 2-DoF ankle-foot prosthesis that is untethered, comparable in weight to the biological ankle-foot complex, and capable of active control in both sagittal and frontal planes. Importantly, such a device should generate sufficient positive net work to support level-ground walking for an average-sized individual – a capability that currently does not exist. The convergence of these technological advancements and biological insights presents a unique opportunity to develop next-generation prosthetic devices. By combining multi-degree-of-freedom functionality with enhanced neural control offered by AMI and eOPRA, there is potential to significantly improve the quality of life for individuals with lower limb amputation. This motivates the exploration of innovative ankle-foot prosthesis designs that can fully leverage the capabilities of these advanced surgical techniques, pushing the boundaries of bionic limb technology.

Furthermore, integrating AMI or eOPRA with a 2-DoF ankle-foot prosthesis could potentially offer unprecedented levels of control, stability, and natural movement for lower limb amputees. This combination could address current limitations in prosthetic technology, such as the lack of proprioception and limited degrees of freedom, ultimately leading to more functional and intuitive prosthetic solutions.

1.2 Prior Art

Several research groups have attempted to develop powered 2-DoF ankle-foot prostheses, as illustrated in Figure 1-2. Bellman *et al.* proposed a mechanical design for a high-power 2-DoF ankle aimed at replicating the functionality of a biological ankle. However, their design weighed 2.1 kg without electronics or battery, and lacked details on control systems or experimental data [12]. Ficanha *et al.* developed a cable-driven 2-DoF ankle prototype capable of modulating impedance in both sagittal and frontal planes. Their design used Bowden cables to transmit power from proximally located motors, reducing weight at the ankle. Despite these advancements, their system was not self-contained or mobile, relying on external power and control systems. Additionally, it faced limitations in torque output and control bandwidth [13]. Kim *et al.* created a cable-driven 2-DoF prosthesis emulator that could independently control plantarflexion and inversion-eversion torque [14]. They conducted clinical trials to examine frontal plane control on balance [15], providing valuable insights into biomechanics and prosthetic design strategies. However, as a tethered system, its use was confined to laboratory settings, limiting its applicability in real-world environments.

Jang *et al.* developed a self-contained 2-DoF ankle-foot prosthesis with a low-inertia extremity, designed for agile walking on uneven terrain [16]. This prosthesis features a compact design with a total weight of 2.25 kg including the battery, making it one of the lightest 2-DoF powered prostheses. It employs a parallel linkage mechanism for 2-DoF motion and a unique spring mechanism to enhance propulsion without increasing foot mass. The prosthesis has a height of 204 mm, comparable to commercial 1-DoF prostheses, and incorporates capacitive-type force sensors for precise ground force detection. While Jang et al.'s work represents a significant advancement in 2-DoF prosthesis design, several limitations and areas for improvement motivated our research:

1. **Torque Control Bandwidth:** While Jang et al. made significant strides in 2-DoF prosthesis design, their work did not report on the torque control bandwidth of their system, which is a crucial performance metric for prosthetic devices. Our work aimed to address this gap by explicitly optimizing the torque control bandwidth, ensuring more responsive and natural movements.

2. **Comprehensive Performance Evaluation:** Jang et al. provided valuable insights into their prosthesis design. Our research sought to expand on this by offering a more comprehensive assessment, including extensive characterization of actuator performance, energy efficiency, and biomechanical outcomes.

3. **Testing with Individuals with Limb Loss:** Jang et al. conducted important initial testing using adapters with individuals without limb loss. Our study aimed to extend this work by including testing with an individual who had undergone transtibial amputation and AMI surgery, potentially offering additional insights.

4. **Neural Control Integration:** Our work aimed to advance beyond traditional control methods by incorporating direct neural control through AMI, potentially offering more intuitive and responsive prosthesis operation.

5. **Actuator Design and Characterization:** we conducted a comprehensive characterization study of human-scale actuators to inform our motor selection and optimization process.

6. **Range of Motion and Torque Output:** Our design targeted increased range of motion and torque output in both sagittal and frontal planes, aiming to

more closely mimic the capabilities of a biological ankle across a wider range of activities.

More recently, I developed an untethered 2-DoF powered ankle-foot prosthesis that builds upon previous designs [17]. This prosthesis integrates dual two-stage belt drives with a four-bar linkage in a compact design, allowing for active control in both sagittal and frontal planes. The system achieves a torque control bandwidth of 9.74 Hz, which is sufficient for replicating human walking dynamics. It also demonstrated torque tracking performance during walking trials with a 77 kg subject, with an RMSE of 6.45 N·m in the sagittal plane. While this design addresses some of the limitations of previous work, it still has room for improvement in terms of range of motion and maximum torque output compared to the biological ankle.

1.3 Research Objective

The primary goal of this Ph.D. thesis is to design, develop, and evaluate an advanced bionic ankle-foot prosthesis capable of mimicking natural ankle function, potentially pushing the boundaries of restored locomotion after lower limb amputation. This research is motivated by the limitations of current prosthetic technologies, which often fail to replicate the complex biomechanics of the human ankle-foot complex. Despite recent advancements in powered prostheses, there remains a significant gap between the capabilities of artificial limbs and their biological counterparts.

The human ankle-foot complex plays a crucial role in locomotion, providing stability, energy storage and return, and adaptability to various terrains. It exhibits a remarkable range of motion and force output, allowing for smooth transitions between different gait phases and activities. Current prosthetic devices often struggle to match this versatility, leading to suboptimal gait patterns, increased metabolic cost, and reduced mobility for people with lower limb amputation.

This research aims to address these challenges by leveraging cutting-edge actuator technology, innovative mechanical design, and advanced control strategies. We seek to create a prosthesis that can closely replicate the functionality of a natural ankle across

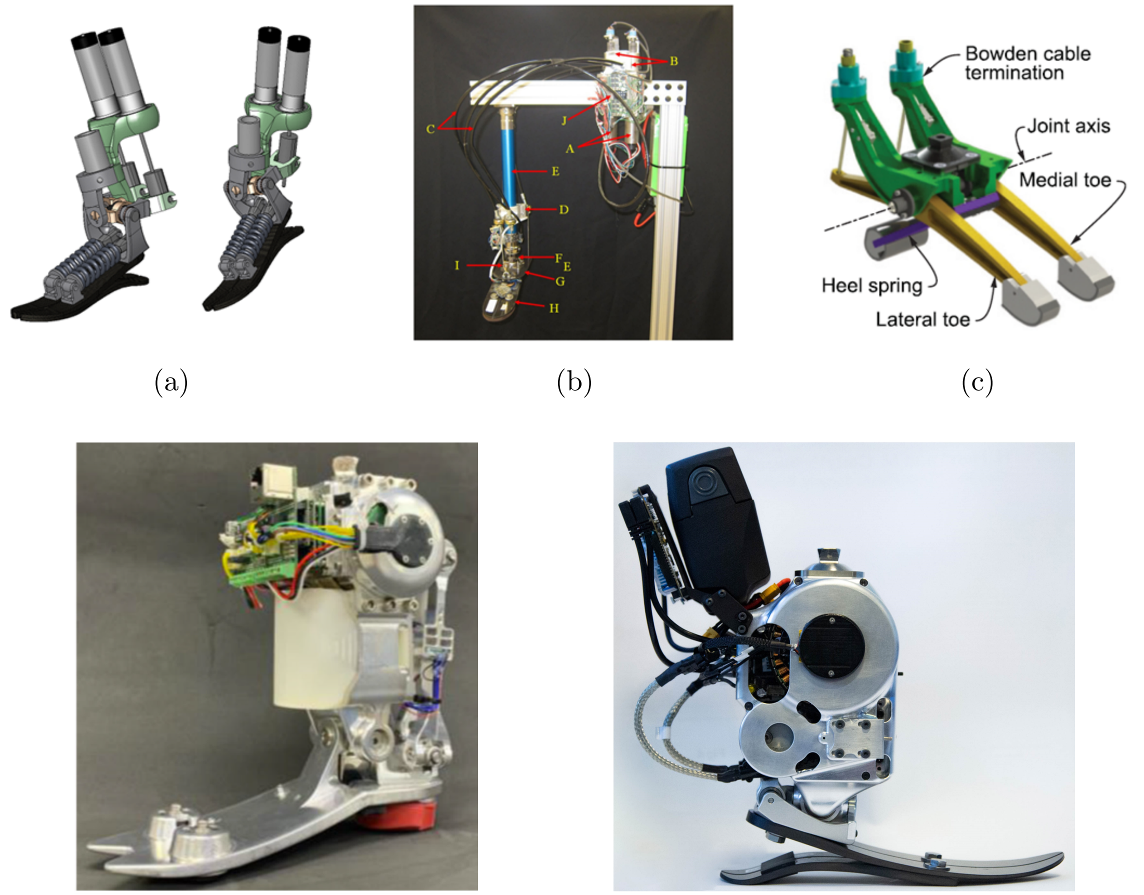

(a) (b) (c)

(d) (e)

Figure 1-2: State-of-the-art powered 2-DoF prostheses: (a) System proposed by Bellman *et al.* featuring a mechanical design of a high-power 2-DoF ankle [12]; (b) Ficanha *et al.*'s 2-DoF ankle prototype that is cable-driven, with electronics separated from the system [13]; (c) Kim *et al.*'s 2-DoF prosthesis emulator used for biomechanics studies [14]; (d) Jang *et al.*'s self-contained 2-DoF ankle-foot prosthesis with low-inertia extremity [16]; and (e) Hsieh *et al.*'s untethered 2-DoF powered ankle-foot prosthesis with dual two-stage belt drives and four-bar linkage [17].

a wide range of activities and environments. By integrating recent advancements in neural interfaces, particularly AMI, we aim to provide more intuitive and responsive control to the user.

Specific objectives include:

- Conducting a comprehensive characterization study of human-scale actuators, including brushless motors of different sizes, using a custom-built dynamometer to evaluate their performance across the full operating range.

- Designing and developing a novel bionic ankle-foot prosthesis with advanced capabilities, such as biological range of motion, torque, and speed outputs, to enable more natural and versatile gait patterns.

- Testing the system under direct neural control with an AMI subject on adaptation to terrains and perturbations to validate performance.

By achieving these objectives, this research aims to demonstrate the feasibility and potential of our advanced bionic ankle-foot prosthesis design when used in conjunction with AMI. Through our single-subject study, we hope to showcase the prosthesis's capabilities in terms of replicating natural ankle function and adaptability across various terrains and conditions. While we cannot generalize from a single case, we expect to provide valuable insights into the performance of our design and its interaction with AMI, potentially informing future directions in prosthetic development and neural interface integration.

Furthermore, the insights gained from this research could have broader implications beyond prosthetics. The advanced actuator technologies and control strategies developed here could inform the design of other robotic systems, particularly in applications requiring high-performance, human-scale actuation. The integration of neural control with advanced mechanical systems could also contribute to the growing field of human-machine interfaces, potentially influencing future developments in rehabilitation robotics, assistive devices, and even augmentative technologies for enhancing human capabilities across diverse populations.

Ultimately, this Ph.D. thesis seeks to push the boundaries of bionic limb function and restoration of locomotion after lower limb amputation. By bridging the gap between biological performance and artificial limbs, we aim to take a significant step towards the goal of fully restoring natural movement capabilities to people with lower limb amputation.

1.4 Summary of Chapters

Chapter 2 presents a comprehensive study of human-scale actuators. The chapter begins by introducing the experimental setup and methodology used for characterizing different brushless motors. Detailed efficiency maps, loss maps, and thermal response profiles are provided for each motor. The findings from these characterizations inform the selection of actuators for the prosthesis design, balancing performance with practical constraints such as size and weight.

Building on the insights from the actuator characterization, Chapter 3 details the mechanical design of the two-degree-of-freedom powered ankle-foot prosthesis. It covers the design specifications, actuator integration, kinematics modeling, and force sensing strategies. The chapter also discusses the development of custom actuators and the innovative mechanical design that enables the prosthesis to achieve biological fidelity in terms of range of motion and torque output.

Chapter 4 focuses on the validation of the prosthesis system. This chapter describes the experimental setup and procedures used to test the prosthesis with a human subject. The results of these tests are presented, demonstrating the system's capabilities in replicating natural ankle movements and adapting to various terrains. The chapter concludes with a discussion of the performance metrics and the implications of the findings for future prosthesis designs.

The final chapter, Chapter 5, summarizes the key contributions of the thesis and discusses the broader implications of the research. It highlights the advancements made in bionic ankle-foot prosthesis design and outlines potential directions for future work. The chapter emphasizes the need for continued innovation to further enhance the functionality and adaptability of prosthetic devices.

Chapter 2

Characterization of Human-Scale Actuators

2.1 Introduction

The multirotor drone market experienced significant expansion in recent years. This growth was attributed to the increasing adoption of drones across various sectors. Drones gained popularity in photography and videography, offering unique perspectives and capabilities. They also found applications in industrial fields such as agriculture, construction, and surveying [18], where they could perform tasks with greater efficiency and safety compared to conventional methods. This trend drove substantial advancements in motor technology, particularly in the development of exterior-rotor brushless motors.

Exterior-rotor brushless motors provided superior torque density compared to their interior-rotor counterparts [19, 20, 21]. This feature made them especially suitable for robotics applications with space and weight constraints. In the field of legged robotics [22, 23, 24], these motors enabled more compact and efficient designs. Similarly, in prosthetics [25, 26, 27] and exoskeletons [28, 29, 30], these motors delivered the required power without excessive weight or bulk. Consequently, the characteristics of these motors made them an appropriate choice for diverse applications, highlighting their significance in robotics.

However, fully utilizing the potential of these motors presented a notable challenge. Drone motor manufacturers typically did not provide comprehensive performance data for these motors under conditions beyond drone-specific applications. This data scarcity created a knowledge gap, potentially limiting the effective use of these motors in various applications. Some research groups attempted to address this gap by examining the performance of such motors across different applications [31, 32]. While these studies offered insights into the performance characteristics of these motors, they had limitations. For example, they did not include direct electrical power measurements entering the motor, nor did they extensively explore high-power use scenarios.

To address these limitations, our study aimed to provide a more in-depth analysis of the performance characteristics of multiple exterior-rotor brushless motors under various operating conditions. We focused on three motors of different sizes: the U8Lite KV100 (87mm in diameter), T-motor RI 50 KV100 (54mm in diameter), and T-motor R60 KV115 (69mm in diameter). These motors had been utilized in numerous robotic applications [22, 23, 27, 33, 30, 34]. Our evaluation encompassed direct measurements of electrical power input to both the drive and motors, as well as the mechanical power output from the motor shafts during operation. We developed comprehensive efficiency maps for all three motors, providing insights into their performance across their full operating ranges.

The U8Lite KV100 motor was subjected to a more comprehensive analysis, encompassing operation under various voltages and thermal response monitoring [35]. This comprehensive approach allowed us to explore the implications of high-power short-duration operation, which is often required in robotics applications due to the periodic nature of loads encountered during activities such as walking, running, or jumping.

By comparing the efficiency maps of these three motors, we provided insights into the trade-offs between motor size, efficiency, and power output, which is crucial for informing motor selection in various robotic applications. The additional thermal analysis of the U8Lite KV100 offered a deeper understanding of the potential risks and benefits of high-power short-duration operation for this specific motor.

Furthermore, our study aimed to provide a comprehensive understanding of the performance characteristics of these motors under various operating conditions. While manufacturers generally discouraged overpowering motors due to potential issues such as reduced efficiency, performance degradation caused by torque saturation, and permanent damage from overheating and demagnetization, our detailed analysis of the U8Lite KV100 suggested that with careful temperature monitoring and proper thermal management, overpowering could be performed safely for short durations.

The findings from this comprehensive evaluation contributed to the design of actuators in robotics applications, particularly those requiring high power output for brief durations. By addressing the current knowledge gap, we aimed to enhance the understanding and utilization of these exterior-rotor brushless motors in various robotics applications. Ultimately, our study sought to contribute to ongoing efforts to optimize the performance and efficiency of robotic systems, providing valuable insights for the design of future robotic systems. Through this research, we hoped to facilitate the development of more efficient, effective, and versatile robotic systems by enabling more informed motor selection based on specific application requirements.

2.2 System Architecture

Figure 2-1 illustrates the system employed for testing. Figure 2-1a presents the overall schematic representation of the system, while Figure 2-1b depicts its physical embodiment. The switching power supplies, rated at 2500 W, encompass three models operating at 24 V, 36 V, and 48 V (UHP-2500-24, UHP-2500-36, and UHP-2500-48, MEAN WELL Enterprises Co., Ltd., New Taipei City, Taiwan). The selection of these voltage levels was based on several considerations. Firstly, these voltages are commonly used in mobile systems, making them readily available for purchase. While higher voltages could potentially enhance motor efficiency, the associated increase in the weight of the required battery pack often does not justify the relatively minor efficiency gains. Secondly, the prevalence of these voltages in mobile systems simplifies the purchase of compatible electronic components for power management. Essential components, including surge protection integrated circuits, diodes, and capacitors, are readily available within these voltage ranges, thereby ensuring the reliable operation of the system.

The drive system, the EVEREST XCR-C motor driver (Novanta Inc., Bedford, MA, USA), boasts a power rating of 3000 W and supports voltage inputs ranging from 8 to 80 V. It delivers a continuous current of 45 A and can handle a peak current of 60 A for up to 3 seconds. The driver was tuned to operate motors using a 100 kHz PWM switching frequency along with a 50 kHz current control loop, the latter utilizing an internal field-oriented control algorithm.

To enable feedback control, an absolute encoder (RM44, RLS Merilna tehnika d.o.o., Komenda, Slovenia) was installed on the back of the motor. Additionally, an optional temperature sensor (NTC thermistor B57861S0103A039, TDK Electronics AG, Munich, Germany) can be directly affixed to the stator winding coil using a thermally conductive epoxy (EP42HT-2AO-1 Black, Master Bond Inc., Hackensack, NJ, USA) to monitor the motor's thermal response. For enhanced measurement accuracy, the thermistor is connected to a 2.5 kOhm reference resistor (USR2G-2K5X1, Riedon, Alhambra, CA, USA) forming a half-bridge circuit.

To maintain a consistent starting temperature of 25 °C and to facilitate effective cooling, a fan is positioned adjacent to the motor. The operation of the fan is regulated based on the readings from the temperature sensor, ensuring optimal thermal management and performance stability of the motor system.

To monitor the DC voltage and current entering the motor driver, a differential voltage divider (Entube DE, Verivolt, San Francisco, CA, USA) and a zero-flux current sensor (IsoBlock I-ZF, Verivolt, San Francisco, CA, USA) were used. The voltage sensor has a measuring range of ±100 V with an 85 kHz bandwidth and ±0.05% accuracy, while the current sensor has a measuring range of ±100 A with an 100 kHz bandwidth and ±0.02% accuracy. Both the voltage and current sensors produce an output of ±10 V, a value that aligns with the input requirements of a typical data acquisition (DAQ) device. To measure the line currents entering the motor, the same

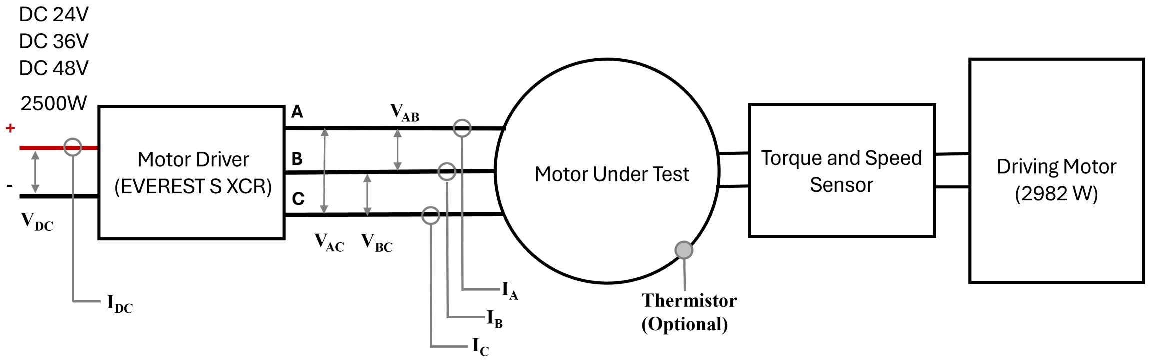

(a) Diagram representing the key components.

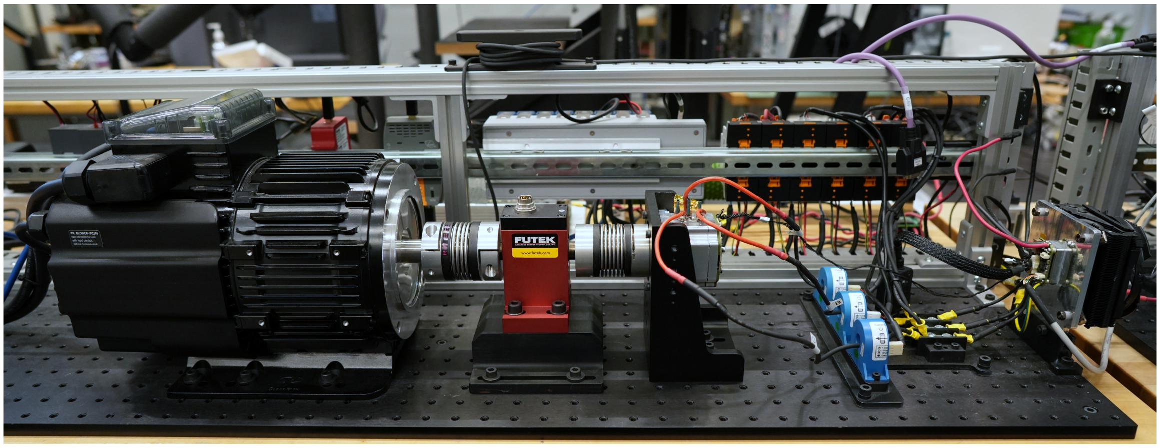

(b) Physical realization of the system.

Figure 2-1: Overview of the experimental apparatus designed for the in-depth characterization of the motor and drive. (**a**) Diagram representing the key components. (**b**) Physical realization of the system.

current sensors were utilized, while the line voltages were measured using a 3-channel differential voltage down-converter specifically designed for 3-phase systems (Entube TE, Verivolt, San Francisco, CA, USA). The Entube TE has the same measuring range, bandwidth, accuracy, and output as Entube DE. The output torque and speed of the motor were measured using a rotary torque sensor with integrated encoder (TRS705 FSH02564, Futek, Irvine, CA, USA). The torque sensor has a sensing range of ±5 Nm and a nonlinearity of ±0.2%. It was calibrated by the manufacturer prior to shipping. The driving motor (CPM-MCVC-D1003A-RLN, Teknics Industries, Inc., Lincoln Park, NJ, US) is an integrated 3-phase servo motor that operates under 208 V AC and has a power rating of 4 hp (2982.8 W). It has a continuous torque of 13.4 Nm, a peak torque of 32.9 Nm, and a maximum speed of 2760 RPM.

Data from the voltage and current sensors were acquired using two analog input modules (NI 9215, Austin, TX, USA) at 40,000 samples/second, while the data from the thermistor were collected via a different analog input module (NI 9219, Austin, TX, USA) at 100 samples/second. This module has built-in voltage and current excitation and supports half-bridge inputs. A digital output module (NI 9401, Austin, TX, USA) was used to control the 3-phase servo motor. All these input and output modules were installed within a chassis (NI cDAQ-9178), which interfaced with a host computer via USB. Data from the torque sensor were collected at 100 samples/second and processed utilizing an separate DAQ system (USB 520, Futek, Irvine, CA, USA), which was also connected to the computer via USB. The configuration used for measuring both the electrical power and temperature is represented in Figure 2-2, which provides a detailed depiction of the setup, offering a close-up view that allows for a comprehensive understanding of the measurement apparatus.

2.3 Efficiency and Loss Mapping Procedure

The experimental procedure involved a systematic exploration of the entire torque-speed plane through the establishment of a mesh of reference operating points, as illustrated in Figure 2-3. The figure represents the operating points utilized during testing under 24 V conditions. The speed range spanned from 0 to 1500 RPM and was divided into equally spaced intervals of 100 RPM. This interval selection ensured an adequate resolution. Similarly, for each speed value, the torque, corresponding to the commanded current A, was adjusted from 0 to 50 A in increments of 5 A. These increments were also chosen to achieve an appropriate resolution. To further enhance the resolution, additional points of 2 A and 4 A were included for each speed value in the tests. Note that in this setup, the driving motor was regulated based on the speed and set the desired speed for a specific operating point. On the other hand, the motor was current controlled. Higher current levels result in greater torque generation based on the relationship between motor torque constant, number of wire turns, magnetic flux strength, and current. Therefore, the operating points in Figure 2-3 with higher

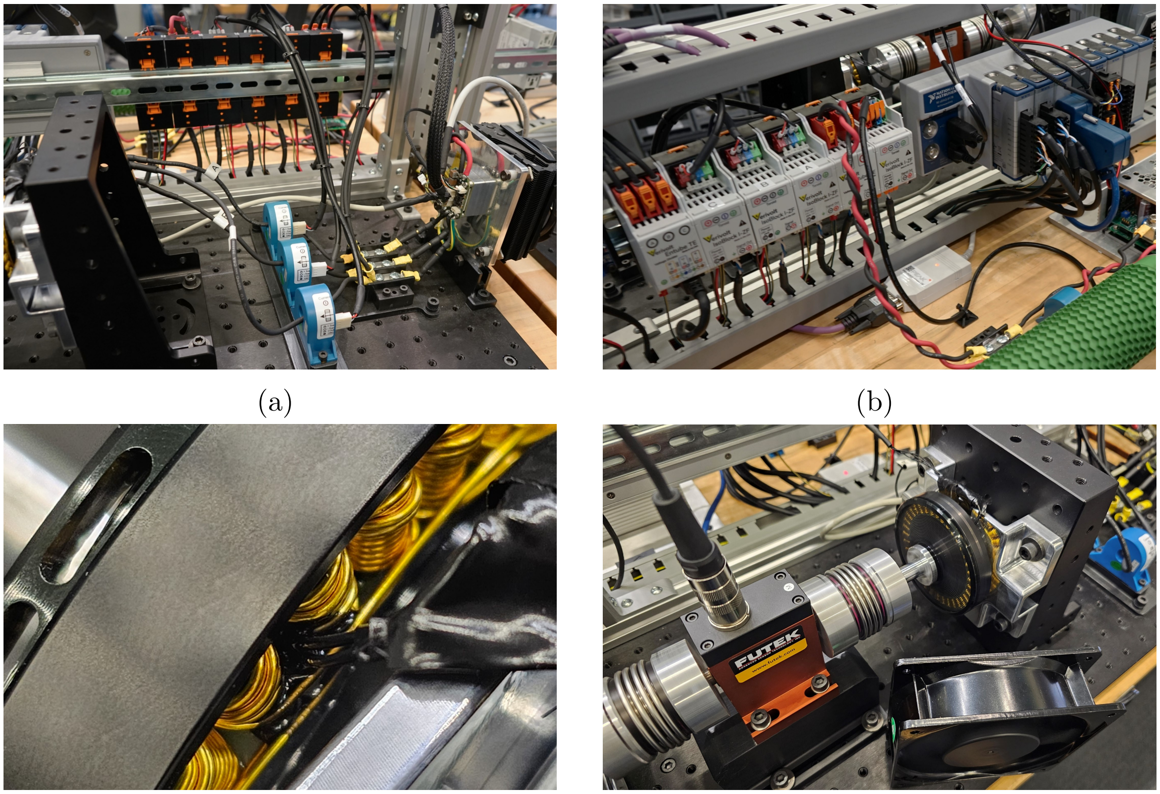

(a)

(b)

(c)

(d)

Figure 2-2: Close-up views of key components: (**a**) current and voltage sensors, (**b**) rear view of the sensors and the DAQ system, (**c**) direct installation of a thermistor on the stator coil, and (**d**) placement of a fan adjacent to the motor for cooling.

current setpoints correspond to a higher torque output.

For each operating point, the driving motor would first start for one second to ensure it reached the target speed, and then the motor under test would begin applying torque. The tests were conducted for a duration of 3.5 s. After the 3.5 s interval, both motors were stopped, but the DAQ continued to collect temperature readings for an additional 15 s. Subsequently, the fan was activated to cool the motor until its temperature dropped below 25 °C before commencing the next operating point. During data processing, the initial and final 20% of the data were trimmed, and the remaining portion was utilized for the calculations. To calculate the motor's input electrical power, the following equation was used:

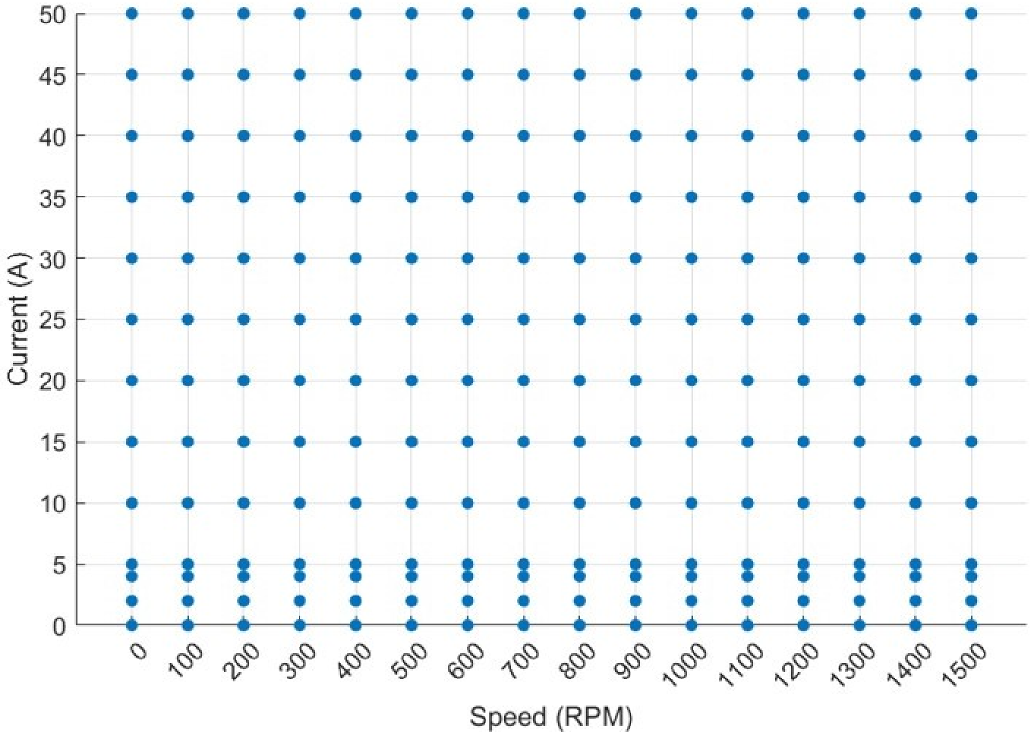

Figure 2-3: Example operating points. The plot showcases the specific combination of speed and torque values spanning the entire torque-speed plane.

$$\begin{aligned} P_E = \frac{1}{\sqrt{3}} \Big[& V_{AB} I_B \cos\left(\theta_{B/AB} - \frac{\pi}{6}\right) \\ & + V_{AC} I_A \cos\left(\theta_{A/AC} - \frac{\pi}{6}\right) \\ & + V_{BC} I_C \cos\left(\theta_{C/BC} - \frac{\pi}{6}\right) \Big], \end{aligned} \tag{2.1}$$

where I_A, I_B, and I_C represent the measured line currents, and V_{AB}, V_{AC}, and V_{BC} represent the measured line voltages. $\theta_{B/AB}$ represents the phase difference between I_B with respect to V_{AB}, $\theta_{A/AC}$ represents the phase difference between I_A with respect to V_{AC}, and $\theta_{C/BC}$ represents the phase difference between I_C with respect to V_{BC}. This equation is used to calculate the electrical power in unbalanced three-phase delta circuits with inductive or capacitive loads [36]. The DC power entering the drive was calculated using the following equation:

$$P_{DC} = V_{DC} I_{DC}, \tag{2.2}$$

where V_{DC} and I_{DC} represent the root mean square (RMS) values of the DC voltage and current, respectively, coming out of the power supply. The RMS values of V_{DC} and I_{DC} were used due to the motor's behavior at certain high-speed operating points. At these points, the motor essentially operates as a generator with negligible torque output, as opposed to its typical function as a torque generator. As a result, the AC currents were measured, necessitating the utilization of RMS values. The output mechanical power from the U8Lite KV100 motor was calculated as:

$$P_M = \tau_M \cdot \omega_M, \tag{2.3}$$

where τ_M is the measured torque, and the ω_M is the measured speed. Using these power values, the motor efficiency η_M can be determined as follows:

$$\eta_M = P_M / P_E. \tag{2.4}$$

Similarly, the motor driver efficiency η_D can be calculated as:

$$\eta_D = P_E / P_{DC}. \tag{2.5}$$

Furthermore, the power loss of the motor P_{loss} can be determined by subtracting the output mechanical power P_M from the input electrical power P_E:

$$P_{loss} = P_E - P_M. \tag{2.6}$$

2.4 Software Development

The dynamometer control and analysis software is a versatile, custom-developed application designed to facilitate comprehensive testing and characterization of various electric motors. The software interface is divided into several key sections, each serving a specific function in the testing process. Figure 2-4 illustrates the software interface.

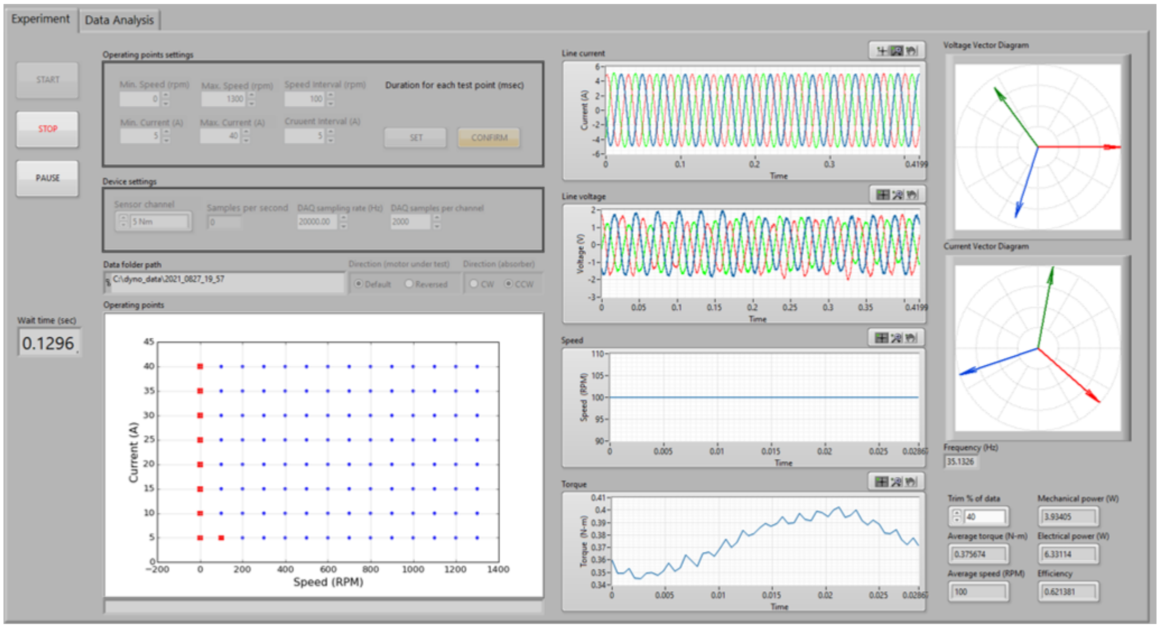

Min. Speed (rpm) 0
Max. Speed (rpm) 1300
Speed Interval (rpm) 100
Duration for each test point (msec)
Min. Current (A) 5
Max. Current (A) 40
Cruuent Interval (A) 5
Sensor channel 5 Nm
Samples per second 0
DAQ sampling rate (Hz) 20000.00
DAQ samples per channel 2000
Data folder path C:\dyno_data\2021_0827_19_57
Direction (motor under test) ● Default ○ Reversed
Direction (absorber) ○ CW ● CCW
Wait time (sec) 0.1296
Frequency (Hz) 35.1326
Trim % of data 40
Mechanical power (W) 3.93405
Average torque (N-m) 0.375674
Electrical power (W) 6.33114
Average speed (RPM) 100
Efficiency 0.621381

Figure 2-4: Dynamometer control interface for motor testing and data acquisition.

The experiment control panel at the top-left of the interface contains buttons for starting, stopping, and pausing the experiment, allowing control over the testing process. Adjacent to this is a section for setting operating points, where users can specify speed and current ranges and intervals, as well as the duration for each test point. This flexibility enables systematic exploration of any motor's performance across its entire operational range.

A device settings section allows configuration of data acquisition parameters, including sensor channel selection, sampling rates, and samples per channel. These adjustable settings ensure the software can accommodate various data acquisition needs for different motors and testing scenarios. A data folder path field is provided to specify where collected data will be saved, facilitating organized data management across multiple motor tests.

Central to the interface is a large plot displaying the operating points being tested, with speed on the x-axis and current on the y-axis. This visual representation helps researchers track the progress and coverage of their motor characterization efforts.

Real-time data visualization is a key feature, with plots for line current, line voltage, speed, and torque displayed on the right side of the interface. These plots offer immediate insight into the motor's performance during testing, regardless of the specific motor type.

Vector diagrams for voltage and current in the top-right corner provide a visual representation of phase relationships in three-phase systems, applicable to a wide range of motor types. Performance metrics such as frequency, mechanical and electrical power, average speed, and efficiency are calculated and displayed in real-time, offering immediate insights into the motor's performance at each operating point.

After data collection is complete, a separate data analysis software can be utilized. The interface of this software is shown in Figure 2-5.

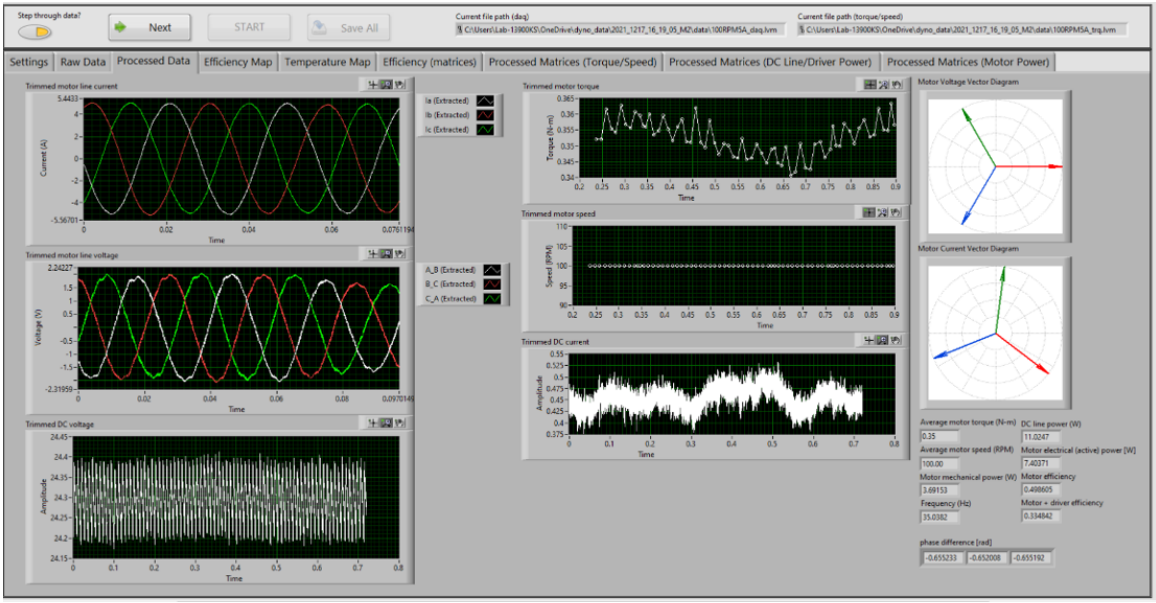

Current file path (daq): C:\Users\Lab-13900KS\OneDrive\dyno_data\2021_1217_16_19_05_M2\data\100RPM5A_daq.lvm

Current file path (torque/speed): C:\Users\Lab-13900KS\OneDrive\dyno_data\2021_1217_16_19_05_M2\data\100RPM5A_trq.lvm

Average motor torque (N-m): 0.35

DC line power (W): 11.0247

Average motor speed (RPM): 100.00

Motor electrical (active) power [W]: 7.40371

Motor mechanical power (W): 3.69153

Motor efficiency: 0.498605

Frequency (Hz): 35.0382

Motor + driver efficiency: 0.334842

phase difference [rad]: -0.655233 -0.652008 -0.655192

Figure 2-5: Interface of the custom data analysis software for processing and visualizing motor performance data.

The data analysis software is a crucial component of the motor characterization system, designed to process and visualize the extensive data collected during dynamometer testing. This software features a multi-tabbed interface for comprehensive data examination.

The main view displays several key plots, including trimmed motor line current, line voltage, DC voltage, motor speed, and DC current. These graphs allow for detailed inspection of the motor's electrical and mechanical behavior during testing. Vector diagrams for motor voltage and current provide insights into the phase relationships within the motor.

Real-time calculations of critical performance metrics are displayed, including average motor torque, speed, power measurements (DC line, motor electrical, and mechanical), efficiency, and frequency. The software also computes phase differences for in-depth analysis of the motor's electrical characteristics.

Navigation through datasets is facilitated by "Step through data" and "Next" buttons, enabling detailed examination of motor performance across different operating conditions or time points. The various tabs - Raw Data, Processed Data, Efficiency Map, Temperature Map, and Processed Matrices - offer different perspectives on the collected data, supporting a thorough analysis of motor performance across its operational range.

The dynamometer control and data analysis software developed for this thesis provide valuable tools for electric motor characterization. These two software components work together to offer a comprehensive solution for motor testing and performance evaluation. Together, these software components form a platform that enhances the efficiency and depth of motor performance studies. They streamline the testing process and enable researchers to extract meaningful insights from complex datasets. This integrated approach to motor characterization supports detailed research in electric motor performance, contributing useful tools to the field of electromechanical systems engineering.

2.5 Motor Efficiency Maps

Figure 2-6 presents the efficiency maps for the two motors under study: the T-motor RI 50 KV100 (54mm diameter) and T-motor R60 KV115 (69mm diameter). These maps are instrumental in evaluating motor efficiency across the entire torque-speed spectrum, offering valuable insights into performance characteristics for each motor size and design.

The efficiency maps visually represent the ratio of output mechanical power to input electrical power across various operating points for each motor. Regions of higher efficiency indicate areas where less electrical power is converted to heat, thus maximizing energy utilization. For instance, in mobile applications using these motors, operating within the high-efficiency region is paramount to optimize battery utilization.

Moreover, these maps provide crucial information on each motor's capabilities beyond its rated power, illustrating the maximum torque and speed limits achievable. This is particularly relevant when comparing the performance of the smaller T-motor RI 50 to the larger R60. By analyzing these efficiency maps, we can:

- Identify optimal operating ranges for specific applications of each motor
- Understand power dissipation patterns across different load conditions for varying motor sizes
- Determine potential for short-term operation beyond rated specifications for each motor type
- Compare performance characteristics across the different motor designs and sizes

This comprehensive visualization of motor performance serves as a powerful tool for selecting between the U8Lite, T-motor RI 50, and T-motor R60 for various robotic and mobile applications, allowing for informed decisions based on size constraints and efficiency requirements.

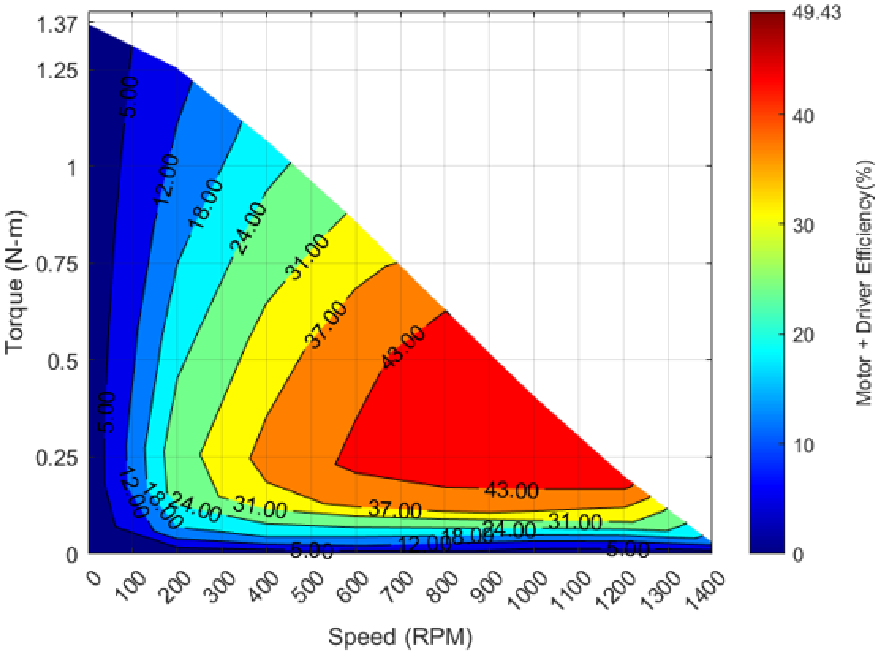

(a) Efficiency map of T-motor RI 50 KV100 at 48V

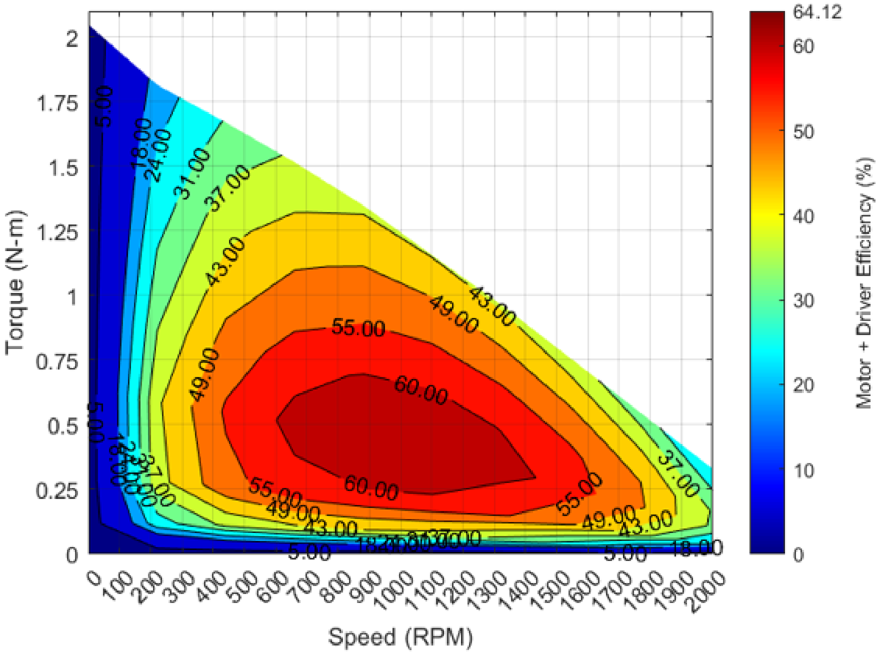

(b) Efficiency map of T-motor R60 KV115 at 48V

Figure 2-6: Efficiency maps of the two studied motors showing the relationship between torque, speed, and efficiency. Color gradients represent efficiency levels, with warmer colors (reds and oranges) indicating higher efficiency, and cooler colors (blues and greens) indicating lower efficiency.

2.6 In-Depth Analysis of U8Lite Motor

2.6.1 Motor Efficiency and Loss Maps

The U8Lite motor was subjected to a more comprehensive analysis, as it was the primary candidate for our ankle design. Its selection was predominantly based on its size specifications, a decision that will be elaborated upon in the subsequent chapter on ankle design. We conducted tests at both 24V and 36V, as these voltages represent an optimal balance between battery pack size and weight for our application. While the motor is capable of operating at 48V, the resulting battery would be prohibitively large and heavy for our purposes.

The rationale for exploring higher voltages stems from the generally improved performance characteristics of these motors at elevated voltages, including enhanced torque output, higher achievable speeds, and increased overall efficiency. However, the potential benefits must be balanced against the added weight of the larger battery required. This trade-off necessitated a comparative analysis between 24V and 36V operations to determine if the performance gains at higher voltage justify the increased power source weight.

This investigation aims to provide insights into the optimal voltage selection for our specific application, balancing the enhanced motor capabilities against the practical constraints of the overall system design. By quantifying the performance differences between these two voltage levels, we can make an informed decision on whether the improved motor characteristics at 36V outweigh the additional weight and complexity of the power supply system. Figure 2-7 and Figure 2-8 illustrate the motor efficiency and loss maps for the two voltage conditions.

As mentioned, in mobile applications, operating the motor within the high-efficiency region is highly desirable to optimize battery usage. The efficiency maps visualize the ratio of the output mechanical power to the input electrical power across operating points. Higher efficiency areas indicate less electrical power is being dissipated as heat. From the results depicted in Figure 2-7 and Figure 2-8, this region is observed to span speeds ranging from 200 RPM to 700 RPM, with torque values below 1 Nm.

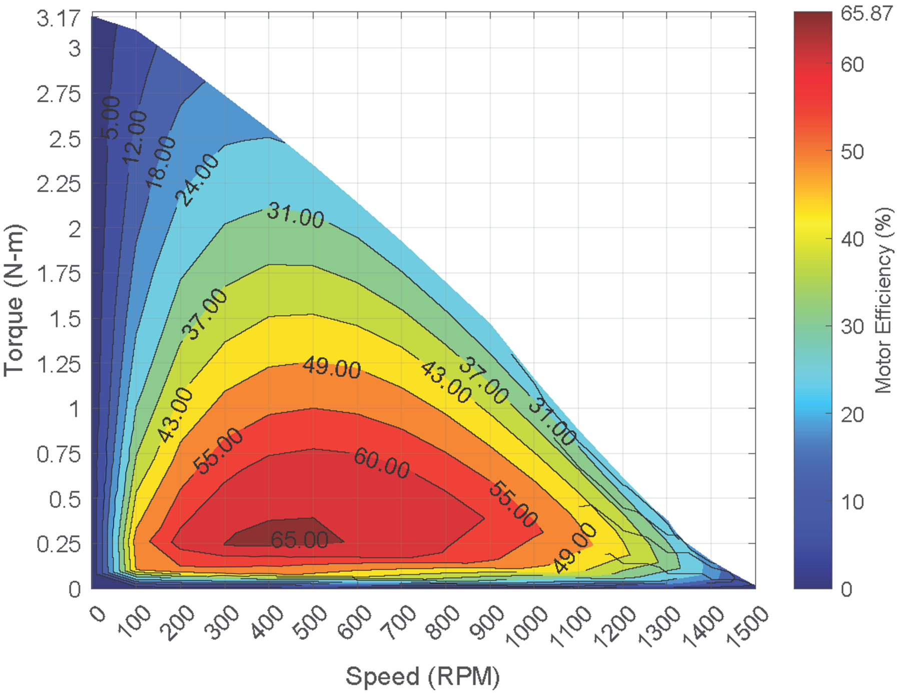

(a) Efficiency map

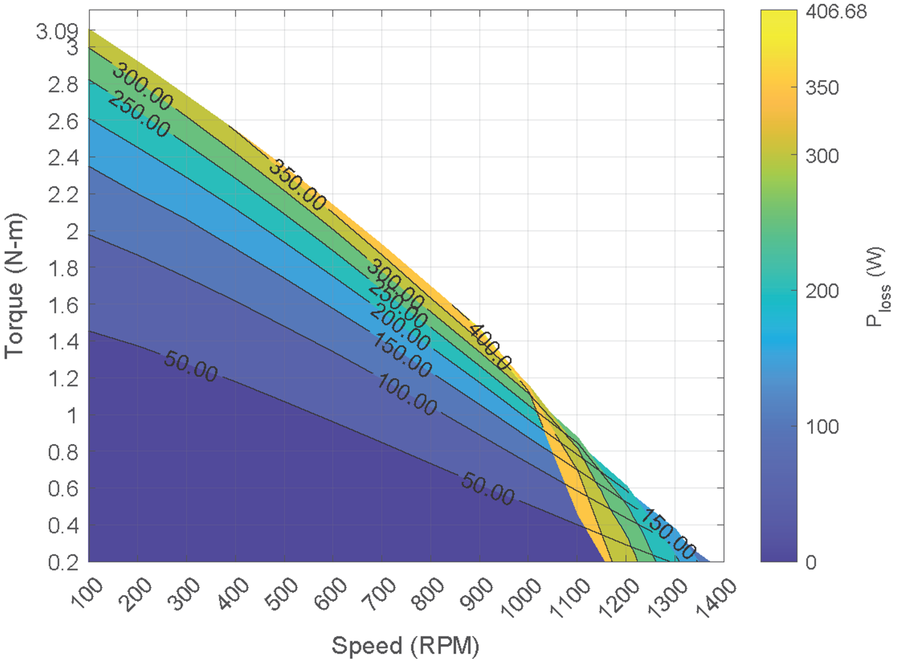

(b) Loss map

Figure 2-7: Efficiency and loss maps for U8Lite motor at 24V. (a) Efficiency map; (b) Loss map. Color gradients represent efficiency levels and loss magnitudes respectively.

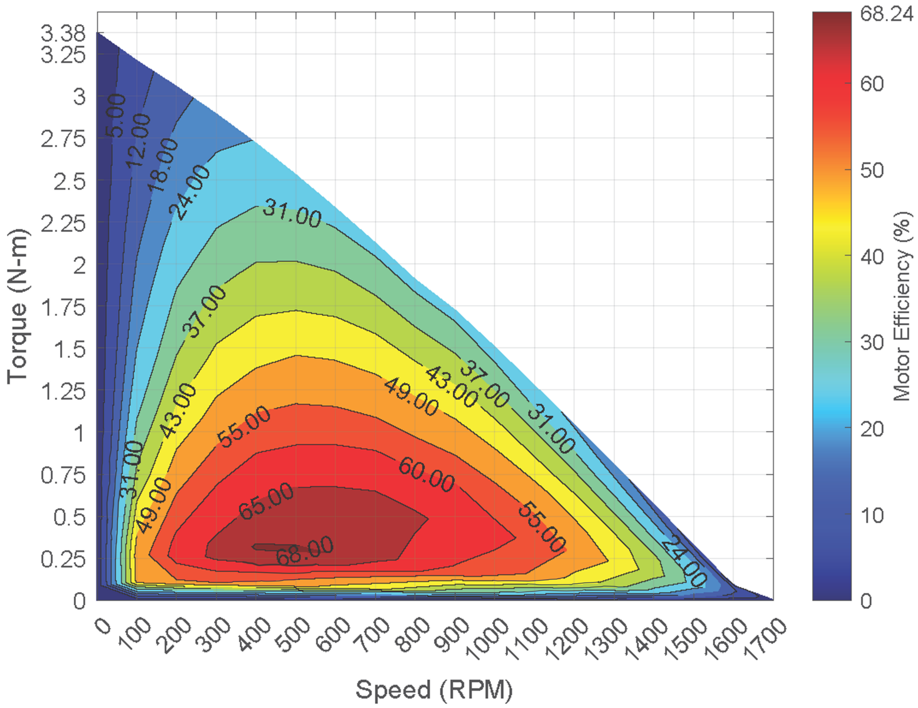

(a) Efficiency map

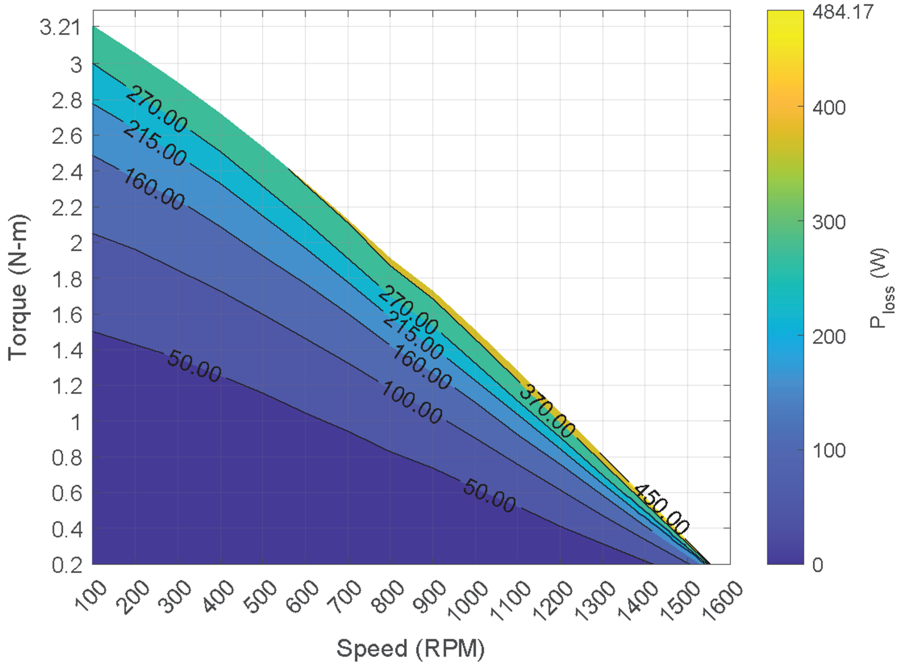

(b) Loss map

Figure 2-8: Efficiency and loss maps for U8Lite motor at 36V. (a) Efficiency map; (b) Loss map. Color gradients represent efficiency levels and loss magnitudes respectively.

Furthermore, these efficiency maps can also provide information on how to momentarily exceed the motor's power rating and ascertain the torque and speed limits that the motor can achieve.

The loss maps provide information about the power dissipation in the motor at different operating points. However, it is important to note that the loss maps for the motor do not include the zero current and zero velocity operating points. These operating points were excluded because at zero speed, the motor does not produce any output mechanical power and, at zero current, the motor does not apply any torque. Therefore, including these points in the loss maps would not provide meaningful information about power dissipation. Nonetheless, the data from these points were included in the motor efficiency maps to provide a comprehensive view of the motor's performance, including its maximum torque and speed capabilities. Further, under the 24 V condition, there are certain operating points, particularly at 1200 RPM and above, where the motor was unable to generate any positive torque. As a result, all the electrical power input was considered as loss, resulting in an irregular pattern in the loss map depicted in Figure 2-7b at high speeds.

It is evident that operating the U8Lite KV100 motor at 36 V yielded improved performance compared to 24 V. When comparing the efficiency maps between the 24 V and 36 V conditions, it can be observed that the torque outputs were approximately 5% to 10% higher for speeds up to 600 RPM and 10% to 25% higher for speeds above 600 RPM. This indicates that the motor can generate higher levels of torque at higher operating voltages. Notably, under the 36 V condition, the motor exhibited the capability to generate torque even at higher speeds. Table 2.1 provides a more detailed comparison of the increase in torque generated by the motor at 36 V compared to 24 V. In addition to higher torque generation, the motor also exhibited higher efficiency under the 36 V condition. Furthermore, the area of the high-efficiency region was larger when operating the motor at 36 V.

Table 2.1: Percentage increase in torque at selected operating points, comparing 36 V to 24 V.

	200 RPM	**400 RPM**	**600 RPM**	**800 RPM**	**1000 RPM**
2 A	5.11%	9.68%	15.5%	25.11%	67.98%
4 A	3.73%	6.69%	10.36%	14.92%	29.03%
5 A	4.34%	6.79%	10.79%	16.34%	29.81%
10 A	3.86%	6.01%	9.22%	13.6%	24.05%
15 A	3.79%	6.06%	9.06%	12.91%	23.08%
20 A	3.95%	6.1%	8.94%	12.83%	23.02%
25 A	4.15%	6.33%	9.00%	12.86%	22.81%
30 A	4.45%	6.5%	9.2%	12.79%	22.78%
35 A	4.59%	6.68%	9.32%	12.76%	22.79%
40 A	4.74%	6.78%	9.32%	12.68%	22.65%
45 A	4.79%	6.83%	9.28%	12.71%	22.44%
50 A	4.72%	6.87%	9.12%	12.53%	34.47%

2.6.2 Motor Driver Efficiency Maps

As the primary focus of this study was to evaluate the motor's performance, it was crucial to ensure that the motor driver did not impede the motor's capabilities. To mitigate this, the driver was affixed to an aluminum plate, and a low-profile CPU cooler (C7 Cu, Cryorig, New Taipei City, Taiwan) was mounted on the plate. However, it is important to acknowledge that this thermal management solution may not be feasible for mobile applications due to weight and size considerations. Therefore, for mobile applications, it is recommended to conduct further tests to assess the thermal properties of the motor drive under various cooling methods. Figure 2-9 presents the efficiency maps for the EVEREST XCR-C motor driver at the two voltage conditions. The results obtained aligned with the energy efficiency specifications provided by the vendor [37]. The driver efficiency maps do not incorporate the zero current and zero velocity operating points for the same reason as the loss maps.

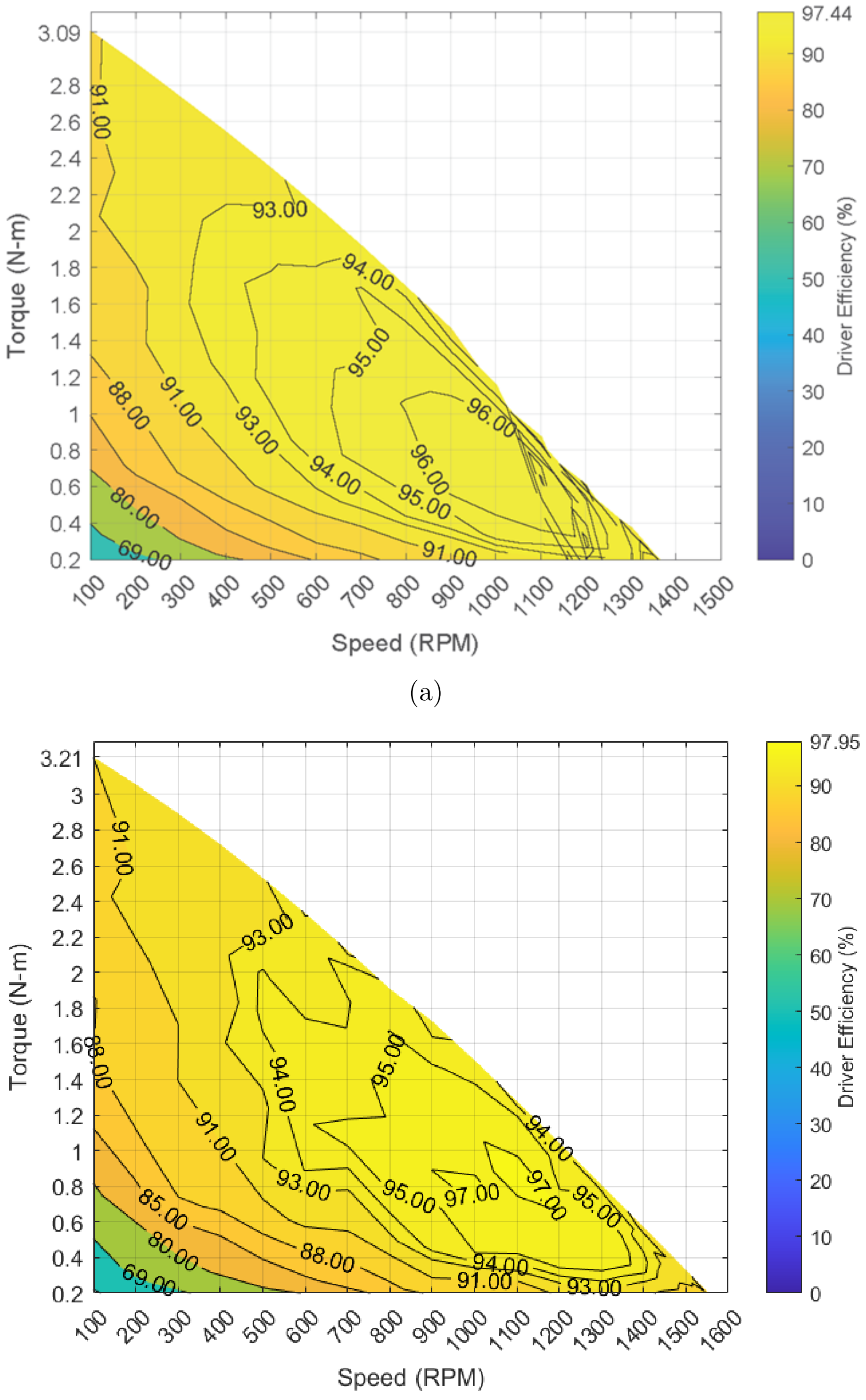

(a)

(b)

Figure 2-9: The efficiency maps of the EVEREST XCR-C motor driver at (**a**) 24 V and (**b**) 36 V.

2.6.3 Motor Thermal Responses

Joule heating within the motor's windings significantly impacts the motor's performance. This thermal effect, caused by the resistance of the windings to the electric current, can lead to increased temperatures, potentially affecting the efficiency and longevity of the motor. Therefore, monitoring the temperature of the windings is crucial to ensure the motor is operated within safe limits when overpowering it. As mentioned earlier, during the tests at each operating point, the motor did not receive any active cooling and was only cooled after the test was completed. It is important to note that the motor should not exceed a temperature of 95 °C at any point during operation. Figure 2-10 illustrates the maximum temperature reached by the motor under both the 24 V and 36 V operating conditions.

These data provide assurance that briefly exceeding the motor's power rating for a limited duration is acceptable within the specified thermal limits. Furthermore, Figure 2-11 displays the thermal responses of selected operating points, providing additional insights into the temperature behavior of the motor.

Upon comprehensive analysis of the thermal behavior, it becomes clear that the introduction of a higher voltage triggered a more accelerated rise in temperature, culminating in greater peak temperatures. Nonetheless, throughout the span of the 3.5 s test interval, this amplified temperature did not significantly affect the efficiency of the motor. Under the 36 V condition, the temperature peaked at approximately 57 °C when operating at high current setpoints, which remained comfortably below the specified limit of 95 °C.

In real-world applications where the motor might need to be momentarily overpowered, it is crucial to continuously monitor the temperature. The motor drive incorporates an I^2T protection system, which acts as a safety measure against situations where the instantaneous thermal energy surpasses a predetermined limit. This is vital as temperature sensors may not be quick enough to identify potentially hazardous conditions.

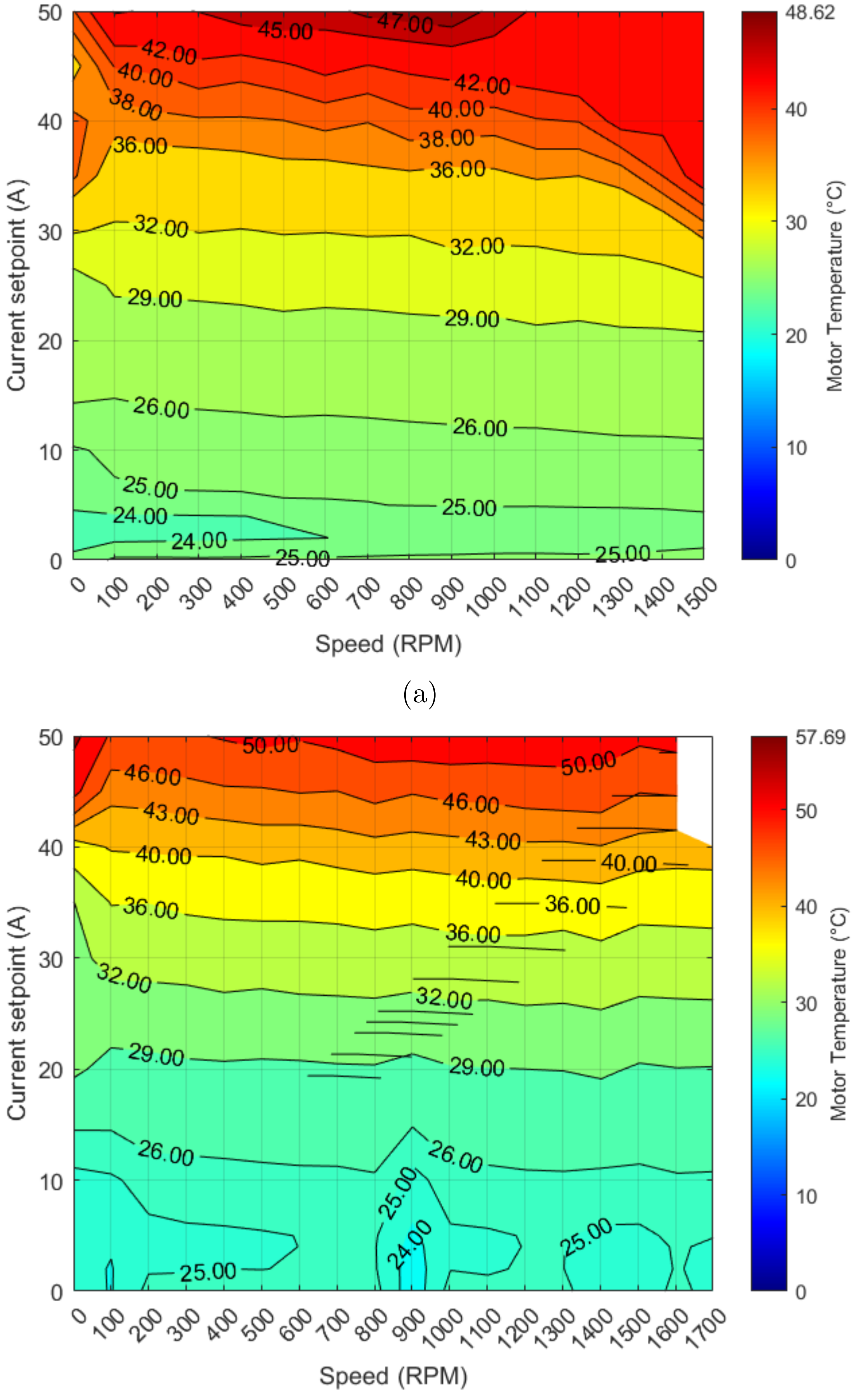

(a)

(b)

Figure 2-10: (**a**) Maximum temperature at each operating point for 24 V. (**b**) Maximum temperature at each operating point for 36 V. Please note that temperature data for the 45 A and 50 A current setpoints at 1700 RPM were not collected due to the activation of the I^2T protection.

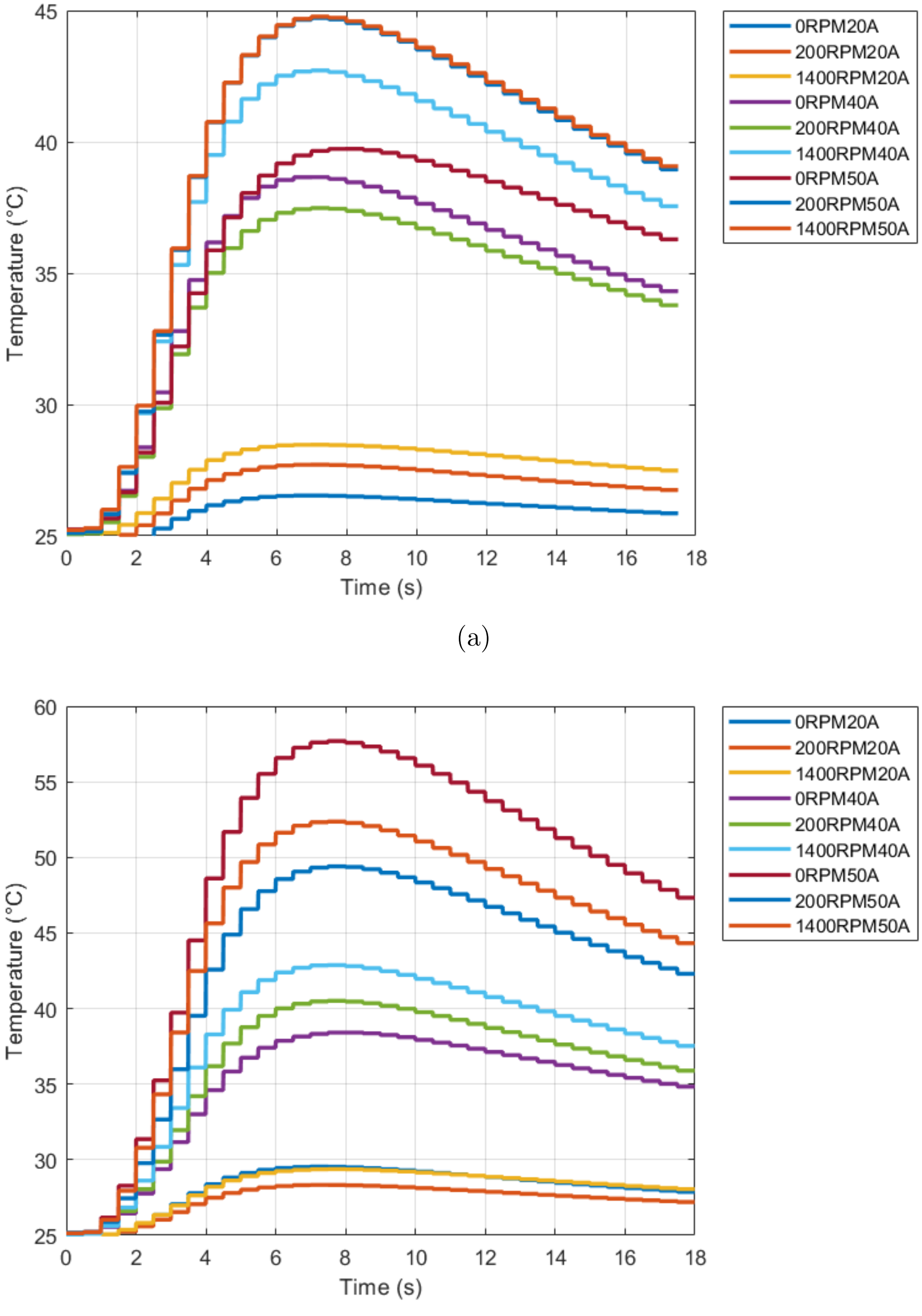

(a)

(b)

Figure 2-11: Thermal responses of the motor. (**a**) Thermal responses for selected operating points under 24 V. (**b**) Thermal responses for selected operating points under 36 V. The accelerated heating with higher current aligns with the greater resistive power dissipation predicted by Joule's first law.

The instantaneous energy that the motor releases is directly proportional to the square of the current flowing through it and the time this current persists. The "nominal current" is defined as the maximum current that a motor can sustain continuously without breaching its thermal boundaries. Any current that goes beyond this nominal value results in an accumulation of thermal energy within the motor and its surroundings, which then needs to be dissipated by the cooling system.

If the thermal energy buildup exceeds the cooling system's dissipation capacity, the system could reach its thermal limits, posing a risk of irreversible damage to the motor or the drive. The I^2T principle is associated with a value that is inversely proportional to the energy that the motor dissipates. The I^2T protection system serves as a control mechanism to ensure that the total power that the motor releases as thermal energy does not go beyond its thermal constraints. [38].

2.7 Setup for High Torque Measurement

A high-torque variant of the testbed was designed and constructed, as illustrated in Figure 2-12. This iteration was developed to facilitate the testing of integrated actuators, which comprise both a motor and a gearbox. The fundamental setup remains largely consistent with the original design, with one notable exception: the driving motor has been replaced with a magnetic powder brake (TPB 200, Magtrol, Buffalo, NY, USA), capable of providing up to 200 Nm of braking torque.

Initially, we explored the possibility of incorporating a 10:1 gearbox on the driving motor. However, this configuration was found to be suboptimal due to the excessive reflected inertia it introduced. Given that the primary function of the driving motor is to establish and maintain speed, any significant resistance to back-driving could potentially lead to damage in either the actuator's gearbox or the driving motor itself.

To accommodate the high-torque requirements of this setup, we integrated a torque sensor with a 500 Nm capacity (TRS705 FSH02570, Futek, Irvine, CA, USA). This sensor enables precise measurement of the substantial torques generated in this modified testbed configuration. This enhanced testbed design allows for more comprehensive evaluation of integrated actuator systems, providing valuable insights into their performance characteristics under high-torque conditions.

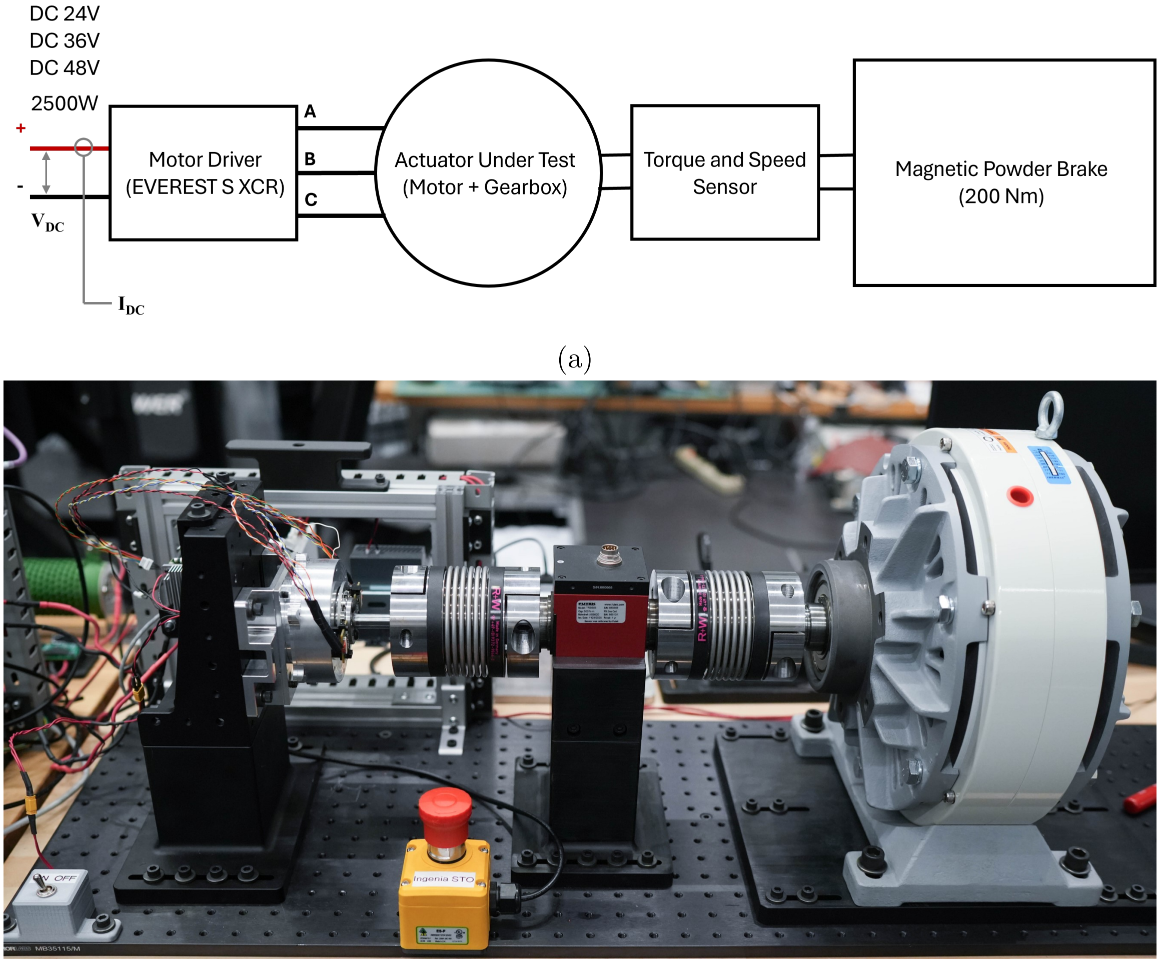

(a)

(b)

Figure 2-12: Overview of the experimental apparatus designed for high torque measurement. (**a**) Diagram representing the key components. (**b**) Physical realization of the system.

2.8 Conclusion

The comprehensive characterization of human-scale actuators presented in this chapter offers valuable insights into the performance and capabilities of exterior-rotor brushless motors, particularly the U8Lite KV100, T-motor RI 50 KV100, and T-motor R60 KV115. Through rigorous testing and analysis, we have developed detailed efficiency maps, loss maps, and thermal response profiles that provide a nuanced understanding of these motors' behavior across various operating conditions.

Key findings include:

1. The performance of the U8Lite KV100 motor at 36V compared to 24V, with higher torque outputs and improved efficiency across a wider range of operating points.
2. The importance of thermal management in motor operation, particularly when considering short-duration overpowering scenarios.
3. The effectiveness of the EVEREST XCR-C motor driver, which demonstrated high efficiency aligned with manufacturer specifications.
4. The development of a high-torque testbed variant, expanding our capability to evaluate integrated actuator systems under more demanding conditions.

These results provide crucial information for the selection and application of these motors in various robotic systems, particularly in scenarios requiring high power output for brief durations. The detailed efficiency maps and thermal profiles offer valuable guidance for optimizing motor performance while ensuring safe operation within thermal limits. Furthermore, the custom software tools developed for this study, including the dynamometer control interface and data analysis software, represent important contributions to the field. These tools streamline the testing process and enable more in-depth analysis of motor performance data.

While this study provides a comprehensive characterization of these motors, it also highlights areas for future research. These include further investigation into thermal management strategies for mobile applications, extended testing of integrated actuator systems using the high-torque testbed, and exploration of motor performance under varying environmental conditions.

In conclusion, this chapter presents a robust methodology for motor characterization and provides valuable data that can inform the design and optimization of actuators in a wide range of robotic applications. The insights gained from this study will contribute to the ongoing efforts to enhance the efficiency and effectiveness of robotic systems, particularly in applications requiring precise control and high performance within constrained operational parameters.

Chapter 3

Bionic Ankle Design

3.1 Introduction

Building upon the comprehensive characterization of human-scale actuators presented in the previous chapter, we now turn our attention to the design of an innovative 2DoF powered ankle-foot prosthesis. This chapter will detail the mechanical design, kinematics modeling, and force sensing strategies employed in the development of this advanced bionic ankle.

Our design aims to address several key challenges in the field of powered prosthetics. We strive to achieve biological fidelity in range of motion, torque output, and angular velocity while incorporating active control in both sagittal and frontal planes. Simultaneously, we aim to maintain a weight comparable to the biological ankle-foot complex and ensure compatibility with advanced neural interfaces like AMI and eOPRA.

The following sections will outline our approach to these challenges. We will discuss the selection and integration of actuators based on the characterization study, as well as the mechanical design principles employed to achieve the desired degrees of freedom. Our exploration of kinematic modeling to optimize the prosthesis' range of motion and force output will be presented, along with our strategies for precise force sensing to enable responsive control.

By detailing these aspects of our design process, we aim to provide insights into the development of next-generation prosthetic devices that can fully leverage the capabilities of advanced surgical techniques and push the boundaries of bionic limb technology.

3.2 Specifications

To provide a comprehensive overview of the design, we begin with a visual representation of the system. Figure 3-1 presents a detailed 3D CAD rendering, illustrating the key components of the prosthesis. This visual aid elucidates the spatial arrangement and integration of critical elements within the compact design. Figure 3-2 complements the CAD model with a photograph of the physical implementation, offering a tangible representation of the realized prototype.

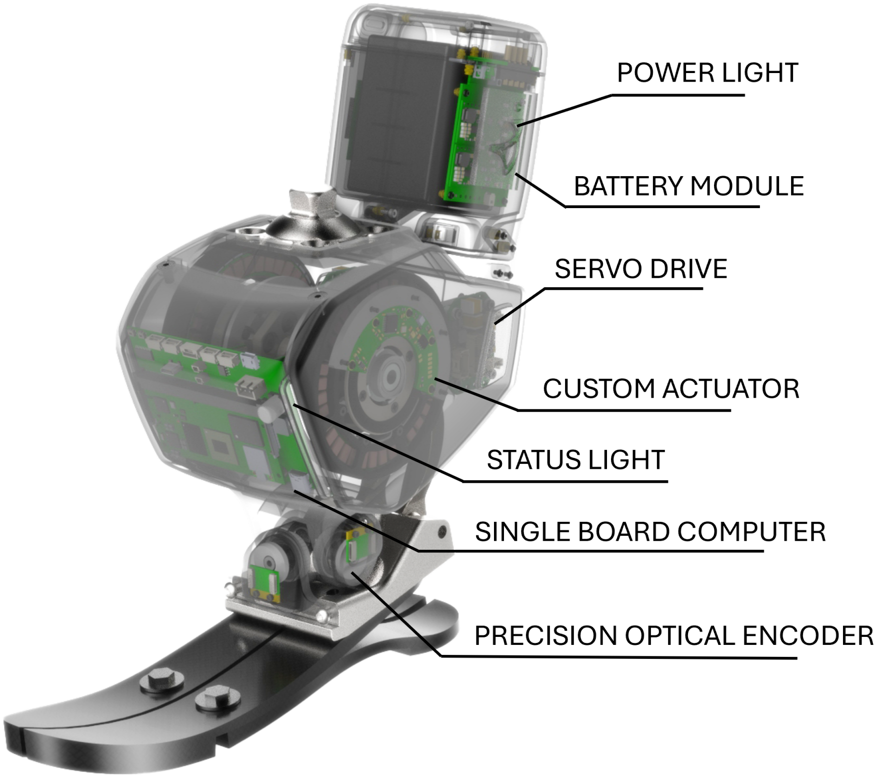

Figure 3-1: CAD rendering of the 2DoF ankle-foot prosthesis illustrating key components.

Figure 3-2: Photograph of the physically implemented 2DoF ankle-foot prosthesis prototype.

Our design achieved specific ranges of motion and torque outputs that approach the capabilities of a natural ankle. Table 3.1 summarizes the key specifications of the bionic ankle prosthesis.

These specifications indicate the device's range of motion in both the sagittal and frontal planes, which may contribute to navigation across various terrains and activities. The torque outputs enable movements that could be relevant for tasks such as stair climbing and jogging. The ankle range of motion in the sagittal plane is typically between 65° and 75°, moving from 10° to 20° of dorsiflexion through to 40°-55° of plantarflexion. However, for everyday activities, a reduced range is sufficient: approximately 30° for walking, and 37° and 56° for ascending and descending stairs, respectively. In the frontal plane, a total range of motion of about 35° (23° inversion

Table 3.1: Specifications of the 2DoF Bionic Ankle Prosthesis

Parameter	**Value**
Plantarflexion	50°
Dorsiflexion	30°
Inversion	35°
Eversion	35°
Peak plantar/dorsi torque (10 seconds)	190 Nm (@40 A)
Max plantar/dorsi torque (3 seconds)	240 Nm (@50 A)
Peak inversion/eversion torque (10 seconds)	50 Nm (@40 A)
Max inversion/eversion torque (3 seconds)	63 Nm (@50 A)
Weight without battery	3.1 kg
Battery weight	0.3 kg
Build height	200 mm
Build width	104 mm

+ 12° eversion) is typical [39]. However, we designed the range of motion to be larger than these typical values, as ankle range of motion can vary significantly between individuals due to geographical and cultural differences based on their activities of daily living [39]. This expanded range ensures our prosthesis can accommodate a wider variety of users and activities. Figure 3-3 demonstrates the prosthetic ankle's range of motion in the frontal plane.

The design incorporates two custom actuators, selected based on our previous analysis to provide performance within the space constraints. While these actuators contribute significantly to the overall weight, they are essential for achieving the desired functionality. Each actuator is controlled by a servo drive, aiming for precise control and responsiveness to user inputs and environmental changes. A custom single board computer is integrated into the prosthesis, serving as the central processing unit for control algorithms and sensor data integration. This computational element is designed to handle the calculations necessary for neural commands and responses to various terrains and activities.

For precise position sensing and spring deflection measurement, the design incorporates four high-precision optical encoders. Two encoders are positioned at the

Figure 3-3: Demonstration of a powered prosthetic ankle's range of motion in the frontal plane. This highlights the device's capability to adjust in the frontal plane, allowing for adaptation to uneven terrain and improved stability during various activities.

output of each actuator, while the other two are located at the joints. These sensors serve dual purposes: they provide crucial feedback for closed-loop control, enabling accurate adjustments in ankle orientation and movement, and they also measure the deflections of the series springs. This dual functionality allows for comprehensive monitoring of the prosthesis's mechanical state, enhancing control accuracy and responsiveness. Power management is addressed through a custom battery module, weighing 0.3 kg. The design includes a power indicator light for monitoring the device's energy status.

The total weight of 3.4 kg (including the battery) represents the current state of miniaturization and weight reduction in this design. While this weight approaches that of a biological ankle-foot complex, it's important to note that a key design principle is to make the prosthesis as light as possible. Future iterations will focus on further weight reduction without compromising functionality.

The prosthesis has a compact form factor, with a build height of 200 mm and a width of 104 mm. These dimensions have been carefully optimized to minimize the overall size of the device. The shorter build height is crucial as it allows the prosthesis to be fitted to a wider range of individuals, particularly beneficial for those with unilateral lower-limb loss. The narrow width is designed to prevent interference with the contralateral leg during gait. These size considerations are part of the ongoing effort to create a prosthesis that is as compact and functional as possible, prioritizing adaptability and ease of use for the wearer.

3.3 Custom Integrated Actuator

3.3.1 Actuator Performance Requirements

The ankle prosthesis incorporates two custom integrated actuators configured in a differential drive arrangement. Synchronized operation of these actuators facilitates plantar or dorsiflexion, while differential actuation enables inversion and eversion movements. An undergraduate researcher, Robert Frei, contributed to the design of the actuator.

To determine the actuator specifications, we first analyzed the requisite torque and speed parameters. We utilized open-source data for walking on inclines and declines at various speeds [40], as well as stair ascent data [41]. To ensure compliance with torque-speed requirements, we plotted these data on a graph with joint velocity on the x-axis and joint torque on the y-axis. We then superimposed the combined torque-speed curve of both actuators to verify complete coverage of the operational range. It's important to note that the torque shown in Figures 3-4 and 3-5 represents the combined output of the two actuators in our 2DoF design. This combined torque capability allows our prosthesis to meet the demanding requirements of various walking conditions. The U8Lite KV100 motor was selected primarily due to its suitable diameter and length for our design constraints. Subsequently, we determined the optimal gear reduction ratio. Our analysis indicated that a 39:1 ratio would sufficiently meet the performance requirements.

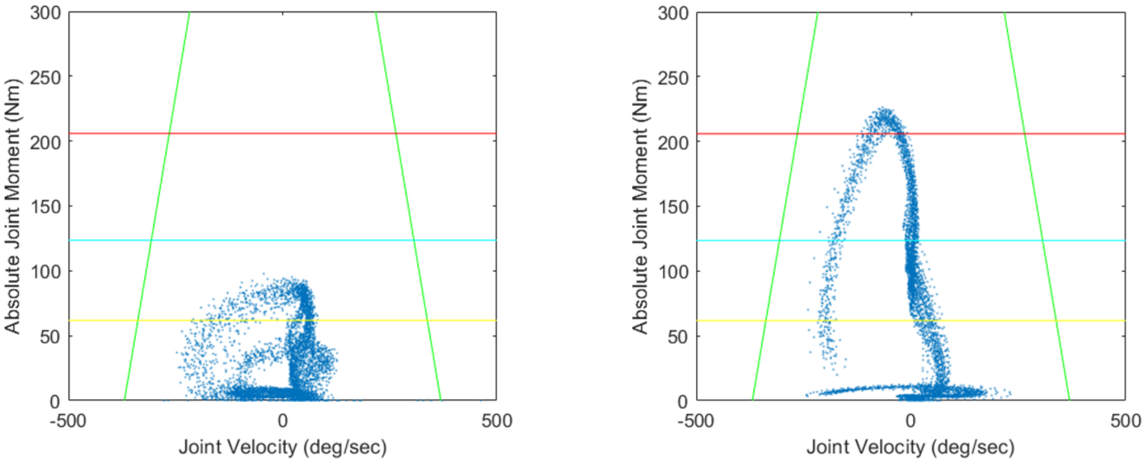

(a) 0.8 m/s 10° decline

(b) 0.8 m/s 10° incline

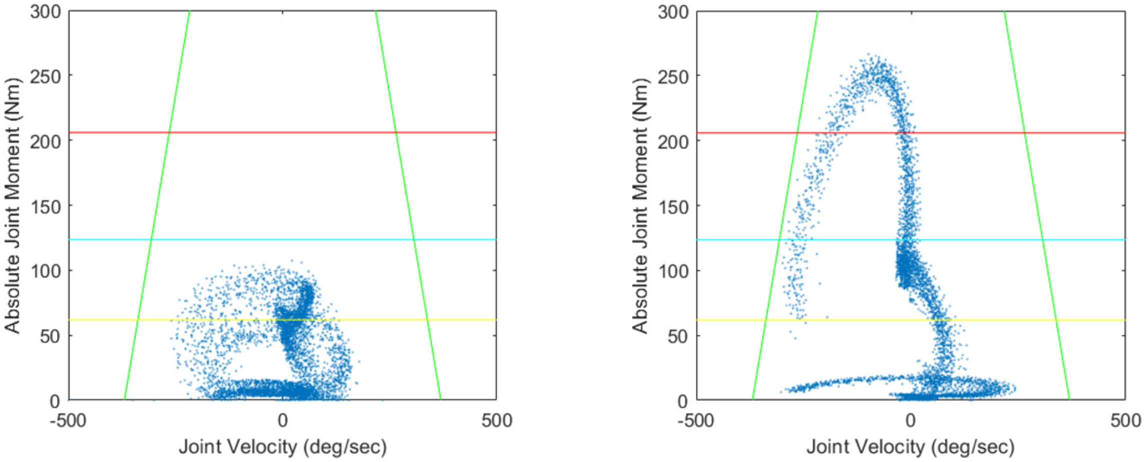

(c) 1.2 m/s 10° decline

(d) 1.2 m/s 10° incline

Figure 3-4: Torque-speed plots for walking on inclines and declines at different speeds. Blue dots represent human ankle joint data, green lines show the actuator's torque-speed slope, and horizontal lines indicate current limits (red: 40A, cyan: 24A, yellow: 12A).

Figure 3-4 illustrates the torque-speed plots for walking on inclines and declines at speeds of 0.8 m/s and 1.2 m/s. The graphs depict the relationship between joint velocity (in degrees per second) and absolute joint moment (in N-m) for four conditions: 10° decline and incline at both 0.8 m/s and 1.2 m/s. Blue dots represent human ankle joint data, while the green lines show the torque-speed slope of the actuator. Horizontal lines indicate current limits at 40A (red), 24A (cyan), and 12A (yellow).

Figure 3-5 depicts the data for stair ascent. In this graph, the additional red dashed line indicates the current at 60A, which represents the theoretical maximum that we won't use in practice. This 60A limit is shown to illustrate the actuator's absolute maximum capability, though our design operates within more conservative current limits for safety and longevity.

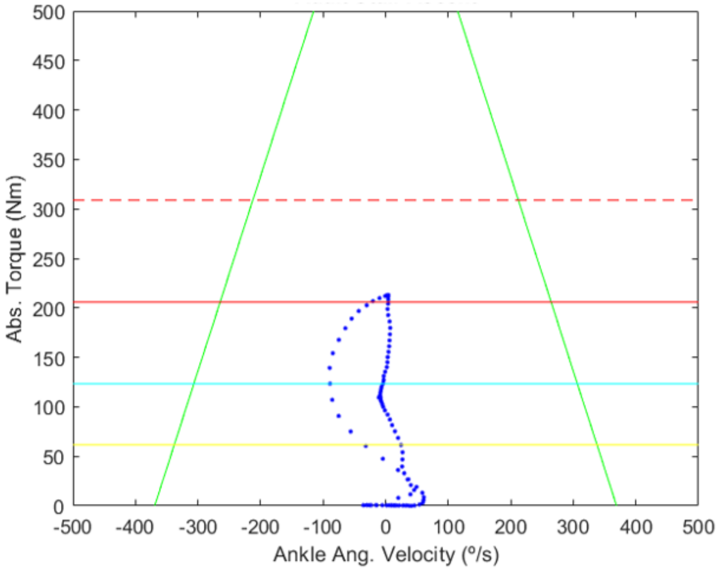

Figure 3-5: Torque-speed plot for stair ascent. Blue dots represent human ankle joint data, green lines show the actuator's torque-speed slope, and horizontal lines indicate current limits (red dashed: 60A, red: 40A, cyan: 24A, yellow: 12A).

3.3.2 Gear Design

Based on our comprehensive analysis of torque-speed requirements, we determined that a 39:1 gear reduction ratio would be optimal for our actuator design. To achieve this ratio while maintaining a compact form factor, we developed a custom two-stage planetary gear drive that integrates seamlessly within the motor's stator housing. This innovative approach significantly contributes to the overall compactness of our prosthetic ankle design.

The primary consideration in designing the gear drive was ensuring its capacity to effectively transmit the required torque. This necessitated a thorough evaluation of two critical stress factors: bending stress and contact stress [42]. These stress analyses are crucial for predicting gear performance and longevity under the expected load conditions.

To quantify these stresses, we employed standard gear stress equations. The bending stress number s_t is calculated using:

$$s_t = \frac{W_t P_d}{FJ} K_o K_s K_m K_B K_v \tag{3.1}$$

where W_t is the tangential force, P_d is the diametral pitch, F is the face width, J is the geometry factor, and K_o, K_s, K_m, K_B, and K_v are modification factors for overload, size, load distribution, rim thickness, and dynamic effects respectively [42].

The contact stress number (s_c) is determined by:

$$s_c = C_p \sqrt{\frac{W_t K_o K_s K_m K_v}{F D_p I}} \tag{3.2}$$

where C_p is the elastic coefficient, D_p is the pitch diameter, and I is the geometry factor for pitting resistance. The other variables are consistent with the bending stress equation [42].

In our design process, we implemented a safety factor of two for both bending and contact stress calculations. By carefully analyzing these stress factors, we were able to optimize our gear design for the specific requirements of our prosthetic ankle. This involved balancing the need for strength and durability with the constraints of size and weight. The bending stress analysis ensures the gear teeth can withstand the cyclic loading without fracture, while the contact stress analysis helps predict and minimize surface fatigue and wear.

Figure 3-6 presents our custom actuator design. The 3D CAD model (Figure 3-6a) illustrates the compact integration of the two-stage planetary gear drive. The photograph of the physical actuator (Figure 3-6b) demonstrates the successful realization of this design, highlighting the compact nature of our solution.

The key specifications of our custom actuator are summarized in Table 3.2. These specifications demonstrate the compact and lightweight nature of our design, while also highlighting its impressive torque capabilities.

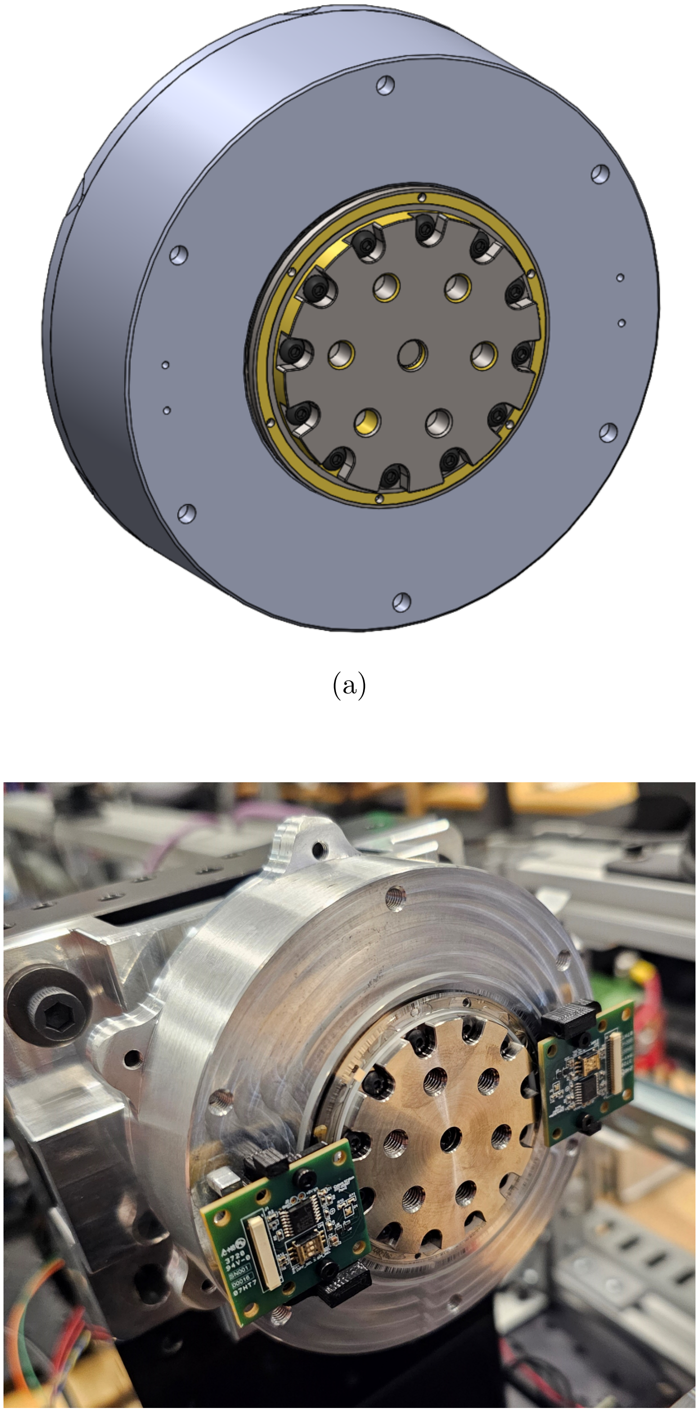

(a)

(b)

Figure 3-6: The integrated actuator: (a) 3D CAD model and (b) physical implementation

Table 3.2: Specifications of the Custom Actuator

Specification	**Value**
Diameter	100 mm
Thickness	31 mm
Weight	570 g
No-Load Speed	50 RPM
Peak Torque (40A)	95 N-m
Max. Torque (50A)	130 N-m

3.4 Transmission Design

3.4.1 Differential Drive System

The 2DoF ankle mechanism incorporates two custom-designed actuators, each of which drives a parallel four-bar linkage. These two four-bar linkages are coupled to create a differential drive system. When the actuators operate synchronously, the ankle executes motion in the sagittal plane. Conversely, any disparity in actuator movement results in motion in the frontal plane. Figure 3-7 provides a detailed illustration of the kinematic model for this mechanism.

As depicted in Figure 3-7, one of the linkages in each four-bar mechanism is modeled as a spring, effectively creating two series elastic actuators (SEAs). Since the seminal work of Pratt et al. [43], who introduced the original SEA concept in 1995, a diverse array of compliant actuator designs has emerged. SEAs have demonstrated remarkable versatility, finding applications across a broad spectrum of fields, from robotics to prosthetics [3, 44, 45, 46, 47, 48, 49, 50].

In series elastic actuators (SEAs), the stiffness of the series spring is crucial, as it affects both the system's robustness to impacts and the open-loop torque bandwidth, which in turn influences the actuator's dynamic performance. Increasing stiffness in SEAs raises the resonance frequency, thereby improving torque tracking capabilities. In the context of prosthesis design, the series spring also plays a significant role in energy storage, aiding in battery conservation and reducing the required motor size [51]. Thus, a design trade-off exists between energy storage and control bandwidth.

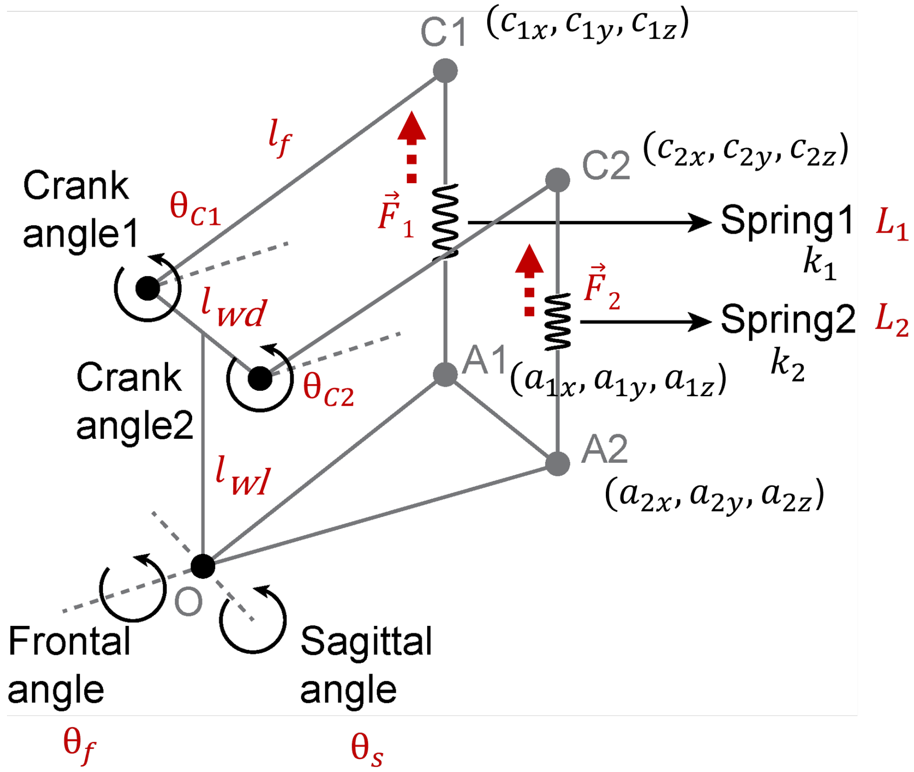

Figure 3-7: Kinematic model of a 2DoF ankle mechanism with differential drive, showing crank angles, linkage geometry, spring elements, and resulting frontal and sagittal ankle angles.

For our specific application, achieving higher bandwidth is essential. Activities such as fast walking, jogging, and jumping necessitate enhanced control bandwidth to ensure the system can accurately track the required signals. Consequently, our design choice favors higher stiffness to meet these dynamic performance requirements.

However, there are upper limits to the spring stiffness in our design. Two primary considerations inform this constraint. Firstly, we engineered the other components of the four-bar linkage to be an order of magnitude stiffer than the spring, allowing us to disregard their deformation in our analysis. Secondly, our method for sensing spring deformation relies on encoders positioned at key points: the actuators (θ_{C1} and θ_{C2}), the sagittal angle (θ_s), and the frontal angle (θ_f). If the spring were to be designed with excessive stiffness, it would impede our ability to accurately detect and measure these subtle deformations, potentially compromising the system's overall performance and responsiveness.

Building upon the aforementioned design considerations, we now present the methodology for calculating sagittal and frontal joint torques based on encoder readings. For this part, I collaborated with Hyungeun Song. Our process begins with the computation of the deformed lengths of the two springs:

$$L_1 = \sqrt{\begin{aligned}&(l_f(\cos(\theta_s) - \cos(\theta_{C1})) - \frac{l_{\mathrm{wd}}}{2}\sin(\theta_f)\sin(\theta_s))^2 \\ &+ (\frac{l_{\mathrm{wd}}}{2}(1 - \cos(\theta_f)))^2 \\ &+ (l_f(\sin(\theta_s) - \sin(\theta_{C1})) + \frac{l_{\mathrm{wd}}}{2}\sin(\theta_f)\cos(\theta_s) - l_{\mathrm{wl}})^2\end{aligned}} \tag{3.3}$$

$$L_2 = \sqrt{\begin{aligned}&(l_f(\cos(\theta_s) - \cos(\theta_{C2})) - \frac{l_{\mathrm{wd}}}{2}\sin(\theta_f)\sin(\theta_s))^2 \\ &+ (\frac{l_{\mathrm{wd}}}{2}(1 - \cos(\theta_f)))^2 \\ &+ (l_f(\sin(\theta_s) - \sin(\theta_{C2})) + \frac{l_{\mathrm{wd}}}{2}\sin(\theta_f)\cos(\theta_s) - l_{\mathrm{wl}})^2\end{aligned}} \tag{3.4}$$

Following the determination of the deformed spring lengths, we proceed to calculate the spring deformation. This step allows us to quantify the extent to which each spring has been compressed or extended from its resting state:

$$\begin{aligned}\Delta L_1 &= L_1 - l_{\mathrm{wl}} \\ \Delta L_2 &= L_2 - l_{\mathrm{wl}}\end{aligned} \tag{3.5}$$

The next step in our analysis involves the calculation of the three-dimensional positions of points $C1$, $C2$, $A1$, and $A2$. This spatial determination is essential for understanding the geometric configuration of the mechanism and forms the basis for subsequent force and torque calculations.

$$\begin{aligned}(c_{1x}, c_{1y}, c_{1z}) &= \left(\frac{l_{\mathrm{wd}}}{2}, l_f\cos(\theta_{C1}), l_{\mathrm{wl}} + l_f\sin(\theta_{C1})\right) \\ (c_{2x}, c_{2y}, c_{2z}) &= \left(-\frac{l_{\mathrm{wd}}}{2}, l_f\cos(\theta_{C2}), l_{\mathrm{wl}} + l_f\sin(\theta_{C2})\right)\end{aligned} \tag{3.6}$$

$$\begin{aligned}(a_{1x}, a_{1y}, a_{1z}) = \Big(&\frac{l_{\mathrm{wd}}}{2}\cos(\theta_f), \\ &l_f \cos(\theta_s) - \frac{l_{\mathrm{wd}}}{2}\sin(\theta_f)\sin(\theta_s), \\ &l_f \sin(\theta_s) + \frac{l_{\mathrm{wd}}}{2}\sin(\theta_f)\cos(\theta_s)\Big) \\ (a_{2x}, a_{2y}, a_{2z}) = \Big(&-\frac{l_{\mathrm{wd}}}{2}\cos(\theta_f), \\ &l_f \cos(\theta_s) + \frac{l_{\mathrm{wd}}}{2}\sin(\theta_f)\sin(\theta_s), \\ &l_f \sin(\theta_s) - \frac{l_{\mathrm{wd}}}{2}\sin(\theta_f)\cos(\theta_s)\Big)\end{aligned} \tag{3.7}$$

We then proceed to calculate the unit force vectors acting on the springs, denoted as $\vec{F_1}$ and $\vec{F_2}$:

$$\begin{aligned}\vec{F_1} = (F_{1x}, F_{1y}, F_{1z}) &= \frac{(c_{1x} - a_{1x}, c_{1y} - a_{1y}, c_{1z} - a_{1z})}{L_1} \\ \vec{F_2} = (F_{2x}, F_{2y}, F_{2z}) &= \frac{(c_{2x} - a_{2x}, c_{2y} - a_{2y}, c_{2z} - a_{2z})}{L_2}\end{aligned} \tag{3.8}$$

Utilizing the aforementioned information, we can now proceed to calculate the sagittal and frontal plane torque contributions from each spring, where k_1 and k_2 represent the respective spring stiffnesses.

$$\begin{aligned}T_{L1(\mathrm{sagittal})} &= |a_{1y}F_{1z} - a_{1z}F_{1y}| \cdot \Delta L_1 \cdot k_1 \\ T_{L2(\mathrm{sagittal})} &= |a_{2y}F_{2z} - a_{2z}F_{2y}| \cdot \Delta L_1 \cdot k_1 \\ T_{L1(\mathrm{frontal})} &= |a_{1x}F_{1z} - a_{1z}F_{1x}| \cdot \Delta L_2 \cdot k_2 \\ T_{L2(\mathrm{frontal})} &= |a_{2x}F_{2z} - a_{2z}F_{2x}| \cdot \Delta L_2 \cdot k_2\end{aligned} \tag{3.9}$$

3.4.2 Series Spring Design and Validation

In the process of designing the spring, I collaborated with an undergraduate researcher, Cunxi Jimmy Dai. Our design approach was guided not only by the upper bound of stiffness discussed in the previous section but also by two additional design objectives: ease of manufacture and adaptability of stiffness. We selected titanium alloy Ti-6Al-4V as our material of choice due to its excellent mechanical properties, including superior tensile strength and exceptional resistance to fatigue and crack propagation.

As previously emphasized, our design prioritizes force control bandwidth. For a series elastic actuator, the transfer function describing the force bandwidth in response to the maximum input motor force F_{sat} is given by [43, 3]:

$$\frac{F_s^{\max}}{F\mathrm{sat}} = \frac{k_s}{M_e s^2 + (b_e + \frac{F_{\mathrm{sat}}}{V_{\mathrm{sat}}})s + k_s} \tag{3.10}$$

The transfer function presented in Equation 3.10 characterizes the dynamic behavior of our series elastic actuator system. It relates the maximum output force of the spring ($F_s^{\max}$) to the maximum input force from the motor ($F\mathrm{sat}$), thus providing insight into the system's force bandwidth. This equation comprises several key components: k_s, the stiffness of the series elastic element, which determines the system's overall compliance and energy storage capacity; M_e, the effective mass of the system, encompassing the motor's rotational inertia and any additional mass introduced by the transmission mechanism; and b_e, the damping coefficient, accounting for various sources of energy dissipation within the system, primarily from the motor and transmission components.

Additionally, the term $\frac{F_{\mathrm{sat}}}{V_{\mathrm{sat}}}$ models the effect of back-electromotive force (back-EMF) in the motor, where V_{sat} represents the maximum achievable velocity. The denominator represents the system's characteristic equation, with s being the Laplace variable, enabling analysis of the system's frequency response.

By analyzing this transfer function, we can gain valuable insights into the system's dynamic behavior, allowing us to optimize the design for improved force control bandwidth while maintaining stability and performance across various operating conditions. For our design, we selected the series elastic stiffness k_s to be an order of magnitude lower than the other structural components in the four-bar linkage mechanism. This strategic choice of compliance results in a system bandwidth of approximately 53 Hz, which is sufficient for our application as it significantly exceeds the typical frequency content of human movement [6, 3].

For the physical spring design, we initially explored two-dimensional structures suitable for water jet fabrication. Our preliminary efforts focused on modeling various cell structures, as illustrated in Figure 3-8.

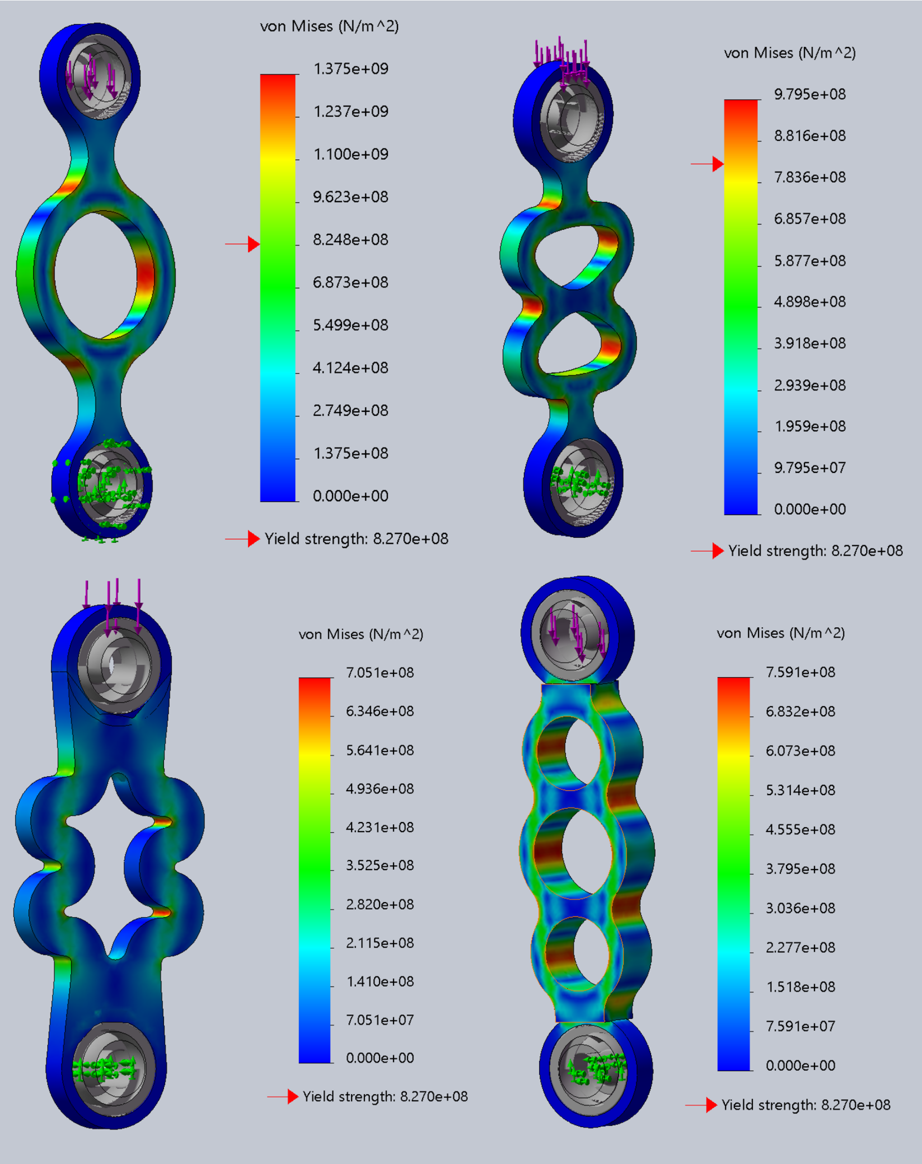

Figure 3-8: Finite element analysis of various cell-based spring designs for the series elastic actuator, using titanium alloy Ti-6Al-4V. The von Mises stress distribution is shown for each design under load, with color scales indicating stress intensity. All designs are evaluated against a consistent yield strength of 8.270×10^8 N/m^2.

Figure 3-8 figure presents finite element analysis (FEA) results for four distinct configurations of the design. These reveal that none of the proposed designs are satisfactory, as they all exhibit significant stress concentrations and exceed the material's yield strength under the applied load. The simulation was conducted with a force of 3000 N, which incorporates a safety factor above the theoretical maximum force of 2300 N. The presence of sharp transitions, tight radii, and abrupt changes in cross-sectional area contributes to the stress concentrations observed. These features act as stress risers and compromise the overall structural integrity of the components.

Following these initial results, we shifted our focus to parallel cell designs, as depicted in Figure 3-9. This alternative approach maintained a two-dimensional structure while offering the advantage of easily modifiable stiffness. The von Mises stress distributions for these designs were similar to those in Figure 3-8, and thus are not separately illustrated.

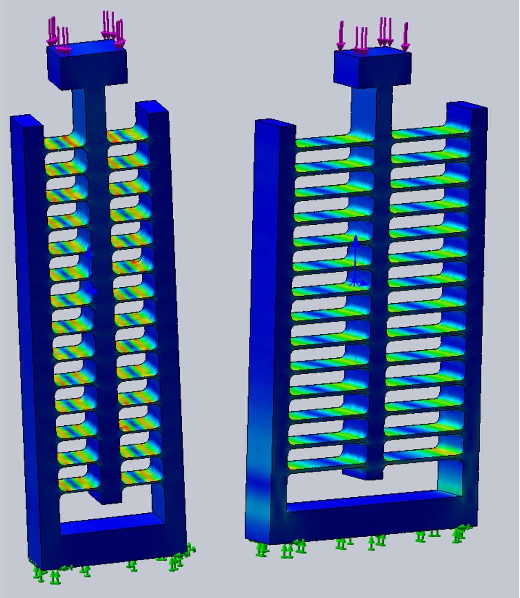

Figure 3-9: Finite element analysis of parallel cell spring designs for the series elastic actuator. The image shows two variants with different cell geometries, illustrating stress distributions under load. These 2D structures offer easily modifiable stiffness while maintaining manufacturability via water jet fabrication.

The parallel cell designs, while promising in theory for their adaptable stiffness, ultimately proved unsuitable for our application. As illustrated in Figure 3-9, finite element analysis revealed that these structures suffer from similar issues to the previous cell designs. Stress concentrations are evident at the junctions and corners of the cell structures, indicated by the color gradients. Moreover, the deformation under the applied load was excessive, compromising the spring's ability to function within the desired parameters of the series elastic actuator. These results led us to conclude that a more robust approach would be necessary to meet our design criteria, prompting further iterations and exploration of alternative geometries.

Ultimately, we abandoned the concept of 2D structures due to their inherent limitations. Our design process evolved towards a more sophisticated 3D structure defined by Bézier curves. This novel approach offered an advantage: the ability to modify stiffness through the adjustment of just two parameters. Figure 3-10 illustrates this innovative design, showcasing how the Bézier curve-based structure addresses the shortcomings of our previous iterations while providing enhanced flexibility in tuning the spring's mechanical properties.

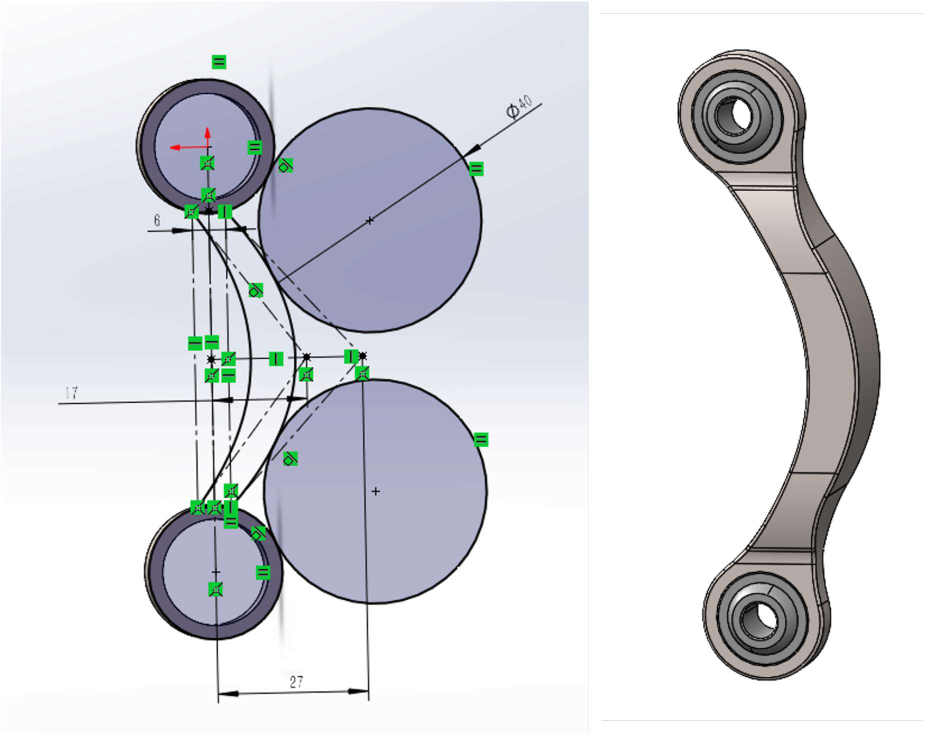

Figure 3-10: Bézier curve-based 3D spring design. Left: Parametric sketch showing the curve definition and key dimensions. Right: Resulting 3D model of the spring structure with integrated spherical bearings.

As this design no longer incorporates sharp transitions, tight radii, or abrupt changes in geometry, it demonstrates improved capability to handle the applied load without developing significant stress concentrations. The smooth, continuous curves defined by the Bézier approach allow for more uniform stress distribution throughout the structure. Figure 3-11 illustrates the FEA on the part, providing a detailed visualization of the stress distribution under load conditions.

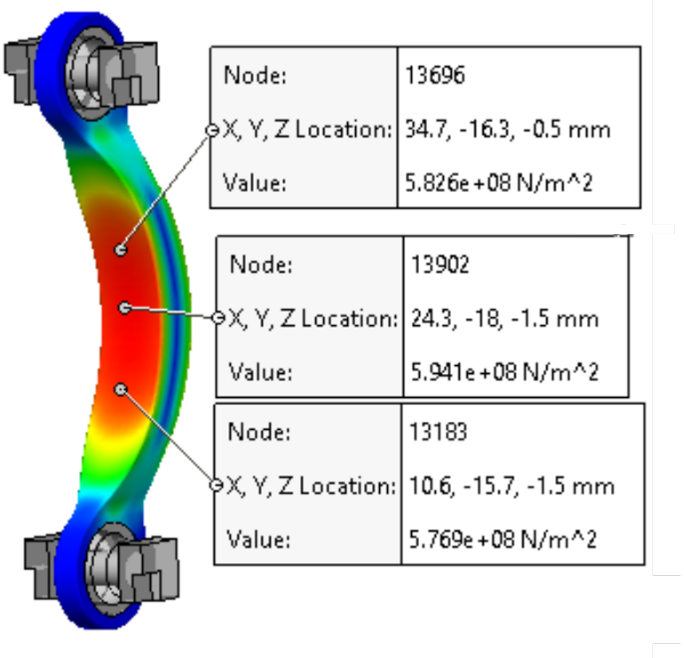

Node:	13696
X, Y, Z Location:	34.7, -16.3, -0.5 mm
Value:	5.826e+08 N/m^2

Node:	13902
X, Y, Z Location:	24.3, -18, -1.5 mm
Value:	5.941e+08 N/m^2

Node:	13183
X, Y, Z Location:	10.6, -15.7, -1.5 mm
Value:	5.769e+08 N/m^2

Figure 3-11: FEA of the Bézier curve-based spring design. Stress values and locations are provided for three critical nodes, with a maximum observed stress of 5.941×10^8 N/m^2, indicating improved performance over previous iterations.

To validate the design, we fabricated the part and conducted tension and compression tests using an Instron machine (Model 5984, Instron, Norwood, MA). Figure 3-12 illustrates the Instron testing setup and presents a comparison of the measured force-displacement data from these experiments with simulated results. To enable this comparison, we performed FEA under various loads and calculated the corresponding displacements. The resulting simulated force-displacement curve is plotted alongside the experimental data, allowing for a direct assessment of the model's accuracy and the design's performance.

(a)

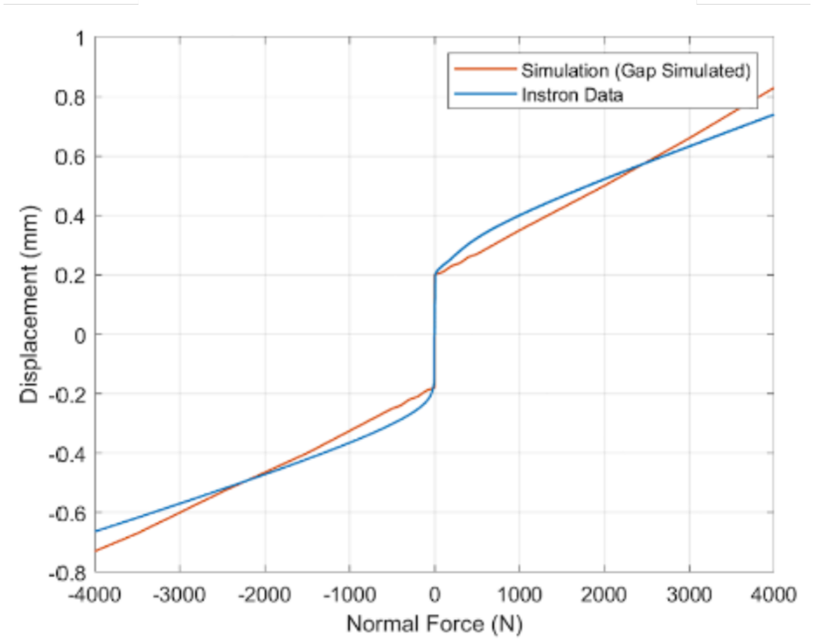

(b)

Figure 3-12: Experimental validation of the Bézier curve-based spring design: (a) Instron 5984 testing setup with the fabricated spring specimen mounted; (b) Comparison of simulated and measured force-displacement data from Instron testing.

3.4.3 Issues and Improvements

As illustrated in Figure 3-12b, there exists a range where force is applied without corresponding changes in displacement. This phenomenon is attributable to the clearance present in the spherical bearings. Such a ”dead zone” in measurement potentially compromises our force sensing precision. While we anticipated this effect, we initially posited that the addition of body weight would preload the clearance when the prosthesis makes contact with the ground. However, we encountered an unforeseen complication: the backlash in the gearbox was significantly larger than expected (0.15 mm). The combination of this backlash and the bearing clearance resulted in an exceptionally large dead zone, surpassing the maximum spring deflection. Consequently, detecting any spring deflection became extremely challenging.

To address these issues, we implemented three key modifications, each targeting a specific aspect of the system’s performance:

1. **Gear-housing tolerance optimization:** Through consultation with the gear manufacturer, we discovered that precisely matching the tolerances between the gears and the housing could significantly reduce backlash to 0.05 mm. This improvement was achievable without necessitating an upgrade in gear precision, offering a cost-effective solution to enhance system performance.

2. **Preloading mechanism integration:** We incorporated strategically placed mounting holes into the housing design, enabling the installation of an extension spring. This spring serves to preload both the actuator output and one of the spherical bearings, as illustrated in Figure 3-13. The spring mounting locations were meticulously calculated to ensure equivalent spring force at both ends, thereby minimizing any potential imbalance in the system.

3. **Series spring redesign:** We fabricated new series springs with significantly lower stiffness, resulting in a force bandwidth of 16 Hz. While this represents a reduction from our initial design, it remains well above the biomechanical requirements for level ground walking, which is approximately 9 Hz [3]. This

modification allows for greater sensitivity in force detection while still maintaining a substantial margin above physiological demands.

These modifications synergistically enhanced our ability to detect spring deflection, even in the presence of residual backlash or clearance. The preloading mechanism, in particular, helps to take up any remaining slack in the system, ensuring that even small deflections can be accurately measured. The lower stiffness springs provide a larger deflection for a given force, further improving measurement sensitivity. Collectively, these changes have significantly improved the robustness and reliability of our force sensing mechanism, addressing the initial challenges we encountered with the ”dead zone” in measurement.

As of this writing, the aforementioned modifications have been completed in both the design and manufacturing phases. The redesigned parts have been successfully fabricated. However, we have not yet assembled a new ankle prosthesis incorporating these upgrades. Consequently, our control implementation relies solely on open-loop strategies. A more comprehensive discussion of these control methods and their implications will be presented in Chapter Four.

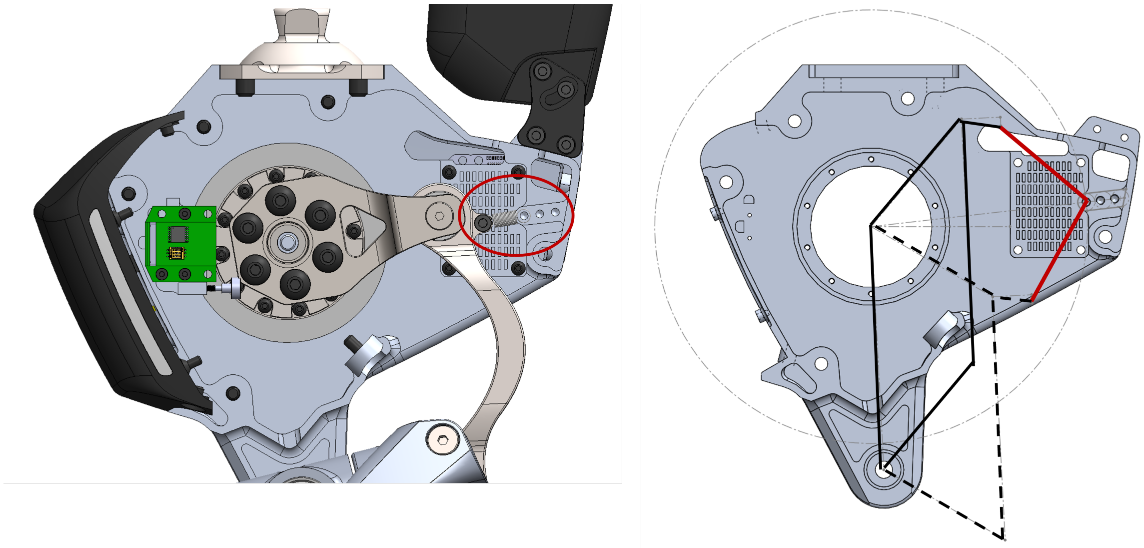

Figure 3-13: Modification to address backlash and clearance issues. Left: Internal view of the prosthetic device showing the extension spring mounting location (circled in red). Right: Schematic diagram illustrating the spring placement and force distribution to preload the actuator output and spherical bearing.

3.5 Battery and Power Management Module

The ankle is powered by a custom-designed battery module. Cunxi Jimmy Dai contributed to the design of the battery housing. Figure 3-14 illustrates the battery module design. The power source consists of a 6-cell Lithium Polymer (LiPo) battery (MA-2000-6s-Lipo-Pack, MaxAmps, USA). This battery operates at a nominal voltage of 22.2 V and can deliver a maximum output current of 57 A. The battery weighs 280 g and boasts a power density of 159 Wh/kg.

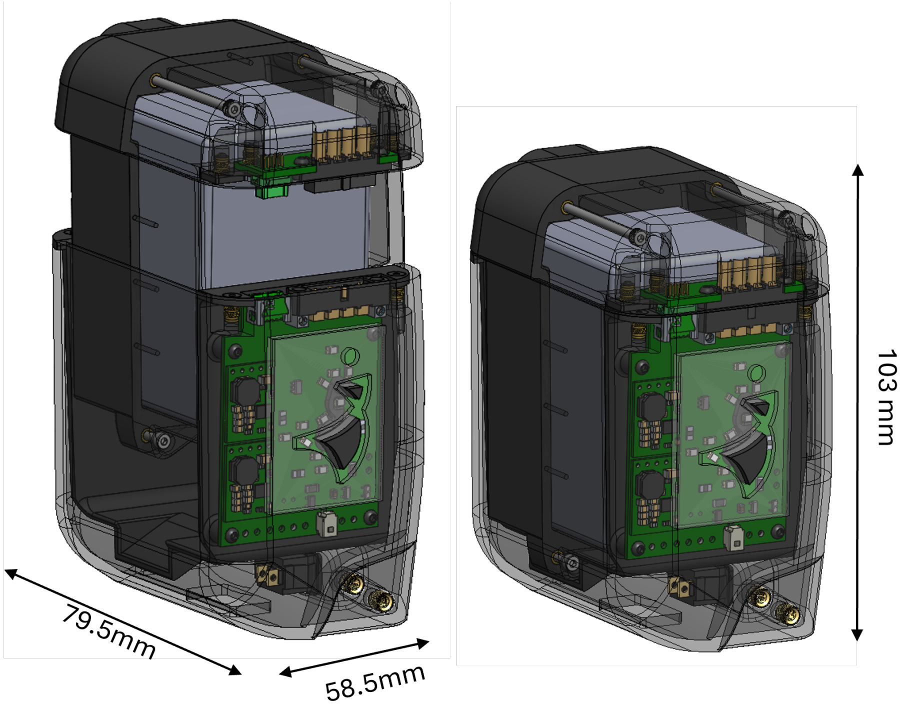

Figure 3-14: Three-dimensional CAD model of the custom battery module. The compact design (103 x 79.5 x 58.5 mm) integrates a 6-cell LiPo battery and control electronics, optimizing space efficiency for prosthetic application.

The transparent view in Figure 3-14 reveals the internal components, including the gray-colored battery and a custom power management printed circuit board (PCB). This PCB regulates the battery input to provide 24V, 12V, and 5V outputs, powering various electronics within the system. The board incorporates surge and electrostatic discharge (ESD) protection features, enhancing system reliability. Additionally, it continuously monitors the battery's total voltage; when the voltage drops below 21

V, the board automatically deactivates the LED indicators as a low-battery safeguard. Figure 3-15 provides a close-up view of the power management PCB.

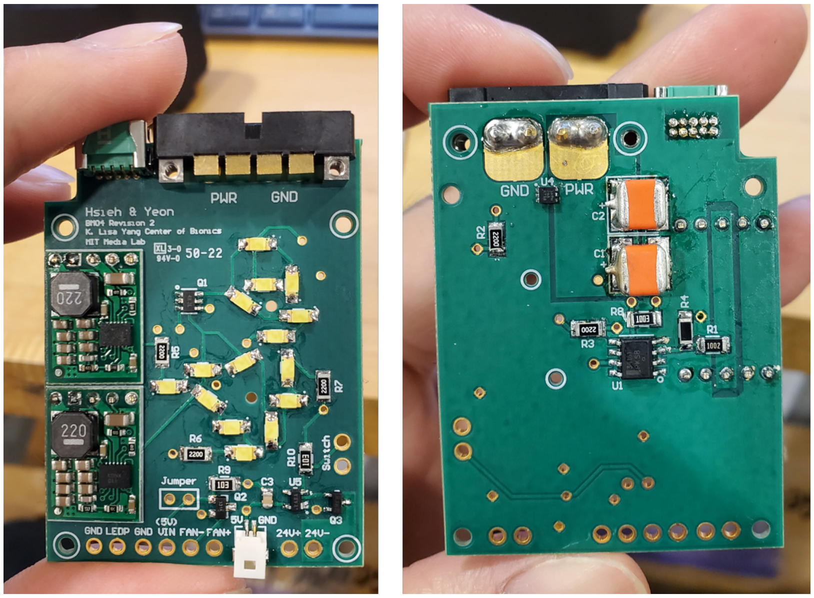

Figure 3-15: Front (left) and back (right) views of the custom power management PCB. The board features integrated voltage regulation, surge protection, and battery monitoring capabilities.

On the opposite side, the module also features LED indicators and a USB Type-C connector. This port interfaces with the USB port on the single-board computer situated at the front of the ankle (refer to Figure 3-1 for the computer's location). In our current system configuration, this connection facilitates the integration of an EMG acquisition and processing board. Figure 3-16 provides visual representations of both the standalone module and a subject wearing the complete system.

3.6 Embedded System Architecture

The powered ankle prosthesis incorporates a sophisticated embedded system architecture that integrates power management, control, computation, and actuation subsystems. Figure 3-17 presents a detailed block diagram of this architecture, illustrating the interconnections between various components and subsystems.

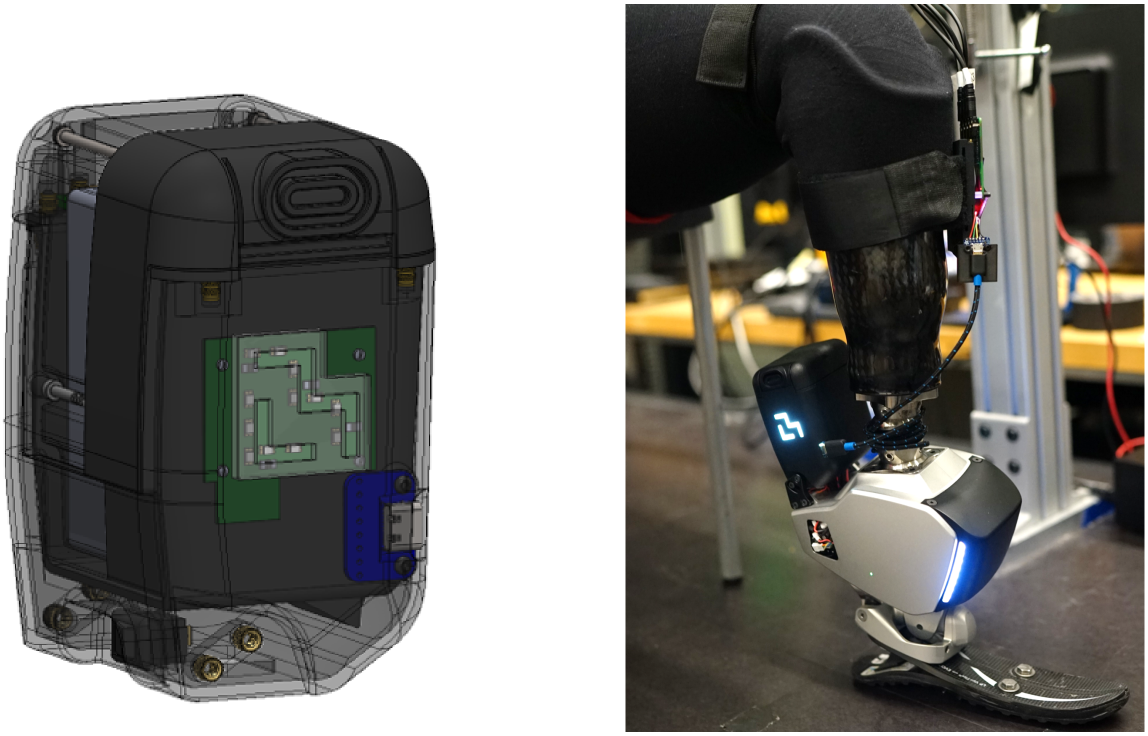

(a) (b)

Figure 3-16: Components of the battery module on the opposite side. (a) 3D CAD model of the electronic module, showing the internal circuitry and housing design. (b) The complete prosthetic system worn by a subject, highlighting the integration of the module with the prosthetic limb.

3.6.1 Power Distribution and Management

The power distribution and management system, detailed in Section 3.5, forms the foundation of the prosthesis' electrical infrastructure. It manages the six-cell Li-Po battery, providing regulated power to all subsystems while incorporating essential safety and monitoring features.

3.6.2 Control and Computation

The control board forms the computational core of the prosthesis, featuring:

- **Computer on Module**: This module features multiple ARM Cortex processors (four A53 cores and one M7 core), a Neural Processing Unit (NPU), and support for Wi-Fi 5 and Bluetooth 5.3, offering significant computational

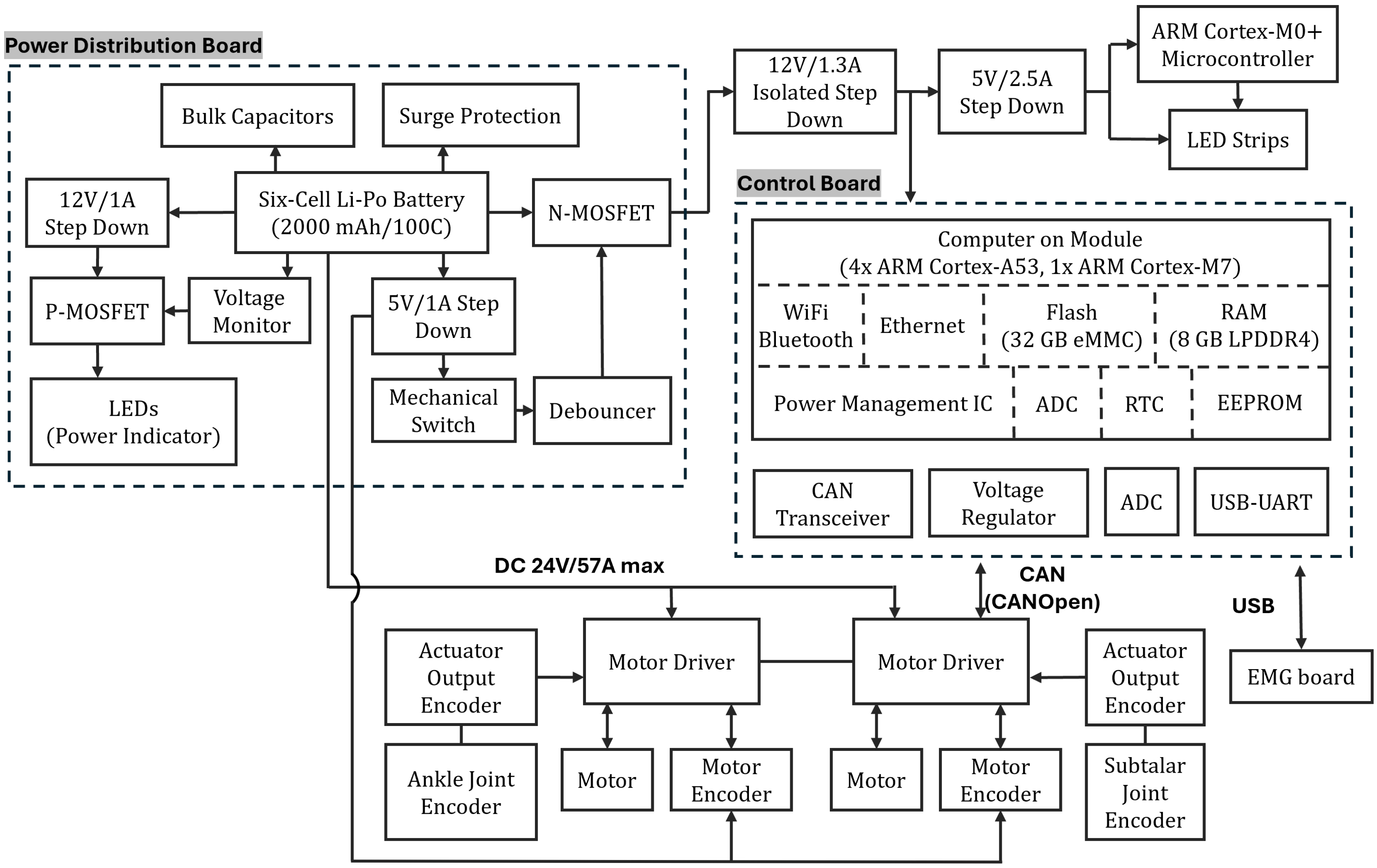

Figure 3-17: System architecture diagram of the powered ankle prosthesis, illustrating the interconnections between various components including the power distribution board, control board, computer module, motor drivers, and sensors.

capabilities (Verdin iMX8M Plus, Toradex Inc, Lucerne, Switzerland).

- **Memory Resources**: 32 GB eMMC flash storage and 8 GB LPDDR4 RAM support complex computations and data storage.
- **Connectivity**: Integrated WiFi, Bluetooth, and Ethernet capabilities enable communication and potential remote monitoring.
- **CAN (Controller Area Network)**: Utilizing the CANOpen protocol for robust inter-component communication.
- **USB**: Enables connection to external devices, such as the EMG board for myoelectric control.
- **ADC and USB-UART**: Provide additional options for sensor integration and communication.
- **Auxiliary Components**: An RTC (Real-Time Clock), EEPROM, and ADC (Analog-to-Digital Converter) support various timing, storage, and sensing functions.

Figure 3-18 depicts the control board architecture. Daniel Levine developed the low-level stack, which forms the foundation of the control system. His work encompasses a wide range of fundamental functionalities, including CAN communications, USB interfaces, analog-to-digital conversion (ADC), interrupt handling, memory management, etc. This comprehensive low-level framework provides a robust and efficient base upon which the high-level control algorithms can be implemented. Hyungeun Song and Christopher Shallal implemented the high-level control algorithms for the prosthesis.

The central processing unit (CPU) and random access memory (RAM) of the computer module generate significant heat during operation, necessitating an effective cooling solution. In our design, we implemented a comprehensive thermal management system. A thermal pad was applied to both the RAM and CPU to facilitate heat transfer. This pad connects to a heatsink, which efficiently conducts the heat

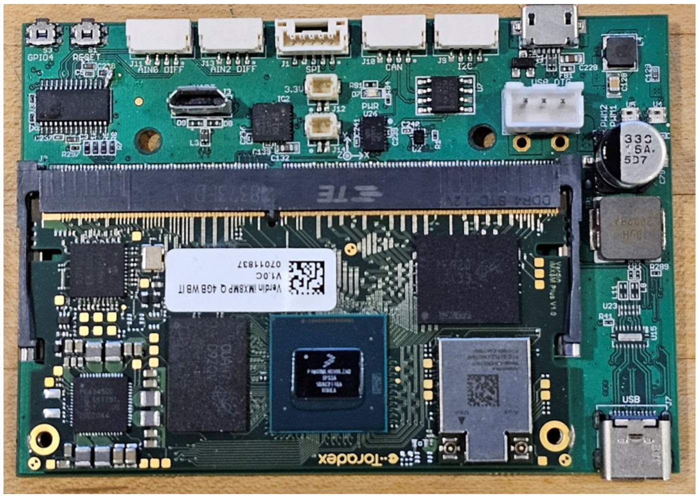

Figure 3-18: Custom control board featuring a Toradex System-on-Module (SoM) with various communication interfaces including CAN, I^2C, and USB. The board integrates power management circuitry and additional peripheral connectors for sensor integration and system control.

to the front cover of the ankle device. Both the front cover and the heatsink were fabricated from 6061 aluminum, chosen for its excellent thermal conductivity and mechanical properties. This design approach effectively transforms the entire front cover into an extended heatsink for the module, maximizing the surface area available for heat dissipation. Figure 3-19 illustrates this thermal management design, showcasing the integration of the computer module, thermal pad, heatsink, and the aluminum front cover.

3.6.3 Motor Control and Sensing

The system incorporates advanced motor control for precise actuation:

- **Dual Motor Drivers**: Each capable of handling up to 80V and 60A (field-oriented control), these drivers control the ankle and subtalar joint motors (Everest S XCR, Ingenia, Barcelona, Spain).
- **Motor Encoder Feedback**: Each motor is equipped with an 18-bit magnetic encoder (AksIM-2, RLS d.o.o., Ljubljana, Slovenia) for accurate position and velocity feedback.

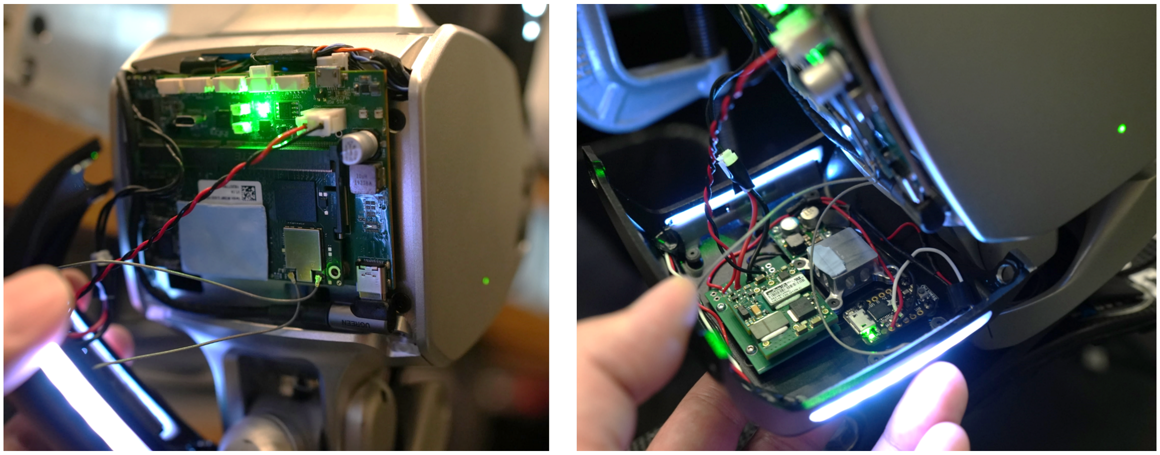

Figure 3-19: Internal views of the ankle. Left: The main control board featuring the Toradex System-on-Module, integrated within the aluminum housing that serves as a heatsink. Right: Close-up view of the auxiliary electronics and LED indicators, demonstrating the compact integration of components within the device.

- **Actuator Output Encoder**: At the output of each actuator is a 20-bit optical encoder (Aura, Celera Motion, Bedford, MA, USA) for precise actuator position measurement.
- **Joint Angle Encoders**: Dedicated 18-bit optical encoders (Aura, Celera Motion, Bedford, MA, USA) for the ankle and subtalar joints provide direct joint angle measurements.

3.6.4 Auxiliary Systems

- **LED Strips**: Controlled by an ARM Cortex-M0+ microcontroller, these may serve as status indicators or for other visual feedback purposes.
- **Isolated Power Supplies**: 12V/1.3A and 5V/2.5A isolated step-down converters ensure clean power for the control board.

3.6.5 EMG Acquisition System

The prosthesis incorporates a custom-designed embedded electromyography (EMG) acquisition system, crucial for capturing and processing surface EMG (sEMG) signals within the prosthetic socket. Developed by Yeon et al. [52], this system addresses the unique challenges of acquiring sEMG signals in lower extremity prostheses, particularly during dynamic loading conditions.

The hardware features a DC-coupled differential pre-amplifier (AD8422, Analog Devices) with high input impedance ($Z_{in} = 200G\Omega||2pF$) and low gain (G = 10), mitigating high skin-electrode impedance and large dynamic DC voltage swings associated with dry electrodes. A 24-bit high-resolution analog-to-digital converter (ADS1299, Texas Instruments) ensures precise signal digitization. For wireless data logging, the system employs a WiFi module (RN42, Microchip Technology).

This advanced system can simultaneously measure up to 16 channels at a sampling frequency of 2 kHz, providing high temporal resolution. Real-time signal processing includes band-pass filtering (80-340 Hz), rectification, and cumulative histogram filtering to mitigate motion artifacts during ambulation.

The EMG acquisition system is designed to interface seamlessly with the Sub-Liner Interface for Prosthetics (SLIP) electrodes, allowing effective sEMG signal capture within the confined space of a prosthetic socket without compromising user comfort or prosthesis functionality. This integration enables robust sEMG measurements during various activities, including stationary voluntary movements and dynamic walking tasks, opening up new possibilities for intuitive control of powered lower extremity prostheses and advancing neuroprosthetic research.

In summary, this integrated architecture demonstrates the complexity and sophistication of the powered ankle prosthesis. By combining custom power management, robust computational resources, precise motor control, multiple sensing and communication interfaces, and a custom EMG acquisition system, the prosthesis delivers responsive, adaptive, and intelligent functionality. The EMG system, featuring high-resolution signal processing and seamless integration with SLIP electrodes, enables accurate sEMG measurements during various activities, enhancing the potential for intuitive control. This comprehensive integration of power, computation, sensing, and bio-signal acquisition showcases the prosthesis's capability to provide natural and efficient motion. The modular design allows for future upgrades or modifications to individual components, including potential enhancements to the EMG system, without necessitating a complete system overhaul. This flexibility ensures the prosthesis can evolve with technological advancements and adapt to user-specific needs. Figure 3-20 illustrates the system.

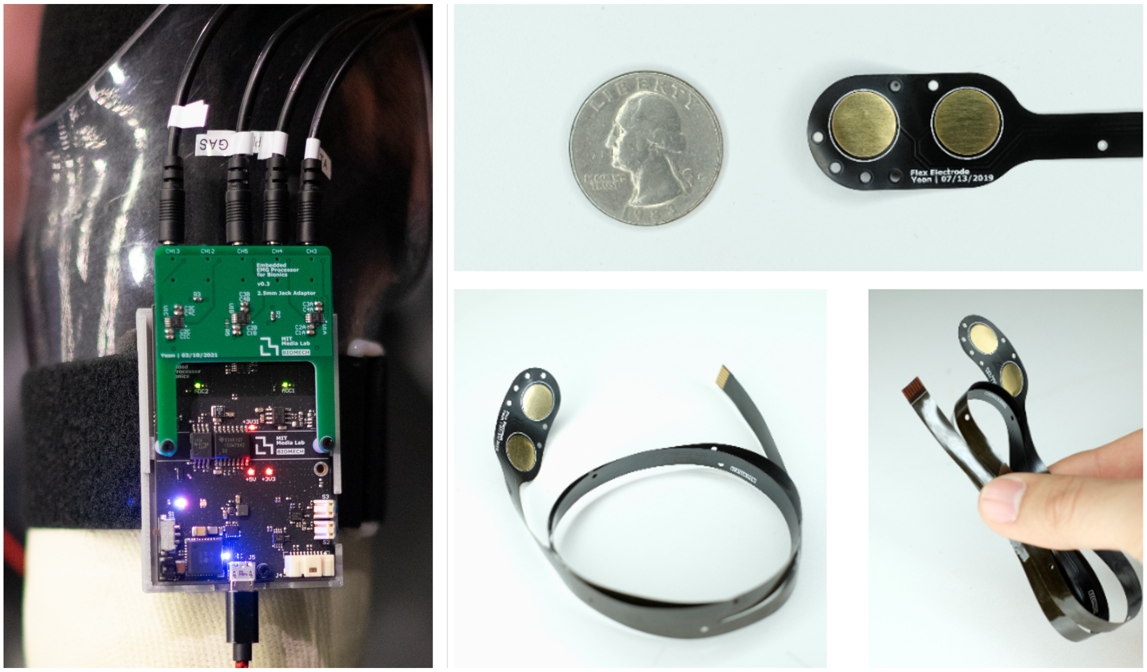

Figure 3-20: Components of the EMG acquisition system. Left: The custom-designed embedded EMG acquisition board with multiple channels. Right: The flexible SLIP (Sub-Liner Interface for Prosthetics) electrode is shown in size comparison with a US quarter coin, in a full-length view displaying its electrode contacts and cable, and demonstrating its flexibility, which allows it to conform to the contours of the residual limb within a prosthetic socket.[52]

3.7 Enclosure Design

In collaboration with industrial designers Chia-Wen Hedy Lin and Tung-Ju Oliver Hsieh, we developed two potential enclosure designs for the project, as illustrated in Figure 3-21. The first design focused on highlighting the innovative rotary actuator, aiming to showcase its mechanical novelty. The second design, in contrast, was inspired by the human form, featuring more curves and surface variations to create a more organic appearance. After careful consideration, we chose to pursue the second design. We further refined it by drawing inspiration from automotive design, particularly in the treatment of curves, which ultimately led to our final design, which is highlighted in red in Figure 3-21b. Figure 3-22 presents front and side views of the physical ankle prototype.

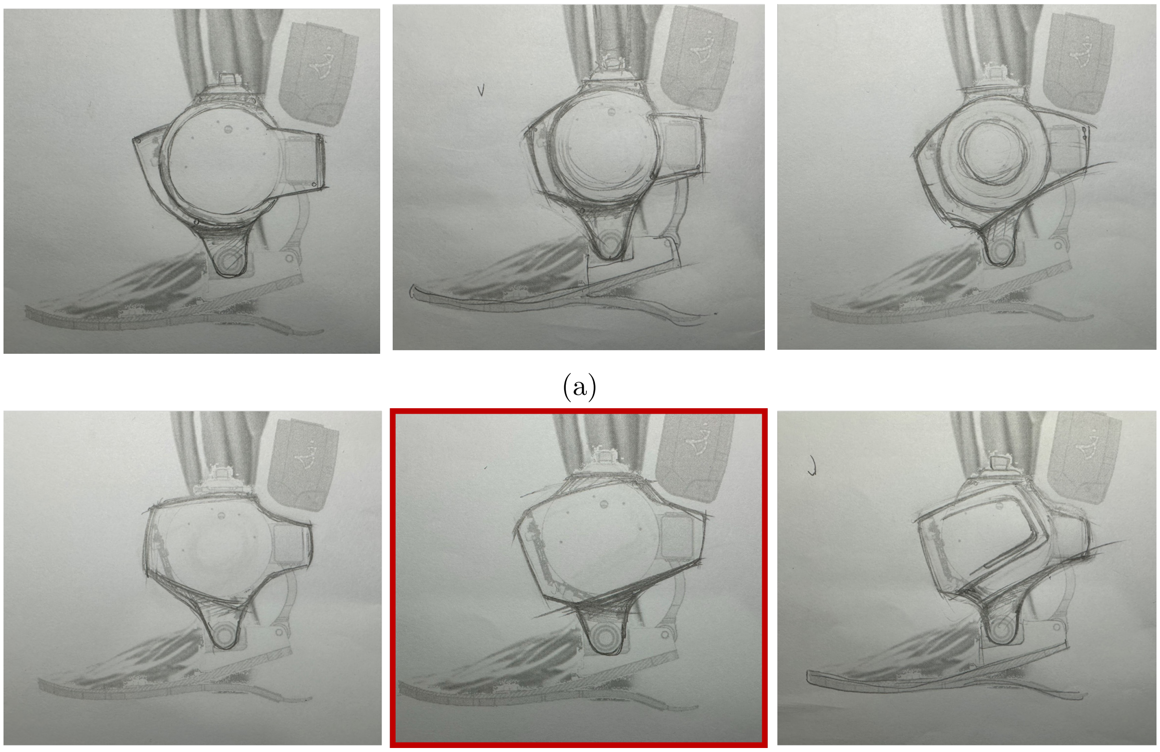

(a)

(b)

Figure 3-21: Comparison of the two enclosure designs. (a) The first design emphasizes the novel rotary actuator, while (b) the second design, inspired by human body forms and car design curves, was chosen as the final design.

One of the critical aspects of the enclosure design is its role in effective wire management. In lower limb prosthesis prototypes, wires are frequently the primary point of failure. Malfunctions are often attributed to broken or loose wires, a consequence of the prostheses' distal location on the body, their swinging motion, and exposure to impact loads. These factors can easily compromise wire integrity if adequate protection is not implemented.

Although our focus is on research prototypes rather than commercial products, it remains crucial to adhere to best practices in design. This approach enhances both safety and reliability. Consequently, we invested considerable effort in developing an enclosure that fully internalizes all wiring. As illustrated in Figure 3-22, the design

Figure 3-22: Front (left) and side (right) views of the developed prosthetic ankle device. The design incorporates a sleek, biomimetic form factor with integrated electronic components, showcasing the fusion of advanced robotics and ergonomic design principles in modern prosthetics.

successfully eliminates any exposed wires, representing a notable improvement in robustness and functionality.

This design strategy not only mitigates the risk of wire-related failures but also contributes to the overall durability and performance of the device. By addressing this common vulnerability, we have potentially improved the device's longevity and reduced the frequency of maintenance interventions, which are critical factors in both research and practical applications.

3.8 Conclusion

This chapter has presented a comprehensive overview of the design and development of an innovative 2DoF powered ankle-foot prosthesis. Our approach addressed key challenges in the field of powered prosthetics, aiming to achieve biological fidelity while maintaining a compact form factor.

The prosthesis design incorporates several novel features:

1. **Custom integrated actuators:** We developed compact actuators with a two-stage planetary gear drive, optimized for torque and speed requirements across various walking conditions.
2. **Differential drive system:** The use of two actuators in a differential configuration enables control in both sagittal and frontal planes, mimicking natural ankle movements.
3. **Series elastic elements:** We designed and validated the Bézier curve-based springs, allowing for adjustable stiffness and improved force sensing.
4. **Advanced control architecture:** The embedded system integrates high-performance computing, precise motor control, and multiple sensing modalities, including a custom EMG acquisition system.
5. **Efficient power management:** A custom battery module and power distribution system ensure optimal energy utilization and system reliability.
6. **Ergonomic enclosure design:** The biomimetically inspired housing not only enhances aesthetics but also addresses critical issues like wire management and thermal dissipation.

Throughout the design process, we encountered and addressed several challenges, particularly in force sensing and backlash reduction. The implemented solutions, including preloading mechanisms and optimized tolerances, demonstrate the iterative nature of prosthetic design and the importance of rigorous testing and refinement.

The resulting prosthesis achieves specifications that closely approximate biological ankle capabilities in terms of range of motion, including 50° plantarflexion, 30° dorsiflexion, and 35° in both inversion and eversion. With a total weight of 3.4 kg including the battery, the device is heavier than a typical biological ankle-foot complex. However, this additional weight allows for powered assistance, potentially offering functional benefits that offset the increased mass. Future iterations will focus on further weight reduction while maintaining or improving the current performance capabilities.

This work lays a solid foundation for future research in powered lower-limb prosthetics. The modular design allows for future upgrades or modifications to individual components without necessitating a complete system overhaul. This flexibility ensures the prosthesis can evolve with technological advancements and adapt to user-specific needs.

In conclusion, this chapter has detailed the development of a powered ankle prosthesis that integrates state-of-the-art components such as high-performance motor drivers, embedded computers, and custom-designed mechanical elements. The design combines novel mechanical solutions, a sophisticated control architecture, and considerations for practical implementation. This prosthesis aims to contribute to the ongoing research and development efforts in restoring ankle functionality and enhancing mobility for individuals with lower-limb amputations.

Chapter 4

Prosthesis System Validation

4.1 Introduction

This chapter presents the methodology and results of our prosthesis system validation. To rigorously assess the performance of our design, we recruited an individual with unilateral transtibial amputation who had undergone Agonist-antagonist Myoneural Interface (AMI) surgery. The system was evaluated under direct neural control, with a particular focus on adaptation to terrains and perturbations.

We begin by delineating the experimental setup and elucidating the high-level control algorithm employed in our study. Subsequently, we present and analyze the data collected during various trials. Our analysis encompasses several key performance metrics, including a comparison of energy expenditure between simulated models and actual measurements, an assessment of open-loop torque tracking performance, and an examination of the prosthesis's functionality during level ground walking and obstacle navigation.

The latter tests were specifically designed to evaluate the system's capacity for inversion and eversion, crucial aspects of our two-degree-of-freedom design. Through these comprehensive evaluations, we aim to provide a thorough validation of our prosthesis system, demonstrating its efficacy in replicating natural ankle function and adaptability across diverse locomotor challenges. It is important to note that this study involves a single participant (N=1); therefore, we do not make any broad clinical claims. Instead, our focus is on system validation and data interpretation, providing insights into the performance and potential of our novel prosthetic design.

4.2 Neural Control Implementation

4.2.1 Overview

The Continuous Neural Impedance Modulation (CNIM) algorithm represents a paradigm shift in bionic limb control, enabling the user's nervous system to directly and continuously modulate the bionic ankle torque across a diverse range of motor tasks [11]. This approach diverges from traditional control frameworks that rely on predefined intrinsic control strategies, such as state machines, offering a more intuitive and adaptable control mechanism. Figure 4-1 presents a high-level diagram of the algorithm, adapted from the work of Hyungeun Song [53]. The system exemplifies a closed-loop interaction between the user's nervous system and the prosthetic device. The process starts from the user's brain transmitting motor control signals, which are captured as raw EMG signals via our custom EMG board (see Section 3.6.5). These signals undergo processing to extract the EMG envelope, which is subsequently utilized to decode the user's motor intentions.

The decoded intentions inform two key parameters: joint impedance regulation and target joint angles calculation. These parameters are input into an impedance control system that also incorporates the current joint angles and velocities. This controller generates joint torque commands for both the ankle and subtalar joints of the powered prosthetic ankle. The ankle's movement engenders perceptual experiences for the user, which are conveyed back to the brain. This sensory feedback facilitates enhanced sensorimotor adaptation, thus completing the control loop. The system integrates various components including flexible electrodes, an EMG board, and the prosthesis itself.

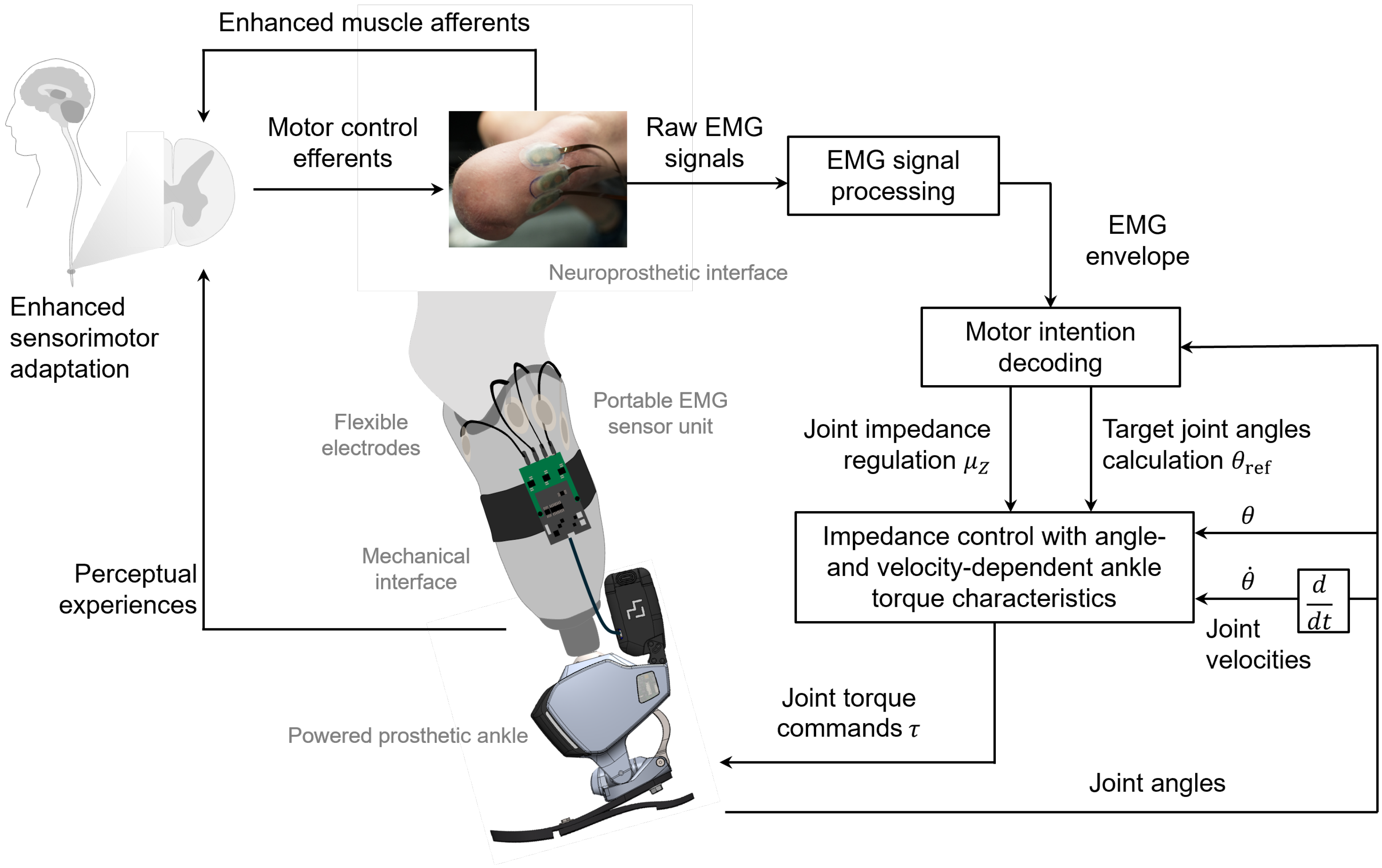

Figure 4-1: High-level schematic of the Continuous Neural Impedance Modulation (CNIM) algorithm for bionic ankle control. The diagram illustrates the closed-loop interaction between the user's nervous system, the neuroprosthetic interface, EMG signal processing, motor intention decoding, and impedance control of the powered prosthetic ankle.

4.2.2 EMG Signal Processing

We will now examine each individual component of the control system in detail. First, we focus on the EMG signal processing. While Song et al. [11] concentrated on active 1-DoF control utilizing two electrodes, our study extends to 2-DoF control, necessitating the use of four electrodes. These were strategically placed on key muscle groups:

- Tibialis Anterior (TA)
- Gastrocnemius (GAS)
- Tibialis Posterior (TP)
- Peroneus Longus (PL)

The placement of these electrodes is illustrated in Figure 4-2. In our experimental setup, we allowed the subject full control over ankle joint impedance, consistent with Song et al.'s work [11]. However, for the subtalar joint, we limited the subject's control to joint stiffness, omitting position control. This decision was primarily driven by the electrode configuration, as evident in Figure 4-2. The close proximity of the electrodes resulted in significant signal crosstalk. While it is theoretically possible to distinguish and isolate these crosstalk signals, we opted not to pursue this complex signal processing task given our focus on system validation rather than comprehensive control implementation. This strategic simplification allowed us to proceed with our primary objective of validating the overall system performance, while acknowledging the potential for future refinement in signal processing to achieve full 2-DoF control. This approach provided a balance between demonstrating the capabilities of our 2-DoF prosthesis and maintaining a feasible scope for our current study.

The EMG signal processing pipeline, as illustrated in Figure 4-3, consists of three main stages designed to extract a clean, normalized EMG envelope from the raw signals [52]. This process is crucial for obtaining reliable muscle activation information for prosthesis control.

Figure 4-2: Electrode placement for 2-DoF control of the powered ankle-foot prosthesis. Four electrodes are positioned on key muscle groups: Tibialis Anterior (TA), Gastrocnemius (GAS), Tibialis Posterior (TP), and Peroneus Longus (PL).

1. **Band-pass filtering:** The raw EMG signals first undergo band-pass filtering with a passband of 80-340 Hz. This step serves to remove low-frequency motion artifacts, eliminate high-frequency noise, and attenuate power line interference (60 Hz). The chosen frequency range focuses on the primary spectral content of surface EMG signals.

2. **Cumulative histogram filtering:** Following band-pass filtering, a cumulative histogram filtering technique is applied. This approach, developed to mitigate artifacts from dynamic ground impacts during ambulation, involves calculating a cumulative short-time histogram within a defined time window. By selecting data points that fall within the 10% to 80% range of the cumulative histogram, this method effectively reduces the influence of outliers and transient artifacts that could otherwise distort the EMG envelope.

3. **RMS and EMG normalization:** The final stage involves computing the root mean square (RMS) of the filtered signal, which provides a measure of the signal's power. This RMS value is then normalized using predetermined minimum and maximum values. Normalization is crucial for standardizing the EMG signals across different muscles and recording sessions, allowing for consistent interpretation of muscle activation levels.

The output of this processing pipeline is a clean, normalized EMG envelope that represents the intensity of muscle activation over time. This envelope serves as a robust input for the subsequent stages of the control system, enabling more accurate and reliable prosthesis control based on the user's muscle activity. This EMG processing approach, combined with the SLIP electrode technology [52], provides a comprehensive solution for acquiring and processing high-quality EMG signals within the challenging environment of a lower-limb prosthetic socket (see 3.6.5). The system's ability to handle motion artifacts and provide normalized, real-time muscle activation data is particularly valuable for the dynamic control requirements of powered ankle-foot prostheses.

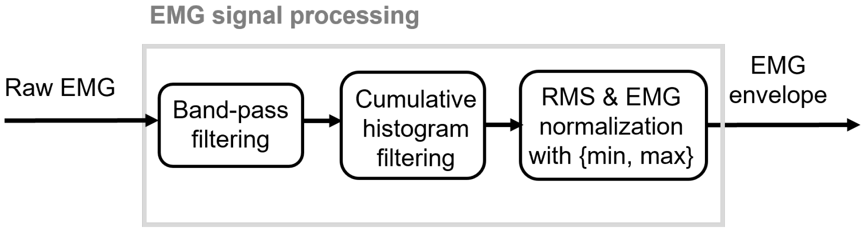

Figure 4-3: EMG signal processing pipeline. Raw EMG signals undergo band-pass filtering, cumulative histogram filtering, and RMS computation with normalization to produce a clean EMG envelope for prosthesis control.

4.2.3 Motor Intention Decoding

For motor intention decoding process, our approach builds upon the work of Song et al. [11], extending it from 1-DoF to 2-DoF control to accommodate both ankle and subtalar joint modulation. Figure 4-4 presents the block diagram.

The process begins with the conversion of normalized EMG envelopes to muscle activation signals. This is achieved using a muscle activation dynamics model [54], represented by the equation:

$$\dot{a}(t) = (u(t) - a(t))(\alpha u(t) + \beta) \tag{4.1}$$

where $a(t)$ is the muscle activation, $u(t)$ is the processed EMG signal, and α and β are shape factors that modulate the nonlinear trend of the EMG-to-activation

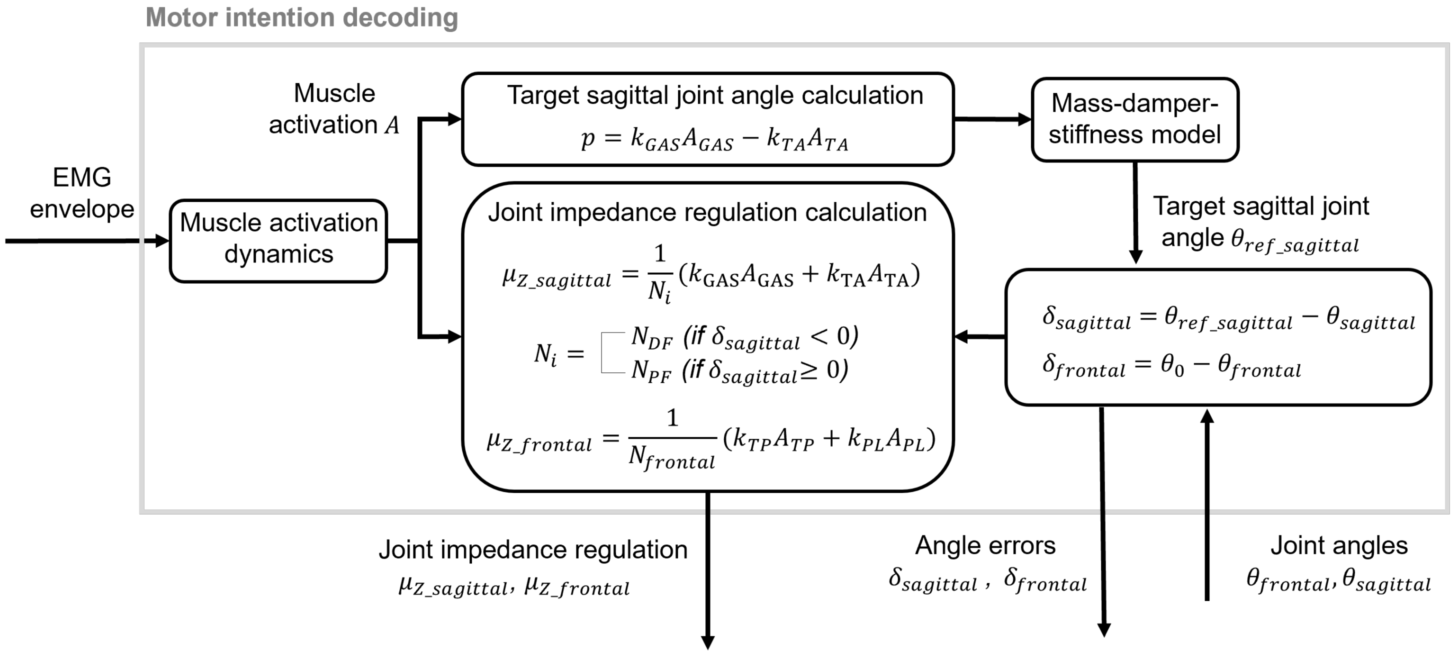

Figure 4-4: Motor intention decoding process for controlling ankle and subtalar joints using EMG signals.

relationship. For the sagittal plane (ankle dorsiflexion/plantarflexion), we calculate the target joint angle (p) as a weighted difference between the Gastrocnemius (GAS) and Tibialis Anterior (TA) activations:

$$p = k_{GAS}A_{GAS} - k_{TA}A_{TA} \tag{4.2}$$

where k_{GAS} and k_{TA} are weighting coefficients, and A_{GAS} and A_{TA} are the respective muscle activations. This target angle is then smoothed using a mass-damper-stiffness model to produce the final target sagittal joint angle ($\theta_{ref\_sagittal}$).

Joint impedance regulation is calculated separately for the sagittal and frontal planes:

$$\mu_{Z\_sagittal} = \frac{1}{N_i}(k_{GAS}A_{GAS} + k_{TA}A_{TA}) \tag{4.3}$$

$$\mu_{Z\_frontal} = \frac{1}{N_{frontal}}(k_{TP}A_{TP} + k_{PL}A_{PL}) \tag{4.4}$$

Here, N_i switches between dorsiflexion (N_{DF}) and plantarflexion (N_{PF}) normalization factors based on the sign of the sagittal plane angle error ($\delta_{sagittal}$), while $N_{frontal}$ is the normalization factor for the frontal plane.

The system also calculates angle errors for both planes:

$$\delta_{sagittal} = \theta_{ref\_sagittal} - \theta_{sagittal} \tag{4.5}$$

$$\delta_{frontal} = \theta_0 - \theta_{frontal} \tag{4.6}$$

where θ_0 represents a neutral reference angle for the subtalar joint. The motor intention decoding system ultimately outputs four key parameters: $\mu_{Z\_sagittal}$, $\mu_{Z\_frontal}$, $\delta_{sagittal}$, and $\delta_{frontal}$. These parameters are then utilized by the subsequent impedance control to modulate joint behavior, enabling adaptive and user-intended movements in both the ankle and subtalar joints.

This motor intention decoding system extends the capabilities of 1-DoF control schemes by incorporating subtalar joint control, limited to stiffness modulation in the current implementation. The system interprets muscle activation patterns and translates them into control parameters for both the ankle and subtalar joints. This approach aims to provide users with control over their ankle-foot prosthesis that more closely mimics natural ankle function. Further research and user studies would be needed to quantify the potential benefits of this extended control scheme in terms of prosthesis performance and user experience.

4.2.4 Impedance Control

The impedance control module is the final stage in our prosthetic control system, translating the decoded motor intentions into joint torque commands. This module utilizes the joint impedance regulation parameters and angle errors from the motor intention decoding stage, along with current joint states, to calculate appropriate torques for both the sagittal (ankle) and frontal (subtalar) planes. Figure 4-5 illustrates the block diagram of this impedance control module.

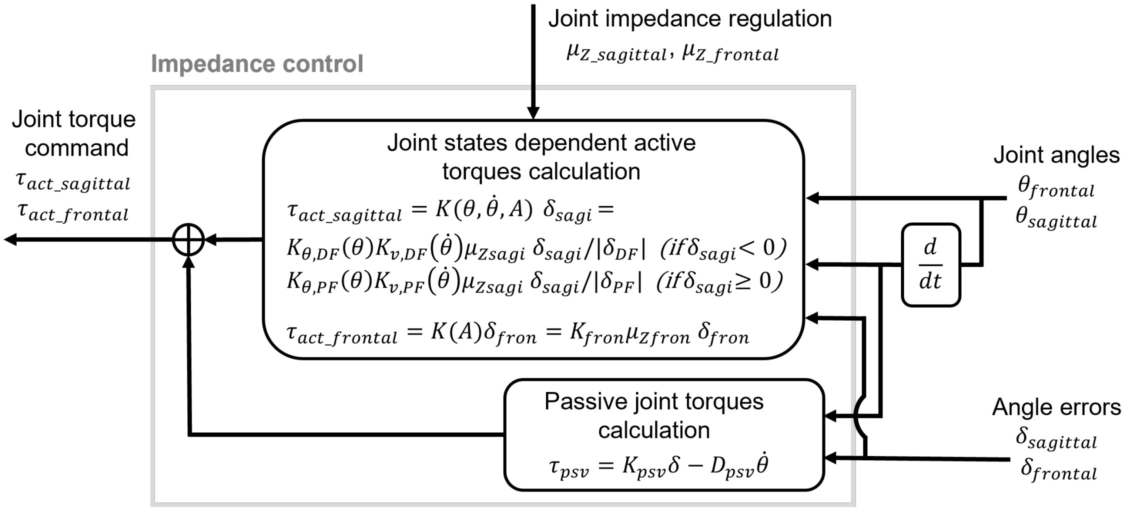

Figure 4-5: Block diagram of the impedance control system, showing the calculation of active and passive torque components for sagittal and frontal plane control of the powered ankle-foot prosthesis.

The control system computes active and passive torque components separately. The active torque calculation for the sagittal plane ($\tau_{act\_sagittal}$) is state-dependent and given by:

$$\tau_{act\_sagittal} = K(\theta, \dot{\theta}, A)\delta_{sagi} \tag{4.7}$$

where $K(\theta, \dot{\theta}, A)$ is a function of joint angle (θ), angular velocity ($\dot{\theta}$), and muscle activation (A). This function is defined piecewise:

$$K(\theta, \dot{\theta}, A) = \begin{cases} K_{\theta,DF}(\theta)K_{v,DF}(\dot{\theta})\mu_{Zsagi}\delta_{sagi}/|\delta_{DF}| & \text{if } \delta_{sagi} < 0 \\ K_{\theta,PF}(\theta)K_{v,PF}(\dot{\theta})\mu_{Zsagi}\delta_{sagi}/|\delta_{PF}| & \text{if } \delta_{sagi} \geq 0 \end{cases} \tag{4.8}$$

Here, $K_{\theta,DF}(\theta)$ and $K_{\theta,PF}(\theta)$ are angle-dependent stiffness functions for dorsiflexion and plantarflexion, respectively. Similarly, $K_{v,DF}(\dot{\theta})$ and $K_{v,PF}(\dot{\theta})$ are velocity-dependent damping functions. The terms δ_{DF} and δ_{PF} represent normalization factors for dorsiflexion and plantarflexion. For the frontal plane, the active torque ($\tau_{act\_frontal}$) is calculated as:

$$\tau_{act\_frontal} = K(A)\delta_{fron} = K_{fron}\mu_{Zfron}\delta_{fron} \tag{4.9}$$

where K_{fron} is a constant stiffness term for the frontal plane. In addition to the active torques, the system computes a passive torque component (τ_{psv}) to provide baseline stability:

$$\tau_{psv} = K_{psv}\delta - D_{psv}\dot{\theta} \tag{4.10}$$

where K_{psv} and D_{psv} are passive stiffness and damping coefficients, respectively.

The final joint torque commands ($\tau_{act\_sagittal}$ and $\tau_{act\_frontal}$) are the sum of their respective active and passive components. These torque commands are then sent to the prosthetic device's actuators for execution. This impedance control approach allows for adaptive joint behavior based on the user's decoded motor intentions and the current state of the prosthetic joints. The incorporation of both active and passive elements aims to provide a balance between user-driven control and inherent stability of the prosthetic device.

4.3 Results and Discussion

4.3.1 Experimental Protocol and Subject Information

For this study, we recruited a single subject with unilateral transtibial amputation who had undergone AMI surgery. The participant was a 47-year-old female, weighing 77.1 kg (170 lbs), with 6 years post-amputation experience. The AMI surgical procedure was performed at Brigham and Women's Hospital (BWH) in Boston, MA, under the Partners Healthcare Institutional Review Board (IRB) protocol P2014001379.

The subject provided informed consent at the Massachusetts Institute of Technology (MIT) in Cambridge, MA. All study data were collected under the approval of MIT's Committee on the Use of Humans as Experimental Subjects (protocol 1812634918). The participant received compensation at a rate of USD 20 per hour for their involvement in the study. Key inclusion criteria for the subject were proficiency in using a standard lower extremity prosthesis and an activity level or K-Level of K4, indicating the capability to ambulate with variable cadence and to traverse most environmental barriers.

This single-subject study design allows for an in-depth evaluation of our prosthesis system's performance with an individual who has undergone AMI surgery. While the results cannot be generalized to a broader population, they provide valuable insights into the potential of our design when used in conjunction with advanced neural interfacing techniques.

4.3.2 Level Ground Walking

We begin our analysis by examining the kinematic and kinetic data obtained during level ground ambulation. The subject was instructed to ambulate at a self-selected velocity. Figure 4-6 presents a comprehensive representation of the gait, comprising both chronographic imagery of a single gait cycle and corresponding joint kinematic, kinetic, and EMG data spanning multiple gait cycles.

The top portion of the figure depicts a sequence of eight images capturing salient

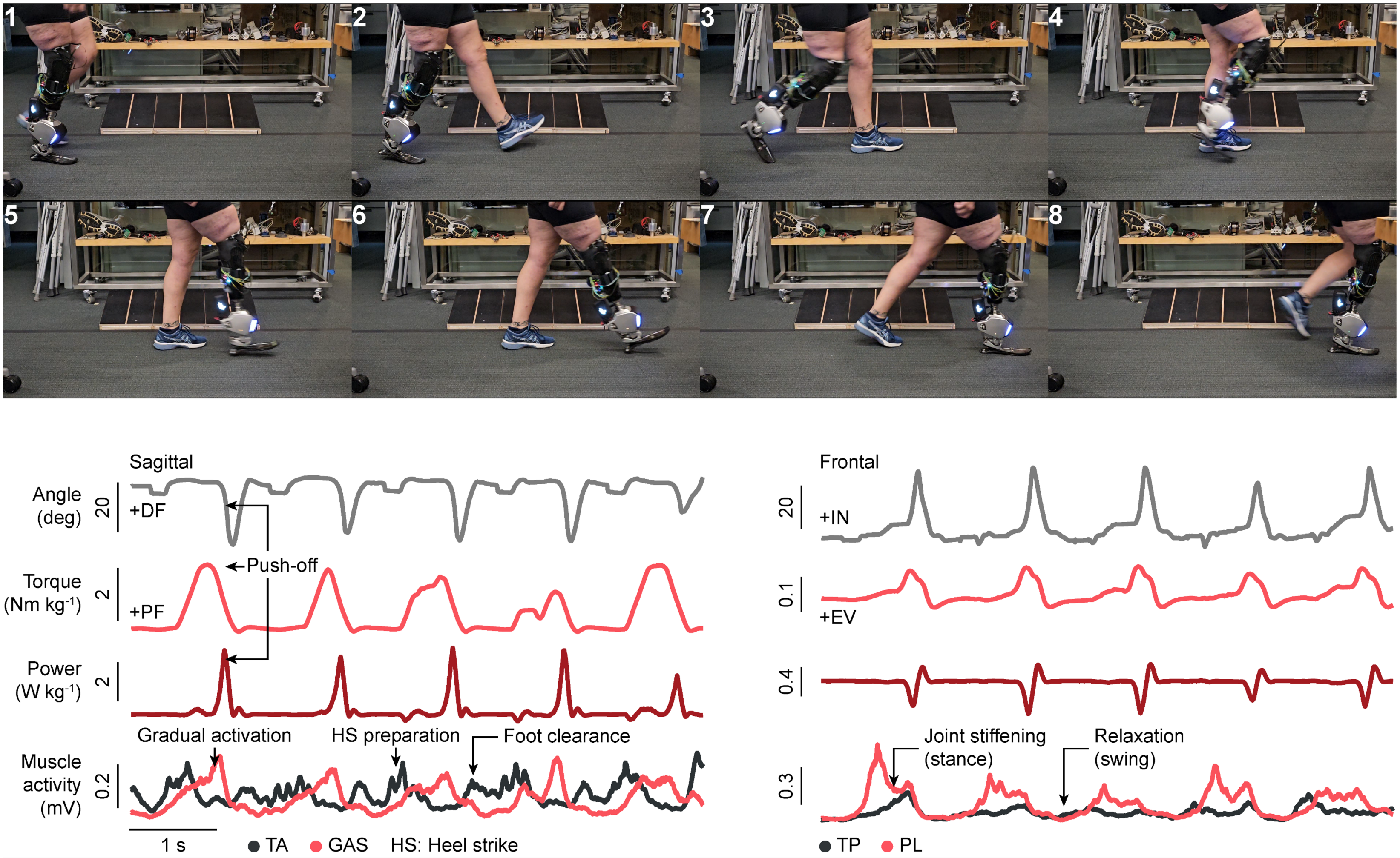

Figure 4-6: Biomechanical analysis of level ground walking with the prosthesis. Top: Chronographic sequence of one gait cycle. Bottom: Joint kinematics, kinetics, and muscle activation data for sagittal and frontal planes over four consecutive gait cycles. DF: Dorsiflexion, PF: Plantarflexion, IN: Inversion, EV: Eversion, TA: Tibialis Anterior, GAS: Gastrocnemius, TP: Tibialis Posterior, PL: Peroneus Longus, DF: Dorsiflexion, PF: Plantarflexion, IN: Inversion, EV: Eversion.

moments throughout a single gait cycle. This visual chronology serves to elucidate the prosthesis's kinematics and the subject's overall gait pattern during one stride of level ground locomotion. The bottom portion of the figure displays four sets of time-series data for both the sagittal and frontal planes, spanning approximately five complete gait cycles.

In the sagittal plane graphs, we observe the ankle's dorsiflexion and plantarflexion kinematics over multiple steps, with gait events such as push-off and heel strike clearly demarcated. The frontal plane graphs illustrate inversion and eversion movements across several strides. The majority of the data, including angle, torque, and power measurements in the sagittal plane, demonstrate close correspondence with normative values observed in individuals without lower-limb amputation[55]. However, a notable deviation is observed in the frontal plane, specifically in the eversion-inversion kinematics. As evidenced in the figure, the peak inversion angle exceeds 20 degrees, which is substantially greater than typical physiological values.

This aberrant frontal plane kinematics can be attributed to the backlash issues previously discussed in Section 3.4.3. The excessive clearance in the transmission mechanism results in a substantial "dead zone" characterized by minimal control authority. Moreover, due to the differential drive configuration of our design, this frontal plane backlash is effectively doubled, further exacerbating the deviation from normative ankle kinematics in the frontal plane.

The EMG data provide insights into the temporal activation patterns of specific muscle groups throughout the gait cycles. In the sagittal plane, we observe the activity of the Tibialis Anterior (TA) and Gastrocnemius (GAS) muscles. The EMG traces reveal several key events:

1. **Gradual activation:** At the beginning of the stance phase, we observe a gradual increase in muscle activity, particularly in the GAS, as the ankle prepares for push-off.

2. **Push-off:** A pronounced spike in GAS activity coincides with the push-off phase, indicating active plantarflexion to propel the body forward.

3. **Heel strike (HS) preparation:** Just prior to heel strike, there is increased activity in the TA, suggesting preparatory action for landing.
4. **Foot clearance:** During the swing phase, we note elevated TA activity, which assists in dorsiflexion to ensure adequate foot clearance.

In the frontal plane, the activation patterns of the Tibialis Posterior (TP) and Peroneus Longus (PL) muscles are presented. Two key events are highlighted:

1. **Joint stiffening (stance):** During the stance phase, we observe increased activity in both TP and PL, indicating co-contraction to stabilize the ankle joint.
2. **Relaxation (swing):** As the limb enters the swing phase, there is a noticeable decrease in both TP and PL activity, allowing for a more compliant ankle during limb advancement.

These EMG patterns demonstrate the prosthesis's ability to respond to the user's neuromuscular inputs, enabling dynamic control of the ankle throughout the gait cycle. The correlation between muscle activations and specific gait events suggests that the user can effectively modulate the prosthesis's behavior to meet the changing demands of level ground walking.

Following our analysis of the EMG data, we now turn our attention to the sagittal plane kinetics. Figure 4-7 presents a comparison of peak power and net work between our subject (Subject A) using the prosthesis and normative data from individuals with intact limbs [55].

The peak power output of our prosthesis, averaging approximately $2.7Wkg^{-}1$, approaches the $3Wkg^{-}1$ observed in intact ankles. This demonstrates that our actuator design and control system can generate power outputs comparable to biological ankles during level ground walking. More notably, the net work performed by our prosthesis (mean of $0.26Jkg^{-}1$) closely matches that of intact ankles. This parity in net work suggests that our prosthesis effectively mimics the energy output of a biological ankle over a complete gait cycle, validating the efficacy of our overall mechatronic design and control strategy.

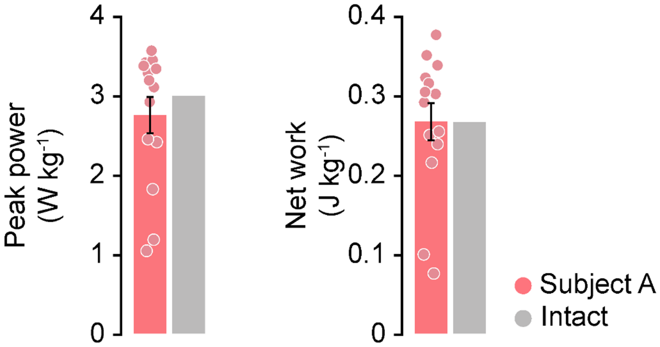

Figure 4-7: Comparison of sagittal plane kinetics between Subject A using the powered ankle-foot prosthesis and normative data from individuals with intact limbs. Left: Peak power output in watts per kilogram of body mass (W kg^{-1}). Right: Net work in joules per kilogram of body mass (J kg^{-1}). Pink bars and dots represent data from Subject A, with individual step data points shown. Gray bars represent mean values from intact limbs.

4.3.3 Model Predictions vs. Experimental Data

To validate our mechatronic design and assess its performance, we compared our experimental results with predictions from a data-driven simulation model. This model, developed using the custom dynamometer described in Chapter 2, allows us to simulate the prosthesis behavior under various conditions. It is important to note that our experiments were conducted using open-loop torque control. Consequently, the torque values were derived from motor current measurements, rather than from direct torque sensing. Figure 4-8 presents the Simulink model used for our simulations, which emulates the open-loop control strategy employed in our experimental setup. The model incorporates several key components of our prosthetic system:

1. **Mapped Motor Block:** This block implements a mapped motor and drive electronics operating in torque-control mode. It incorporates the motor efficiency map obtained from our dynamometer tests, allowing for accurate representation of motor behavior under various operating conditions.

2. **Gearbox Model:** The gearbox is modeled with assigned inertias for each gear, derived from our 3D CAD designs.

To evaluate the model's predictive capabilities, we input target torque and speed

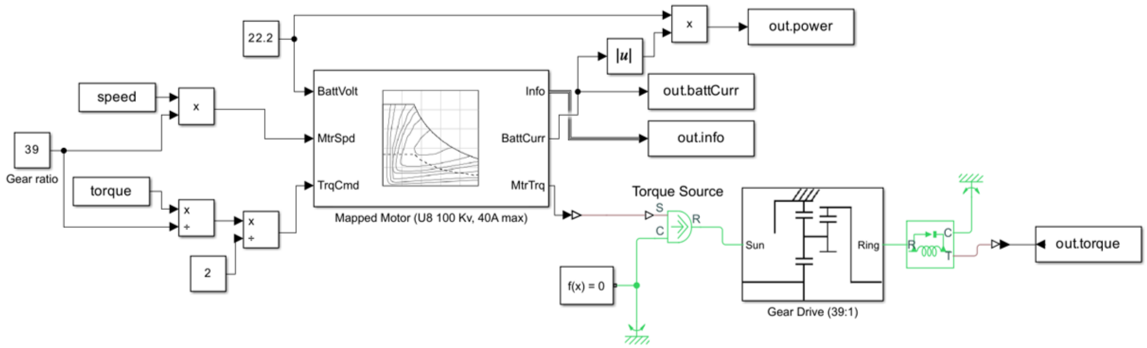

Figure 4-8: Simulink model of the powered ankle-foot prosthesis, incorporating motor efficiency maps and gearbox dynamics

profiles corresponding to level ground walking. The simulation then predicts the system's response, including torque output and energy consumption. Comparing the simulation results with our experimental data reveals:

1. **Torque Tracking:** The model-predicted torque closely aligns with the measured torque from our subject trials. We observed a root mean square error (RMSE) of 5 Nm between predicted and actual torque outputs, indicating good agreement.

2. **Energy Consumption:** Our model estimated an average energy consumption of 22.8 J per gait cycle, which is within 10% of the measured energy consumption from our experimental trials.

3. **Peak Power:** The simulated peak power output of 2.98 W kg^{-1} closely matches our experimental findings of 2.7 W kg^{-1}, further validating the model's accuracy.

These comparisons demonstrate the effectiveness of our data-driven modeling approach in predicting the performance of our powered ankle-foot prosthesis. The close alignment between simulated and experimental results not only validates our mechatronic design but also provides confidence in using this model for future design iterations and optimizations. However, it's important to note that while the model shows good agreement with our single-subject data, further validation with a larger cohort would be necessary to establish its generalizability across different users and walking conditions.

4.3.4 Adaptation to Uneven Terrain

To evaluate the prosthesis's performance in adapting to uneven terrain, we conducted trials involving a 15-degree inclined surface. These tests assessed the device's capability for inversion and eversion, crucial for maintaining balance on irregular surfaces. The subject walked at a self-selected speed, navigating the incline in two conditions: stepping with the inner edge (inversion) and outer edge (eversion) of the prosthetic foot.

Figure 4-9 illustrates the inversion condition. The data shows three consecutive steps: before, onto, and after the incline. Key observations include:

- Increased inversion angle during incline contact, demonstrating terrain adaptation
- Increased eversion torque for ankle stabilization on the incline
- Increased PL (Peroneus Longus) activation for ankle stabilization on the incline, noting that PL is an evertor muscle

Notably, the inversion angle when stepping on the obstacle reached a plateau at approximately 35 degrees, indicating that the ankle joint had reached its maximum range of motion and was limited by the mechanical hard stop. This occurred despite the subject stepping on only a 15-degree incline, suggesting that the actual required inversion angle could potentially exceed 35 degrees if the prosthesis had a greater range of motion.

The degree of inversion is highly dependent on the subject's stepping strategy and body positioning relative to the obstacle. In this trial, as evident from the chronograph, the subject's body was positioned directly above the obstacle when stepping. This body alignment necessitated a greater inversion angle to maintain balance. Had the body been positioned further from the block, a smaller inversion angle would likely have been observed.

Figure 4-10 presents the eversion condition. Notable features include:

- Significant increase in eversion angle during incline contact

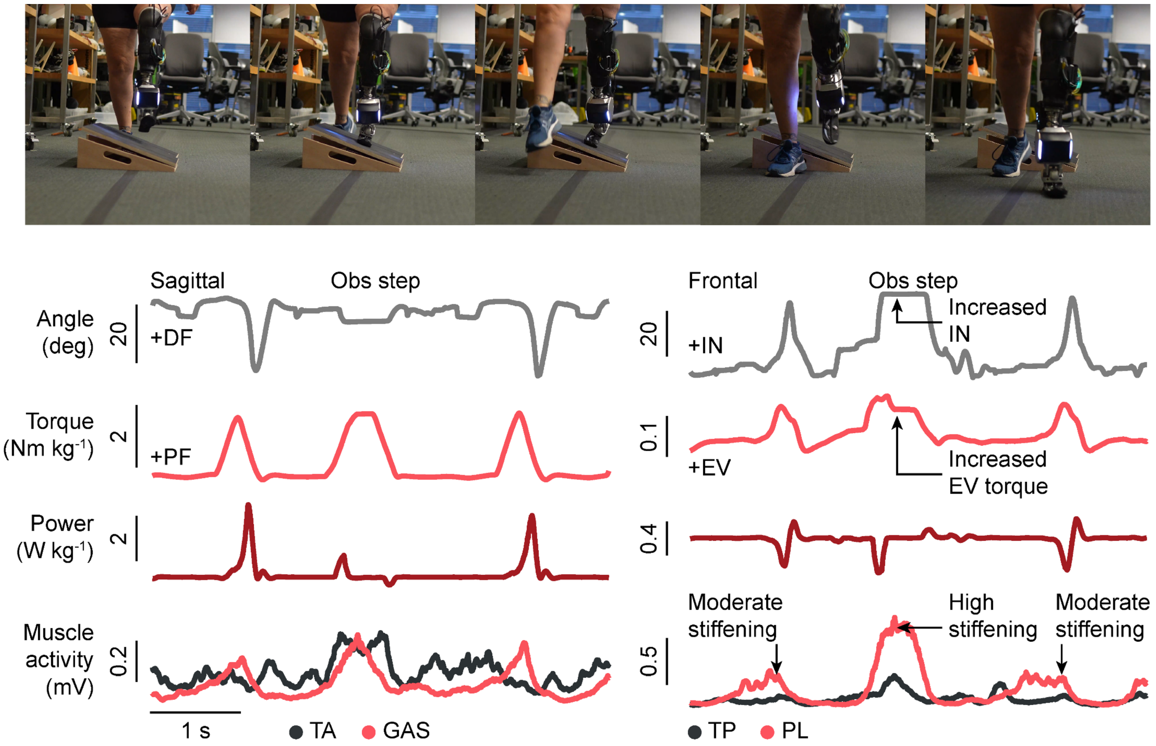

Figure 4-9: Biomechanical analysis of inclined surface navigation with inversion. Top: Chronographic sequence of the prosthetic foot stepping onto an inclined surface. Bottom: Joint kinematics, kinetics, and muscle activation data for sagittal and frontal planes over three consecutive steps.

- Increased inversion torque for foot stabilization on the incline
- Increased activation of Tibialis Posterior (TP) and Peroneus Longus (PL) muscles, corresponding to eversion angle and torque changes
- Similar sagittal plane adaptations as in the inversion condition

In both conditions, we observe:

- Return to baseline kinematics and kinetics after clearing the incline
- Coordinated muscle activity patterns suggesting effective neuromuscular control in adapting to the incline

To further understand the neuromuscular control strategies employed during obstacle navigation, we conducted a detailed analysis of the EMG data. Figure 4-11

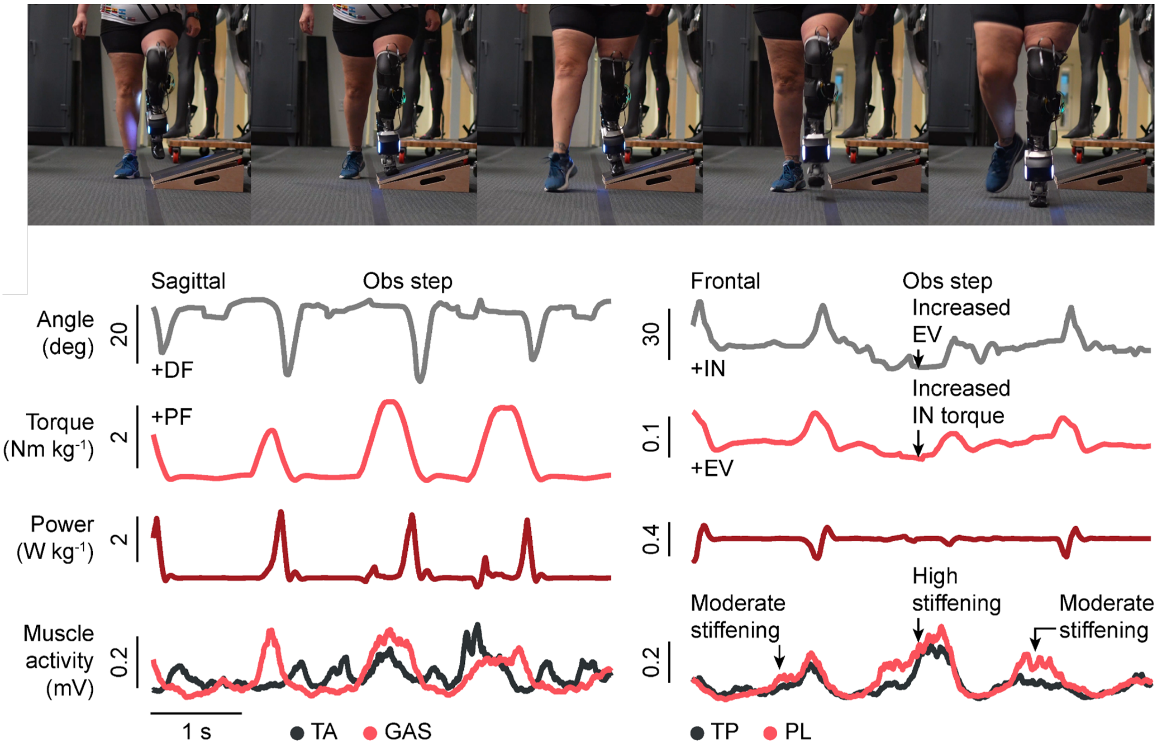

Figure 4-10: Biomechanical analysis of inclined surface navigation with eversion. Top: Chronographic sequence of the prosthetic foot stepping onto an inclined surface. Bottom: Joint kinematics, kinetics, and muscle activation data for sagittal and frontal planes over three consecutive steps.

presents two key analyses: TP and PL coactivation levels and principal component analysis (PCA) of EMG signals.

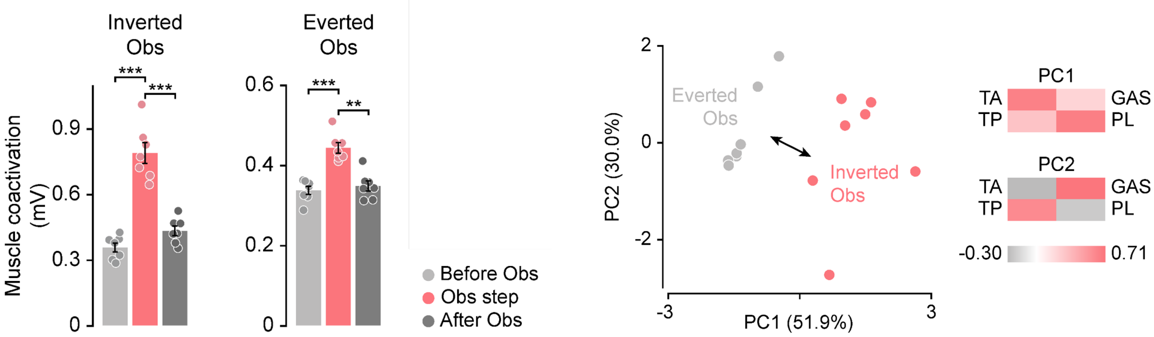

(a) (b)

Figure 4-11: EMG analysis of (a) TP and PL coactivation levels revealed significant differences, denoted by $**(p < 0.01)$ and $***(p < 0.001)$, and (b) Principal Component Analysis of EMG signals.

Figure 4-11a illustrates the coactivation levels of the TP and PL muscles before, during, and after obstacle negotiation for both inverted and everted conditions. The data reveal a significant increase in muscle coactivation when the subject steps onto the obstacle, particularly in the inverted condition. This heightened coactivation suggests a neuromuscular strategy to increase joint stiffness and stability during the challenging phase of obstacle navigation. Notably, the coactivation levels return to near-baseline values after clearing the obstacle, indicating a dynamic modulation of joint control in response to terrain changes.

The Principal Component Analysis (PCA) presented in Figure 4-11b offers insights into the dimensionality and variability of muscle activation patterns. The scatter plot clearly distinguishes between the ”Everted Obs” and ”Inverted Obs” conditions, suggesting distinct neuromuscular control strategies for each scenario. The first principal component (PC1) accounts for 51.9% of the total variance, while PC2 explains an additional 30.0%, collectively capturing over 80% of the data’s variability.

The accompanying heatmaps provide a visual representation of how each muscle contributes to the principal components. In PC1, we observe strong positive loadings for all muscles, with slightly higher contributions from the GAS and PL. This suggests that PC1 might represent overall muscle activation intensity. PC2 shows a more complex pattern, with positive loadings for TA and GAS, but negative loadings for TP and PL. This antagonistic pattern in PC2 could represent the balance between dorsiflexion/plantarflexion and inversion/eversion control.

These findings provide evidence that the subject employed distinct, coordinated muscle activation strategies for navigating inverted versus everted obstacles. The clear separation in the PCA plot and the structured patterns in muscle coactivation levels indicate that these strategies were consistently applied across trials, rather than being random muscle firings. This suggests that the prosthesis user was able to leverage the device’s capabilities to implement task-specific neuromuscular control patterns, adapting to different obstacle orientations in a controlled and repeatable manner. This analysis not only validates the effectiveness of the prosthesis in enabling nuanced control but also highlights the potential to further exploit these natural neuromuscular control strategies for improved functionality and user experience.

4.4 Conclusion

This chapter has presented a detailed evaluation of our powered ankle-foot prosthesis, demonstrating its capacity to adapt to various walking conditions, including level ground and uneven terrain. The prosthesis exhibited the ability to modulate its behavior in both sagittal and frontal planes, as evidenced by the observed changes in joint angles, torques, and muscle activation patterns across different walking scenarios. Key findings include:

- The prosthesis's performance in level ground walking closely matched normative data from individuals without amputation, particularly in sagittal plane kinematics and kinetics.

- During inclined surface navigation, the device demonstrated significant adaptability, with increased inversion/eversion angles and torques to maintain stability.

- EMG analysis revealed distinct, coordinated muscle activation strategies for navigating inverted versus everted obstacles, suggesting effective user control and adaptation.

- The comparison between experimental data and our simulation model showed good agreement, validating our mechatronic design and modeling approach.

These results collectively indicate that the user can effectively control the prosthesis to maintain stability across various terrains and foot positions, a crucial capability for navigating real-world environments. However, we acknowledge the limitations of this single-case study. While the results are encouraging, they represent the performance of one individual under specific controlled conditions. To comprehensively evaluate the robustness and versatility of our prosthesis design, future research should:

- Conduct more extensive trials involving a diverse group of participants with varying physical characteristics, amputation levels, and activity profiles.

- Test the prosthesis across a broader range of environmental challenges and daily living scenarios.
- Investigate long-term adaptation and learning effects in prosthesis users.
- Explore the potential for further optimizing the prosthesis's range of motion, particularly in inversion/eversion, based on the observed performance limits.

Additionally, future iterations of the design should address the identified limitations, such as the backlash issues in the frontal plane control. Enhancing the mechanical design and control algorithms based on these findings could further improve the prosthesis's performance and user experience.

In conclusion, while this study demonstrates the promise of our powered ankle-foot prosthesis in adapting to various walking conditions, it also highlights the need for continued research and development in this field. By addressing the identified areas for improvement and conducting more comprehensive studies, we can work towards prosthetic devices that more closely mimic natural ankle function and improve the mobility and quality of life for individuals with lower-limb amputations.

Chapter 5

Conclusion and Future Work

This thesis has presented a comprehensive approach to advancing the field of bionic ankle-foot prostheses, addressing three key aims: actuator characterization, prosthesis design, and system validation. The research conducted has yielded meaningful contributions to the understanding and development of more capable and naturalistic lower-limb prostheses.

5.1 Summary of Key Contributions

5.1.1 Aim 1: Dynamometer Development and Actuator Characterization

The custom-built dynamometer and subsequent comprehensive characterization of human-scale actuators have provided invaluable insights into the performance of exterior-rotor brushless motors across their full operating range. This study has:

- Developed detailed efficiency maps and loss profiles for multiple motor types, offering a robust framework for actuator selection in robotic applications.
- Revealed the potential for short-duration overpowering of motors, expanding the design space for high-performance robotic systems.
- Created a valuable resource for the robotics community, addressing the previous

lack of comprehensive performance data for these motors beyond their typical drone applications.

5.1.2 Aim 2: Bionic Ankle-Foot Prosthesis Design

The development of the novel two-degree-of-freedom powered ankle-foot prosthesis represents a notable advancement in prosthetic technology. Key features include:

- A compact differential drive system enabling control in both sagittal and frontal planes, mimicking natural ankle movements.
- Custom-designed actuators with integrated planetary gearboxes, optimized for the specific torque and speed requirements of ankle locomotion.
- An innovative series elastic element design using Bézier curves, allowing for adjustable stiffness and improved force sensing.
- Advanced embedded control architecture integrating high-performance computing, precise motor control, and multiple sensing modalities.

5.1.3 Aim 3: System Validation with AMI Subject

The validation study with an AMI subject provided crucial insights into the prosthesis's performance under direct neural control. Notable findings include:

- Demonstration of the prosthesis's ability to adapt to various walking conditions, including level ground and uneven terrain.
- Evidence of distinct, coordinated muscle activation strategies for navigating different obstacles, suggesting effective user control and adaptation.
- Close alignment between the prosthesis's performance and normative data from non-amputees, particularly in sagittal plane kinematics and kinetics.

5.2 Broader Implications

This research has broader implications for the field of powered prosthetics and rehabilitation robotics:

- The comprehensive actuator characterization methodology can be applied to optimize motor selection and design across various robotic applications.
- The two-degree-of-freedom ankle design opens new possibilities for more naturalistic and adaptable prosthetic devices, potentially improving user mobility and quality of life.
- The successful integration with AMI procedure demonstrates the potential for more intuitive and effective neural control of prosthetic devices.
- The modular design approach facilitates future iterations and improvements, accelerating the development cycle of advanced prosthetics.

5.3 Future Directions

While this research has made notable strides, several avenues for future work have been identified:

- **Extended user trials:** Conducting more extensive trials with a diverse group of participants to evaluate the prosthesis's performance across varying physical characteristics and activity levels.
- **Refinement of frontal plane control:** Addressing the identified backlash issues to improve the precision of inversion/eversion movements.
- **Advanced neural control algorithms:** Developing more sophisticated algorithms to fully leverage the potential of novel neural interfaces, potentially enabling even more intuitive and naturalistic control.
- **Miniaturization and weight reduction:** Further optimizing the design to reduce overall weight while maintaining or improving performance capabilities.

- **Integration of additional sensing modalities:** Exploring the incorporation of tactile and proprioceptive feedback to enhance user experience and control.
- **Long-term adaptation studies:** Investigating how users adapt to and learn to optimize their use of the prosthesis over extended periods.

In conclusion, this thesis has made important contributions to the field of powered lower-limb prosthetics, from fundamental actuator characterization to the development and validation of an advanced bionic ankle-foot prosthesis. The work presented here lays a solid foundation for future innovations in prosthetic technology, with the ultimate goal of restoring natural ankle functionality and improving the mobility and quality of life for individuals with lower-limb amputations. As we continue to push the boundaries of what's possible in bionic limb technology, the integration of advanced materials, control systems, and neural interfaces promises to bring us closer to truly biomimetic prosthetic solutions.

Bibliography

[1] Merkur Alimusaj et al. "*Kinematics and Kinetics with an Adaptive Ankle Foot System During Stair Ambulation of Transtibial Amputees*". In: *Gait & Posture* 30 (Aug. 2009), pp. 356–63. DOI: `10.1016/j.gaitpost.2009.06.009`.

[2] Hugh M. Herr and Alena M Grabowski. "*Bionic Ankle-Foot Prosthesis Normalizes Walking Gait for Persons with Leg Amputation*". In: vol. 279. 1728. 2012. DOI: `10.1098/rspb.2011.1194`.

[3] Samuel Kwok-Wai Au. "*Powered Ankle-Foot Prosthesis for the Improvement of Amputee Walking Economy*". PhD thesis. Massachusetts Institute of Technology, 2007.

[4] Ottobock. *"Empower Ankle"*. URL: `https://www.ottobockus.com/prosthetics/lower-limb-prosthetics/solution-overview/empower-ankle/`.

[5] Össur. *"PROPRIO FOOT®"*. URL: `https://www.ossur.com/prosthetic-solutions/products/dynamic-solutions/proprio-foot`.

[6] D. A. Winter. "*Human Balance and Posture Control during Standing and Walking*". In: *Gait & Posture* 3 (1995), pp. 193–214.

[7] N. Matsusaka. "*Control of the Medial-Lateral Balance in Walking*". In: *Acta Orthopaedica Scandinavica* 57 (1986), pp. 555–559.

[8] H Herr and MJ Carty. "The Agonist-antagonist Myoneural Interface". In: *Tech Orthop* 36.4 (Dec. 2021), pp. 337–344. DOI: `10.1097/bto.0000000000000552`.

[9] Tyler R. Clites et al. "*Proprioception from a Neurally Controlled Lower-Extremity Prosthesis*". In: *Science Translational Medicine* 10.443 (2018). DOI: `10.1126/scitranslmed.aap8373`.

[10] Max Ortiz-Catalan et al. "Self-contained neuromusculoskeletal arm prostheses". In: *New England Journal of Medicine* 382.18 (2020), pp. 1732–1738. DOI: `10.1056/NEJMoa1917537`.

[11] H. Song, T.H. Hsieh, S.H. Yeon, et al. "*Continuous neural control of a bionic limb restores biomimetic gait after amputation*". In: *Nature Medicine* (2024). DOI: `10.1038/s41591-024-02994-9`.

[12] R. D. Bellman, M. A. Holgate, and T. G. Sugar. "*SPARKy 3: Design of an Active Robotic Ankle Prosthesis with Two Actuated Degrees of Freedom using Regenerative Kinetics*". In: *2008 2nd IEEE RAS EMBS International Conference on Biomedical Robotics and Biomechatronics*. Oct. 2008, pp. 511–516. DOI: `10.1109/BIOROB.2008.4762887`.

[13] E. M. Ficanha et al. "*Design and Preliminary Evaluation of a Two DOFs Cable-Driven Ankle-Foot Prosthesis with Active Dorsiflexion-Plantarflexion and Inversion-Eversion*". In: *Frontiers in bioengineering and biotechnology* 4.36 (2016). DOI: `10.3389/fbioe.2016.00036`.

[14] Myunghee Kim et al. "*An Ankle–Foot Prosthesis Emulator With Control of Plantarflexion and Inversion–Eversion Torque* ". In: *IEEE Transactions on Robotics* 34.5 (2018). DOI: `10.1109/ICRA.2015.7139345`.

[15] Myunghee Kim and Steven H. Collins. "*Step-to-Step Ankle Inversion/Eversion Torque Modulation Can Reduce Effort Associated with Balance*". In: *Frontiers in Neurorobotics* 11 (2017). DOI: `10.3389/fnbot.2017.00062`.

[16] Woo-Seok Jang et al. "Self-Contained 2-DOF Ankle-Foot Prosthesis With Low-Inertia Extremity for Agile Walking on Uneven Terrain". In: *IEEE Robotics and Automation Letters* 6.4 (2021), pp. 8134–8141. DOI: `10.1109/LRA.2021.3098931`.

[17] Tsung-Han Hsieh et al. "Design, Characterization, and Preliminary Assessment of a Two-Degree-of-Freedom Powered Ankle–Foot Prosthesis". In: *Biomimetics* 9.2 (2024), p. 76. DOI: `10.3390/biomimetics9020076`.

[18] *Multirotor Drone Market—Report Overview.* `https://www.alliedmarketresearch.com/multirotor-drone-market-A09185`. Accessed on 18 April 2023.

[19] G Kenneally, De A, and D E Koditschek. "Design principles for a family of direct-drive legged robots". In: *IEEE Robot. Autom. Lett.* 1 (2016), pp. 900–907.

[20] T Reichert, T Nussbaumer, and J W Kolar. "Torque scaling laws for interior and exterior rotor permanent magnet machines". In: *IEEE Int. Magn. Conf.* Vol. 3. 2009, pp. 4–7.

[21] J J Lee et al. "Comparison between concentrated and distributed winding in IPMSM for traction application". In: *Proceedings of the IEEE International Conference on Electrical Machines and Systems*. Incheon, Republic of Korea, 2010, pp. 1172–1174.

[22] B Katz, J D Carlo, and S Kim. "Mini cheetah: A platform for pushing the limits of dynamic quadruped control". In: *Proceedings of the 2019 International Conference on Robotics and Automation (ICRA)*. Montreal, QC, Canada, 2019, pp. 6295–6301.

[23] S Kalouche. "GOAT: A legged robot with 3D agility and virtual compliance". In: *Proceedings of the 2017 IEEE/RSJ International Conference on Intelligent Robots and Systems (IROS)*. Vancouver, BC, Canada, 2017, pp. 4110–4117.

[24] A L Brill et al. "Tail-assisted rigid and compliant legged leaping". In: *Proceedings of the 2015 IEEE/RSJ International Conference on Intelligent Robots and Systems*. Hamburg, Germany, 2015, pp. 6304–6311.

[25] M E Carney et al. "Design and Preliminary Results of a Reaction Force Series Elastic Actuator for Bionic Knee and Ankle Prostheses". In: *IEEE Trans. Med. Robot. Bionics* 3 (2021), pp. 542–553.

[26] J Zhu et al. “Design and Backdrivability Modeling of a Portable High Torque Robotic Knee Prosthesis With Intrinsic Compliance for Agile Activities”. In: *IEEE/ASME Trans. Mechatron.* 27 (2022), pp. 1837–1845.

[27] A F Azocar et al. “Design and clinical implementation of an open-source bionic leg”. In: *Nat. Biomed. Eng.* 4 (2020), pp. 941–953.

[28] S Yu et al. “Quasi-Direct Drive Actuation for a Lightweight Hip Exoskeleton With High Backdrivability and High Bandwidth”. In: *IEEE/ASME Trans. Mechatron.* 25 (2020), pp. 1794–1802.

[29] T-H Huang et al. “Modeling and Stiffness-Based Continuous Torque Control of Lightweight Quasi-Direct-Drive Knee Exoskeletons for Versatile Walking Assistance”. In: *IEEE Trans. Robot.* 38 (2022), pp. 1442–1459.

[30] C Nesler et al. “Enhancing Voluntary Motion With Modular, Backdrivable, Powered Hip and Knee Orthoses”. In: *IEEE Robot. Autom. Lett.* 7 (2022), pp. 6155–6162.

[31] U H Lee, C-W Pan, and E J Rouse. “Empirical Characterization of a High-performance Exterior-rotor Type Brushless DC Motor and Drive”. In: *Proceedings of the 2019 IEEE/RSJ International Conference on Intelligent Robots and Systems (IROS).* Macau, China, 2019, pp. 8018–8025.

[32] G B Katz. “A Low Cost Modular Actuator for Dynamic Robots”. MA thesis. Cambridge, MA, USA: Massachusetts Institute of Technology, 2018.

[33] T H Hsieh. “Design and Control of a Two-Degree-of-Freedom Powered Ankle-Foot Prosthesis”. MA thesis. Cambridge, MA, USA: Massachusetts Institute of Technology, 2019.

[34] I Kang et al. “Design and Validation of a Torque-Controllable Series Elastic Actuator-Based Hip Exoskeleton for Dynamic Locomotion”. In: *J. Mech. Robot.* 15 (2023), p. 021007.

[35] Tsung-Han Hsieh, Seong Ho Yeon, and Hugh Herr. "Energy Efficiency and Performance Evaluation of an Exterior-Rotor Brushless DC Motor and Drive System across the Full Operating Range". In: *Actuators* 12.8 (2023), p. 318. DOI: `10.3390/act12080318`.

[36] J E Fleckenstein. *Three-Phase Electrical Power*. 1st ed. Boca Raton, FL, USA: CRC Press, 2016.

[37] *Everest XCR Product Description*. `https://drives.novantamotion.com/eve-xcr/product-description`. Accessed on 8 February 2023.

[38] *Drive Protections*. `https://drives.novantamotion.com/denxcr/drive-protections`. Accessed on 18 May 2023.

[39] CL Brockett and GJ Chapman. "Biomechanics of the ankle". In: *Orthop Trauma* 30.3 (June 2016), pp. 232–238. DOI: `10.1016/j.mporth.2016.04.015`.

[40] K.R. Embry, D.J. Villarreal, R.L. Macaluso, et al. "Modeling the Kinematics of Human Locomotion Over Continuously Varying Speeds and Inclines". In: *IEEE Trans Neural Syst Rehabil Eng* (2018).

[41] G Bovi et al. "A multiple-task gait analysis approach: kinematic, kinetic and EMG reference data for healthy young and adult subjects". In: *Gait Posture* (2011).

[42] Robert L. Mott, Edward M. Vavrek, and Jyhwen Wang. *Machine Elements in Mechanical Design*. 6th ed. Pearson, Apr. 2017.

[43] G. A. Pratt and M. M. Williamson. "Series elastic actuators". In: *Proceedings 1995 IEEE/RSJ International Conference on Intelligent Robots and Systems. Human Robot Interaction and Cooperative Robots* 1 (1995), pp. 399–406. DOI: `10.1109/IROS.1995.525827`.

[44] Jonathan W. Hurst. "The Role and Implementation of Compliance in Legged Locomotion". PhD Thesis. Pittsburgh, PA: Robotics Institute, Aug. 2008.

[45] N. Tsagarakis et al. "A compact soft actuator unit for small scale human friendly robots". In: *Proc. IEEE Int. Conf. Robot. Automat.* 2009, pp. 4356–4362.

[46] Marco Hutter et al. "High Compliant Series Elastic Actuation for the Robotic Leg ScarlETH". In: *Proceedings of the International Conference on Climbing and Walking Robots*. 2011, pp. 507–514. DOI: `10.1142/9789814374286_0059`.

[47] N. A. Paine. "High-performance series elastic actuation". Ph.D. dissertation. Dept. Elect. Comput. Eng., 2014.

[48] M. Hutter et al. "ANYmal - a highly mobile and dynamic quadrupedal robot". In: *Proc. IEEE/RSJ Int. Conf. Intell. Robots Syst.* 2016, pp. 38–44.

[49] d. G. Fernández et al. "Design, modelling and control of novel series-elastic actuators for industrial robots". In: *Actuators* 9.1 (2020), p. 6. DOI: `10.3390/act9010006`.

[50] A. Shu et al. "Impact Robustness Versus Torque Bandwidth: A Design Guide for Differential Elastic Actuators". In: *IEEE Transactions on Robotics* 40 (2024), pp. 3657–3675. DOI: `10.1109/TRO.2024.3422049`.

[51] S. K. Au and H. M. Herr. "Powered ankle-foot prosthesis". In: *IEEE Robotics & Automation Magazine* 15.3 (Sept. 2008), pp. 52–59. DOI: `10.1109/MRA.2008.927697`.

[52] S. H. Yeon et al. "Acquisition of Surface EMG Using Flexible and Low-Profile Electrodes for Lower Extremity Neuroprosthetic Control". In: *IEEE Trans. Med. Robot. Bionics* 3.3 (Aug. 2021). Epub 2021 Jul 21. PMID: 34738079; PMCID: PMC8562690, pp. 563–572. DOI: `10.1109/TMRB.2021.3098952`.

[53] Hyungeun Song. "*Design and Control of Mechanoneural Interfaces for Neuroprosthetic Limbs*". Harvard-MIT Program in Health Sciences and Technology. PhD thesis. Massachusetts Institute of Technology, 2023. URL: `https://hdl.handle.net/1721.1/153092`.

[54] J. Markowitz et al. "Speed adaptation in a powered transtibial prosthesis controlled with a neuromuscular model". In: *Philos. Trans. R. Soc. B* 366.1570 (May 2011). PMID: 21502125; PMCID: PMC3081504, pp. 1621–1631. DOI: `10.1098/rstb.2010.0347`.

[55] Michael Lars Palmer. “*Sagittal plane characterization of normal human ankle function across a range of walking gait speeds*”. Department of Mechanical Engineering. MA thesis. Massachusetts Institute of Technology, 2002. URL: `http://hdl.handle.net/1721.1/16802`.